

Durham E-Theses

Preparing for Dark Matter: Maximising our discrimination power in the event of detection

CHEEK, ANDREW

How to cite:

CHEEK, ANDREW (2019) *Preparing for Dark Matter: Maximising our discrimination power in the event of detection*, Durham theses, Durham University. Available at Durham E-Theses Online: <http://etheses.dur.ac.uk/13291/>

Use policy

The full-text may be used and/or reproduced, and given to third parties in any format or medium, without prior permission or charge, for personal research or study, educational, or not-for-profit purposes provided that:

- a full bibliographic reference is made to the original source
- a [link](#) is made to the metadata record in Durham E-Theses
- the full-text is not changed in any way

The full-text must not be sold in any format or medium without the formal permission of the copyright holders.

Please consult the [full Durham E-Theses policy](#) for further details.

Preparing for Dark Matter

*Maximising our discrimination power in the
event of detection*

Andrew Cheek

A Thesis presented for the degree of
Doctor of Philosophy



Institute for Particle Physics Phenomenology
Department of Physics
Durham University
United Kingdom

September 2019

Preparing for Dark Matter

*Maximising our discrimination power in the
event of detection*

Andrew Cheek

Submitted for the degree of Doctor of Philosophy

September 2019

Abstract: Numerous experimental observations place Dark Matter (DM) as a central character in our cosmological history. Many extensions to the Standard Model of particles physics provide candidates for DM, often predicting interactions additional to gravity. This gives us the opportunity to experimentally probe these extensions and determine the nature of DM. In this thesis, we explore how direct DM detection could be used most effectively to achieve this goal. With this in mind, we have developed a tool for performing multidimensional parameter scans. This tool allows us to evaluate the capabilities of current and future detectors for detecting and understanding DM interactions. We show that by extending the energy region analysed, detection sensitivities and parameter reconstruction can be improved substantially. These insights play an important role in more global analyses, where hints of DM could come from other experiments, but verification depends on direct detection.

Contents

Abstract	III
List of Figures	IX
List of Tables	XIX
1 The Status of Dark Matter	1
2 Direct Detection of Dark Matter	29
2.1 Effective Theory of DM-nucleus interactions	31
2.2 Matching the relativistic and non-relativistic theories	36
2.3 Current Experimental landscape	43
3 Determining Dark Matter Properties	47

3.1	Statistical tools	49
3.2	Astrophysical inputs and their uncertainties	52
3.3	Analysis Strategies	56
4	RAPIDD	61
4.1	Parametrization of the DM detection rate	62
4.2	Examples	67
4.3	Simplified dark matter models	74
4.4	Summary	89
5	Improving the Reach of Direct Detection	91
5.1	Energy Region of Interest in direct detection experiments	94
5.2	Benefits of enlarging the energy window	98
5.3	Summary	114
6	Dark Matter from Flavour Anomalies	117
6.1	Introduction	117

6.2	Our model	119
6.3	Direct DM detection prospects and constraints	130
6.4	LHC constraints and prospects for high-luminosity	135
6.5	Summary	143
7	Conclusions	147

List of Figures

1.1	Rotation curve for the NGC 6503 galaxy. Also shown is the predicted rotation curve from different components of the galaxy. Figure taken from Ref. [12].	3
1.2	Image of the bullet cluster collision. The green contours on the left and right represent the matter density as inferred by from gravitational lensing. On the left, stellar matter is shown also. On the right, the distribution hot gas from X-ray observations is depicted by the color grading. As can be seen, the majority of the mass in the clusters moves straight past each other, unaffected. Images taken from [20].	4
1.3	Angular power spectrum of the CMB temperature fluctuations taken from Ref. [34]. The curve represents the best assuming Λ CDM cosmological model. Residuals are shown in the bottom panel. . . .	8
1.4	Concordance between Deuterium to Hydrogen abundance found in Ref. [35] and the the Planck collaborations result reported in Ref. [34]. The black curve corresponds to BBN calculations of primordial abundances as a function of baryon density $\Omega_b h^2$ [37].	9

-
- 1.5 The dashed line comes from the simply counting the relativistic degrees of freedom in both Eq.(1.22) and Eq.(1.23) as contributions to the energy and entropy density respectively. Ref. [62] calculates these contributions more precisely and considers the QCD phase transition at different temperatures, which we show with solid lines. We see that the approximation holds up fairly well. 17
- 1.6 Numerical solutions to eq.(1.27) for different values of m_χ on the left and $\langle\sigma v\rangle$ on the right. A dotted line at $x = 20$ is included to show limited variation. 18
- 1.7 The different avenues for DM detection. 21
- 2.1 DM interacting with nucleons. The incoming and outgoing DM particles have momenta of \vec{p} and \vec{p}' , respectively, whereas incoming and outgoing nucleons have momenta \vec{k} and \vec{k}' , respectively. We choose the transfer momentum to be defined by $\vec{q} = \vec{p} - \vec{p}' = \vec{k}' - \vec{k}$ 30
- 2.2 Recoil spectra for a number of common operator responses. All spectra are calculated with couplings $c_i = 1$ to give an impression of the difference in size of the responses. The mass of the DM particle provoking these spectra is $m_\chi = 100$ GeV. 34

-
- 2.3 The current exclusion limits of spin-independent (\mathcal{O}_1) interactions between DM (χ) and nucleons (N) for an array of experiments. The exclusion limits presented here are to the same confidence as quoted in the relevant papers. Refs. [102, 104, 107, 115, 116] provide 90% confidence for the upper limit exclusions for PandaX, Xenon1T, CRESST, Darkside-50, NEWS-G and CDMS respectively. For DAMA, the 3σ (90% C.L.) reconstruction regions are shown [141]. 44
- 2.4 **(Left)** The best constraints on proton-DM spin dependent interaction, including direct detection and annihilation constraints coming from SuperK and IceCube. **(Right)** Constraints on the neutron-DM spin dependent interaction. 45
- 3.1 Exclusion limits published in 2018 for the XENON1T experiment [102]. We see that the naive Poissonian method is effective at replicated published experimental limits in the mass region above ~ 100 GeV. 51
- 3.2 The variation of the halo distribution function Eq.(3.15) due to the nuisance parameters k , v_0 and v_{esc} . When panel is not varying a particular panel its SHM value is taken, i.e. $k = 1$, $v_0 = 220 \text{ km s}^{-1}$ and $v_{\text{esc}} = 544 \text{ km s}^{-1}$ 54
- 3.3 The same as Figure 3.2 but now for the halo integral $\eta(v)$. The Earth and Sun's motions are incorporated for these evaluations. We have also shown the plots on a logarithmic because the differences in the tail of the distribution are important for the recoil spectra, especially for low DM masses. 55

-
- 4.1 Execution time of the surrogate model RAPIDD (red lines) as a function of the number livepoints used in MultiNest runs [228, 229]. For reference, the gray lines represent the runtime of the full physics code. The solid (dashed) lines correspond to the case without (with) astrophysical uncertainties. 64
- 4.2 Reconstruction of DM parameters in the (m_χ, c_1^0) plane for two benchmark points. The best-fit point and 1σ (68% C.L.) and 2σ (95% C.L.) regions are shown for the results obtained with RAPIDD (red cross and shaded areas) and the full physics code (black stars and solid and dashed black lines). 70
- 4.3 Reconstruction of DM parameters in (m_χ, c_1^0, c_1^1) . The best-fit point and 1σ (68% C.L.) and 2σ (95% C.L.) regions are shown for the results obtained with RAPIDD (red cross and shaded areas) and the full physics code (black star and solid and dashed black lines). . . . 72
- 4.4 Reconstruction of DM parameters in the (m_χ, c_1^0) plane when astrophysical uncertainties are included. The best-fit point and 1σ (68% C.L.) and 2σ (95% C.L.) regions are shown for the results obtained with RAPIDD (red cross and shaded areas) and the full physics code (black star and solid and dashed black lines). 74

- 4.5 Profile likelihood for the reconstruction of DM parameters for the simulated data of benchmark point BP1, using simplified model SS. Dashed blue, green, and orange lines correspond to the 2σ (95% C.L.) contours obtained for individual targets of xenon, germanium, and argon. The light and dark pink shaded regions bounded by black dashed and solid lines correspond to the 1σ (68% C.L.) and 2σ (95% C.L.) contours obtained for the combination of the three targets. The best fit point is represented by a white star. For reference, the one-dimensional profile likelihoods are also shown. 77
- 4.6 Reconstruction of parameters for BP1: Differential rate as a function of the recoil energy corresponding to the best fit point in each simplified model (columns) and for each of the experimental targets (rows). The thick black line corresponds to the full differential rate obtained from the best fit point (after combination of data from the three targets) in each of the simplified models. For reference, the thick red line shows the differential rate corresponding to the benchmark point. The thin dotted (dot-dashed) lines represent the individual contributions from momentum dependent (independent) operators. The vertical dashed lines delimit the energy range explored for each target. The table indicates the parameters for the best fit points in each case (using the same colour code as the lines in the plots), and the value for its log-likelihood calculated using eq. 3.2. Gray shading is used to denote the true model (SS in this case). 80

-
- 4.7 Profile likelihood for the reconstruction of DM parameters for the simulated data of benchmark point BP2, using simplified model SS. Much like Figure 4.5, dashed blue, green, and orange lines correspond to the 2σ (95% C.L.) contours obtained for individual targets of xenon, germanium, and argon. The light and dark pink shaded regions bounded by black dashed and solid lines correspond to the 1σ (68% C.L.) and 2σ (95% C.L.) contours obtained for the combination of the three targets. The best fit point is represented by an white star. For reference, the one-dimensional profile likelihoods are also shown. 82
- 4.8 The same as in Figure 4.7, but for simplified model SV. 83
- 4.9 The same as in Figure 4.7, but for simplified model FV. 84
- 4.10 The same as in Figure 4.6, but for benchmark point BP2. 85
- 4.11 Profile likelihood for the reconstruction of DM parameters for the simulated data of benchmark point BP3, using simplified model SS. Much like Figure 4.5, dashed blue, green, and orange lines correspond to the 2σ (95% C.L.) contours obtained for individual targets of xenon, germanium, and argon. The light and dark pink shaded regions bounded by black dashed and solid lines correspond to the 1σ (68% C.L.) and 2σ (95% C.L.) contours obtained for the combination of the three targets. The best fit point is represented by an white star. For reference, the one-dimensional profile likelihoods are also shown. 86
- 4.12 The same as in Figure 4.11, but for simplified model SV. 87

-
- 4.13 The same as in Figure 4.6, but for benchmark point BP3. No events are expected for argon in the last row of plots. 88
- 5.1 The expected recoil spectrum for EFT operators, \mathcal{O}_1 (top left panel), \mathcal{O}_6 (top right panel), \mathcal{O}_{10} (bottom left panel), and for anapole interactions (bottom right panel) in a xenon experiment. The DM mass is chosen to be $m_\chi = 100$ GeV (solid), 500 GeV (dashed), and 1000 GeV (dotted). The vertical dashed lines represent $E_R^{\max} = 30$ keV and 500 keV. The coupling for each operator has been fixed to produce 100 events in the energy range $[3, 30]$ keV. 100
- 5.2 Projected exclusion limits for a xenon detector for EFT operators, \mathcal{O}_1 , \mathcal{O}_6 , \mathcal{O}_{10} , and for anapole interactions. The solid, dashed, and dotted lines correspond to $E_R^{\max} = 30, 250$ and 500 keV, respectively. 101
- 5.3 The sensitivity of Xenon experiments as a function of the E_R^{\max} in the experiment. We show the results for two heavy DM particles $m_\chi = 1$ TeV (solid) and $m_\chi = 10$ TeV (dashed). 102
- 5.4 Projected exclusion limits for an argon detector for EFT operators, \mathcal{O}_1 and \mathcal{O}_{11} . The solid, dashed, and dotted lines correspond to $E_R^{\max} = 50, 100$ and 300 keV, respectively. 102
- 5.5 Mass reconstruction parameter, Δ_m (defined in eq. 5.3), as a function of the DM mass for operators \mathcal{O}_1 , \mathcal{O}_6 , and \mathcal{O}_{10} from the left to right panels in a xenon detector. We have assumed a benchmark point, for each value of the DM mass, that produces 100 nuclear recoil events. The light to dark grey regions correspond to different energy ROIs, with $E_R^{\max} = 30, 250, 500$ keV, respectively. 105

- 5.6 Results from a 3D parameter scan, fitting mock data from our benchmark point with mass $m_\chi = 1$ TeV and a coupling to \mathcal{O}_1 and \mathcal{O}_{10} which produces 100 counts in the [3, 30] keV window. The 2σ contours are shown from light gray to dark gray for $E_R^{\max} = 30, 250$ and 500 keV, respectively. The white star represents the benchmark point. 106
- 5.7 Same as figure 5.6 but for $m_\chi = 500$ GeV and a coupling via the anapole moment. The black dashed line in the (c_9, c_8) plane represents the relation among these couplings in an anapole DM model. . . . 107
- 5.8 Profile likelihoods for the reconstruction of DM parameters for a 100 GeV DM benchmark point that produces 100 counts in our future Xe and Ar detector configurations given in table 5.1, for a coupling only to \mathcal{O}_1 . Red and blue shaded regions correspond to 2σ (light shade) and 1σ (dark shade) regions obtained from the individual targets of Xe and Ar, respectively. The top row corresponds to the *nominal* configuration of the experiments assuming an energy window of [3, 30] keV for Xe and [5, 50] keV for Ar. The bottom row corresponds to the *extended* configuration assuming an energy window of [3, 500] keV for Xe and [5, 300] keV for Ar. The left and right panels correspond to the SHM and EAGLE halo models, respectively, which were assumed to generate the data (i.e. the *true* halo model). Every parameter scan has been performed assuming the SHM with values given in table 5.2. 111
- 5.9 Same as figure 5.8, but with an experimental exposure increased by a factor of 10, i.e. a benchmark point that produces 1000 counts. . . . 112
- 5.10 Same as figure 5.8 but with a coupling only to operator \mathcal{O}_{11} 113

-
- 6.1 One-loop diagram contribution from the new particles to the $b \rightarrow s\mu^+\mu^-$ transitions. 120
- 6.2 Tree-level contributions to the DM pair annihilation. 123
- 6.3 The indirect detection constraints for the annihilation to muons from Fermi [325] and AMS [323,324]. The thermal cross sections today is shown for the Dirac DM candidate in this model. 124
- 6.4 The dark (light) green area is the 1σ (2σ) allowed region by $b \rightarrow s\mu^+\mu^-$ observables in the $(\text{Re}(\lambda_s\lambda_b^*), \text{Im}(\lambda_s\lambda_b^*))$ plane. Dark (light) blue regions correspond to 1σ (2σ) B_s - mixing allowed regions. We take $\lambda_\mu = \sqrt{4\pi}$ and $m_{\phi_q} = 1.5$ TeV (top row), 2.5 TeV (bottom row). The specific values of m_χ , m_{ϕ_q} are given in the plot and m_{ϕ_l} is fixed to reproduce the measured DM relic abundance. 127
- 6.5 Loop process that leads to DM anapole interaction in this model. 132
- 6.6 Theoretical predictions for the anapole (**left**) and spin-independent (**right**) couplings, \mathcal{A} and c_1 , as a function of the DM mass, m_χ for the four benchmark points: A1 (red points), A2 (green), B1 (orange), and B2 (blue). For comparison, we show the current exclusion line by Xenon1T [102] and the predicted reach of LZ [231,338] and DarkSide-20k [113]. The shaded area represents the neutrino floor. 134
- 6.7 Diagrams for the pair production of the coloured scalar mediator, ϕ_q , leading to dijet + \cancel{E}_T signatures in the final state. Diagrams (a1)–(a4) are generated by purely QCD interactions, and diagrams (b), (c1)–(c4) are generated by DM t-channel exchange. 137

- 6.8 Diagrams for the pair production of the leptonic scalar mediator, ϕ_l , leading to $\mu\mu/\mu\nu + \cancel{E}_T$ signatures in the final state. 138
- 6.9 LHC limits from the $pp \rightarrow jj + \cancel{E}_T$ (green) and $pp \rightarrow \mu\mu + \cancel{E}_T$ (blue) searches. On the left (right), results for the scenario with $|\lambda_\mu| = 2$ ($|\lambda_\mu| = \sqrt{4\pi}$) are presented. The figures in the upper panel correspond to $\lambda_b = \lambda_s^*$, while the bottom panel shows limits for $\lambda_b = 4\lambda_s^*$. The colour code represents the average value of the coupling $|\lambda_b|$ in the region allowed by flavour constraints, as defined in the text. Solid lines represent the current exclusion limits, whereas dashed ones correspond to the projected reach of the LHC High luminosity phase. 140
- 6.10 Kinematic distributions for dijet (green) and dilepton (blue) signals produced by a benchmark point, which just escapes the constraints for current 13 TeV bounds but will be constrained by the leptonic channel of the HL-LHC. We plot the distribution for both energies of 13 TeV and 14 TeV with a fixed luminosity of 10 fb^{-1} 143
- 6.11 The same as in Figure 6.6, but including constraints coming from collider results as shown in Figure 6.9. 144

List of Tables

1.1	Quantum numbers for the SM fields. Remember that $\mathbf{1}$ in an $SU(N)$ group is uncharged under that group and transforms trivially, whereas \mathbf{N} and $\mathbf{N}^2-\mathbf{1}$ transform in the fundamental and adjoint representations respectively. For $U(1)$, an uncharged field has the quantum number 0. The subscripts refer to the chirality of the fields	10
2.1	List of non-relativistic EFT operators for spin-1/2 and spin-1 DM particles, classified according to their dependence on the momentum exchange.	33
4.1	Specifications of the direct detection experiments considered in this chapter. Bin no. refers to the number of equally spaced bins we use for each target.	67
4.2	Benchmark points considered in this chapter. They all satisfy experimental constraints from direct detection experiments, and are within the reach of next generation detectors. For reference, we indicate the total number of DM events expected in each of the experimental configurations of Table 4.1.	75

5.1	Specifications of the xenon and argon experiments considered in this work inspired by future LZ [232] and DarkSide [112] experiments, respectively.	97
5.2	The peak speed of the Maxwellian velocity distribution, local circular speed, Galactic escape speed, and the local DM density assumed in the SHM (row 1) and extracted from the simulated MW-like galaxy in the EAGLE simulation farthest from the SHM (row 2).	109
6.1	Quantum numbers of the new fields. We also indicate the charges under \mathcal{Z}_2	120
6.2	List of experimental searches sensitive to our model, where l denotes electron and muon. The third column describes the final state targeted by the analysis and the last column displays the total integrated luminosity.	141

Declaration

The work in this thesis is based on research carried out in the Department of Physics at Durham University. No part of this thesis has been submitted elsewhere for any degree or qualification and it is all my own work unless referenced to the contrary in the text. The following chapters in this work are based on articles that have been published,

- Chapter 4 is based on Ref. [1]. “*Surrogate Models for Direct Dark Matter Detection*”, D.G. Cerdeño, A. Cheek, E. Reid, H. Schulz, *JCAP* 1808 no. 011 (2018).
- Chapter 5 is based on Ref. [2]. “*Opening the energy window on direct dark matter detection*”, N. Bozorgnia, D. G. Cerdeño, A. Cheek, B. Penning, *JCAP* 1812, no. 12, 013 (2018).
- Chapter 6 is based on Ref. [3]. “*B anomalies and dark matter: a complex connection*”, D. G. Cerdeño, A. Cheek, P. Martín-Ramiro and J. M. Moreno, *Eur. Phys. J. C* **79** (2019) 517.

Copyright © 2019 Andrew Cheek.

The copyright of this thesis rests with the author. No quotation from it should be

published without the author's prior written consent and information derived from it should be acknowledged.

Acknowledgements

I would like to thank David Cerdeño for providing me with excellent guidance and encouragement throughout my PhD, as well as creating a working atmosphere that is both fun and productive. This atmosphere was fostered by my collaborators who I would also like to thank, such as Elias Gerstmayr, Miguel Peiró, Ji-Haeng Huh, Holger Schulz, Elliott Reid, Nassim Bozorgnia, Bjoern Penning, Jesus Moreno and Pablo Martín-Ramiro. I am also thankful to those who took the time to discuss physics with me, enriching my understanding, such as Bradley Kavanagh, Jessica Turner and Ricardo Catena.

I am grateful to the Science and Technology Facilities Council (STFC) for financially supporting my work as well as Silvia Pascoli and the Elusives network for the opportunity to do research secondments at FERMILAB and IPMU, two inspirational experiences. My gratitude goes to the IFT and the MultiDark project, for hosting me in Spain. Additionally, I would like to thank my examiners for taking the time to read and provide feedback on this thesis.

Thank you to all my peers who have made the PhD an enjoyable experience, keeping the OC118 spirit alive. To Andres, Alexis, Matheus and Kristian, thank you for the many illuminating conversations. Thank you to Duncan, Darren, James, Joey, Matthew, Maura and Tom for always being helpful. Furthermore, I am hugely

grateful to the support staff at the IPPP, past and present, they really cannot be praised enough. I am also grateful to the Academic staff who make the IPPP a uniquely fascinating place to work.

Outside physics, Stefan, Mary, Alice, Luke, Jonty and all members of the Cognoscenti have helped me tremendously these past years. Thank you for the laughs. To all members of the Monroes, thank you for music and friendship. To Esther, thank you for everything.

Last but not least, I would like to thank my family. Who have supported me unconditionally and are a source of inspiration. This includes my biological family and the Garcia Monreals. Thank you all.

What happened before the beginning? What was God doing before he made the world? Was he preparing Hell for people who asked such questions?

— from *Brief Answers to the Big Questions* by S. Hawking

Dedicated to

Esther García Monreal

Chapter 1

The Status of Dark Matter

Dark Matter (DM) plays an essential role in our understanding of the Universe and its evolution. This omnipresent yet utterly mysterious form of matter cries out for deeper understanding. Here we review what is known about DM, the constraints placed on its properties from cosmology and astrophysics, and the role it plays in theories beyond the Standard Model.

In the 20th century, astronomers started to determine the total mass of galaxies and galaxy clusters by using dynamics and their understanding of gravity. They could compare this total mass with the amount of luminous matter belonging to said system, with what is known as the mass-to-light ratio. Fairly early on, estimates suggested that a large amount of matter in galaxies and galaxy clusters is invisible [4, 5], but only after developments in radio astronomy and spectrography did a clearer picture form. Precise measurements of the rotational speeds of stars and neutral hydrogen gave clear indications that the matter profile of galaxies tended not to follow that of the luminous matter [6, 7].

Objects in the outer regions of spiral galaxies orbit around a galactic center, with some circular velocity, v_c . According to Newtonian gravity, this is given by,

$$v_c^2(r) = \frac{M(r)G}{r}, \quad (1.1)$$

where G is gravitational constant and $M(r)$ is the mass contained at distance r from the galactic center. We have assumed here that the mass distribution is spherically symmetric, i.e., $M(r) = \int_0^r 4\pi r'^2 \rho(r') dr'$, where ρ is the matter density. Astronomers measured the v_c of objects at different distances to build what is known as a rotation curve, allowing them to infer the mass distributions of a given galaxy. A number of different galaxies showed that for large distances, far beyond the region where the majority of stars reside, the rotation curve is approximately flat, $v_c(r) = \text{const.}$, as shown in Figure 1.1. This implies that

$$\rho(r) = \frac{\text{const.}^2}{4\pi G r^2}. \quad (1.2)$$

These mass distributions have no luminous counterpart, either in gaseous or stellar matter. Further evidence for this kind of large symmetrical structure in galaxies came from the development of N-body simulations. They showed that rotating spiral galaxies are in fact unstable without the addition of a DM halo [8–10]. This also gave some motivation for the assumption of spherical symmetry use to derive Eq. 1.2, which, to a first approximation is still the accepted picture. It was becoming clear that a large amount non-luminous matter was present in these galaxies, exactly how much was uncertain, but many mass-to-light ratios were reported between 3-10 [11].

An alternative solution to this missing mass problem was proposed with Modified Newtonian Dynamics (MOND) [13, 14], which affects small acceleration scales. Initially introduced as a phenomenological model, substantial work has been conducted to try to embed MOND into a more fundamental theoretical framework. In particular, the initial formulation of MOND was not relativistic and therefore inconsistent with General Relativity (GR). One of the great successes of GR is that it successfully

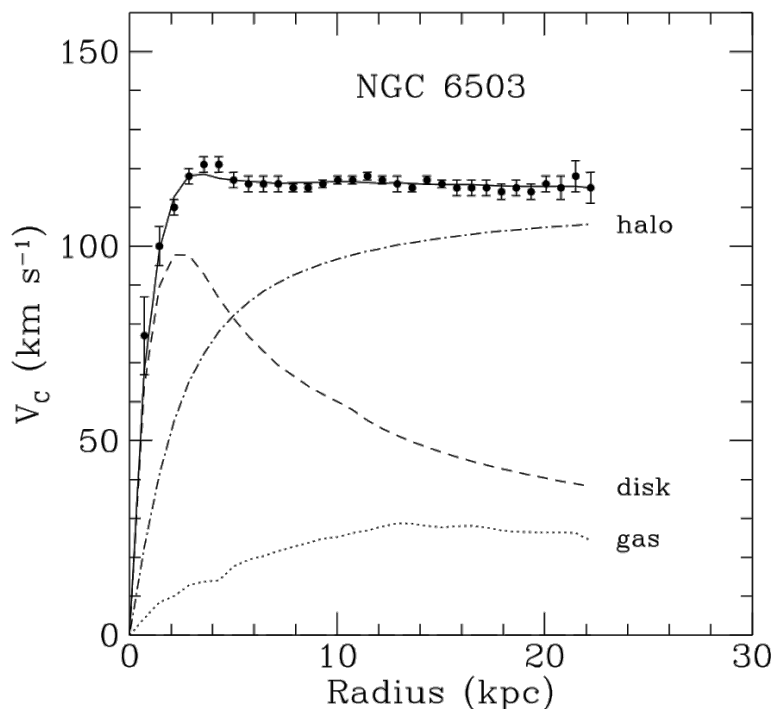


Figure 1.1: Rotation curve for the NGC 6503 galaxy. Also shown is the predicted rotation curve from different components of the galaxy. Figure taken from Ref. [12].

predicts the phenomenon of gravitational lensing, where the light from background stars is bent by a massive foreground object. In many cases this can be used to simply determine the total mass of a foreground galaxy or cluster, which can in turn be compared with the luminous matter measured in the object [15]. TeVeS [16], standing for Tensor-Vector-Scalar gravity, was developed as a modified gravity that is consistent with lensing results and rotation curves, it still however, has difficulties reproducing gas density distributions found in galaxy clusters [17].

Greater problems occur, when one considers cluster mergers. The most famous being the Bullet Cluster, a collision between two galaxy clusters, leaving a shock front formation in the gas component. Lensing can produce information about where the predominant matter lies whereas X-ray astronomy gives information about the gaseous matter that interacts and collides as expected. From Figure 1.2 we can see the difference the two measurements. Lensing shows that the two clusters simply

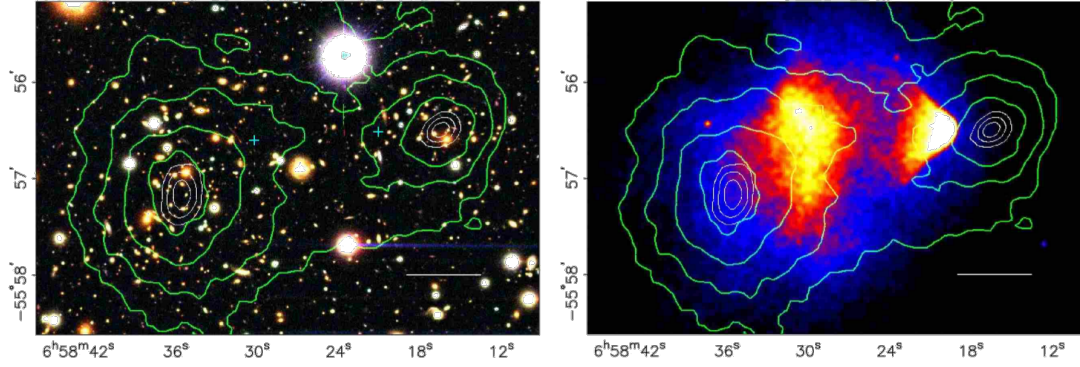


Figure 1.2: Image of the bullet cluster collision. The green contours on the left and right represent the matter density as inferred by from gravitational lensing. On the left, stellar matter is shown also. On the right, the distribution hot gas from X-ray observations is depicted by the color grading. As can be seen, the majority of the mass in the clusters moves straight past each other, unaffected. Images taken from [20].

passed through each other, whereas X-ray images tell the story of a violent collision. Over the years more of these mergers have been studied [18] providing processes that are very difficult to reconcile with TeVeS. In the particle interpretation however, this simply constrains the strength of self-interaction within the dark sector to [19]

$$\frac{\sigma_{\text{self}}}{m_{\text{DM}}} < 1 \text{ cm}^2 \text{ g}^{-1}, \quad (1.3)$$

where σ_{self} is the interaction cross section for DM, self scattering, and m_{DM} is DM mass.

Both the Bullet Cluster and galaxy rotation curves could be explained by some population of dim astrophysical objects, such as brown dwarfs. In fact, these objects are commonly dubbed massive astronomical compact halo objects (MACHOs) and were the subject of two experimental searches looking for micro-lensing events [21,22]. The EROS collaboration constrained MACHOs in the mass range $10^{-7} - 1 M_{\odot}$ to be less than 8% of DM halo mass [21]. This result seemed to make the MACHO explanation for DM less probable. More convincing evidence comes when considering the role DM had in Big Bang Cosmology.

With the discovery of Hubble's law [23] and the Cosmic Microwave Background (CMB) [24], physicists sought to understand how the universe evolved from a hot dense plasma to what we see today. Galaxies no longer had to just be stable, they had to be created.

The very early stages of the Universe are driven by a period of Cosmic Inflation, which has the effect of pushing the curvature of the space-time metric to zero [25]. Following inflation is a period of reheating, where the energy from the rapid expansion gets converted into hot SM particles. The homogeneous and isotropic metric, with zero curvature is described by the FRW metric,

$$ds^2 = dt^2 - a^2(t) \left(dr^2 + r^2 d\theta^2 + r^2 \sin^2(\theta) d\phi^2 \right), \quad (1.4)$$

in spherical coordinates and $a(t)$ is the scale factor where $a(t_0) = 1$ for the current epoch, t_0 . The Hubble parameter ($H(t) = \dot{a}/a$) is often expressed in terms of the dimensionless parameter,

$$h(t) = \frac{H(t)}{100 \text{ km s}^{-1} \text{ Mpc}^{-1}}. \quad (1.5)$$

Substituting this metric into Einstein's field equation leads to the Friedmann equation,

$$H^2 = \frac{8\pi G \rho_c}{3}, \quad (1.6)$$

where once again, flatness is assumed such that the energy density ρ_c in this equation is actually known as the critical density, i.e. the density required to have a flat universe, the value of which is $\rho_c = 1.054 \times 10^{-5} h^2 \text{ GeV cm}^{-2}$.

The equation of state $p = w\rho$ can be applied to different forms of energy density, such as matter ($w = 0$) or radiation ($w = 1/3$), and in an expanding Universe evolves as,

$$\frac{\dot{\rho}}{\rho} = -3(1+w)H, \quad (1.7)$$

which produces the result $\rho_m \propto a^{-3}$ for matter and $\rho_r \propto a^{-4}$ for radiation. Therefore, by measuring the densities of today, one can solve

$$H(a) = H_0 \left[\frac{\Omega_{m0}}{a^3} + \frac{\Omega_{r0}}{a^4} + \Omega_{\Lambda 0} \right]^{1/2} \quad (1.8)$$

to calculate how the scale factor has changed over time. The Ω 's are density parameters normalised by ρ_c , i.e. $\Omega_i = \rho_i/\rho_c$ and $\Omega_{\Lambda 0}$ is dark energy which is not the topic of this Thesis.

From the temperature of the photons in the Cosmic Microwave Background (CMB), we can infer that the early universe was not only very dense, but also very hot. These high temperatures would produce quarks and baryons. A few minutes after the Big Bang, the universe cooled enough to support simple nuclei forming in a process known as Big Bang Nucleosynthesis (BBN) [26]. These light elements were formed from the primordial plasma, first forming protons and neutrons, then deuterium, helium-3, helium-4 and lithium. The cleanest prediction to test BBN is the abundance of deuterium, which is not known to be produced by any astrophysical source. The observed abundance of deuterium $D/H \sim 10^{-5}$ can be explained by a baryon density of $\Omega_b h^2 \sim 0.02$ [27,28]. The baryon and photon densities here would provide us with a minuscule amount of energy density, resulting in an open Universe¹. Measurements of the CMB anisotropies provide a way to test this.

The CMB is the afterglow from recombination [29,30], an event that took place approximately 380,000 years after the Big Bang. Similarly to BBN, recombination occurs when the Universe cooled enough to support composite particles, but this time the particles are neutral atoms. When this happens, photons can travel unimpeded, so the Universe becomes transparent. Before then, Thomson scattering between photons and ions kept baryonic matter and radiation closely connected forming a plasma fluid. The photons emitted from this time are still visible today and, due to

¹A universe with negative curvature

the earlier period of inflation, the temperature distribution on the sky is remarkably homogeneous. Importantly, there are small temperature fluctuations that give a tremendous amount of information about the structure of the early Universe.

At the Big Bang, density perturbations exist at all scales and are pushed out of causal contact by inflation i.e. at super horizon scales. Whilst above the horizon scale, perturbations are frozen, and will not grow or shrink. In the radiation era, perturbations begin to enter the horizon. They start to compress under gravity and expand with radiation pressure, producing Baryon Acoustic Oscillations (BAO). However, a pure dark matter perturbation will not produce BAOs and instead will slowly grow.

Since the pattern of the CMB is observed on a 2D surface, it is usually analysed using the angular power spectrum, where the multipole order, ℓ , can be related to angular size. The oscillation modes that provide the greatest temperature variations are caused by perturbations that, at the time of recombination have just reached an extrema. Therefore, the first peak in the power spectrum is determined by the time it takes for one compression to occur. Since the speed of BAOs and the time of recombination is known, the multipole order of this peak is predictable. When translating this ℓ to angular size as observed on the CMB today, only the total energy density affect the result. The first peak was measured by WMAP, where they reported a flat curvature [31, 32]. In order to extract information about the components of Ω , subsequent peaks need to be measured. For DM specifically, Ω_{DM} , the first three peaks of the CMB are sufficient. This is because the relative heights of the peaks allow one to disentangle multiple effects. The relative baryon density produces an enhancement of odd peaks due to baryon loading in oscillations, whereas the total matter density can be inferred by observing which perturbations entered the horizon before matter radiation equality. This can be observed via the effect of Gravitational Driving [33].

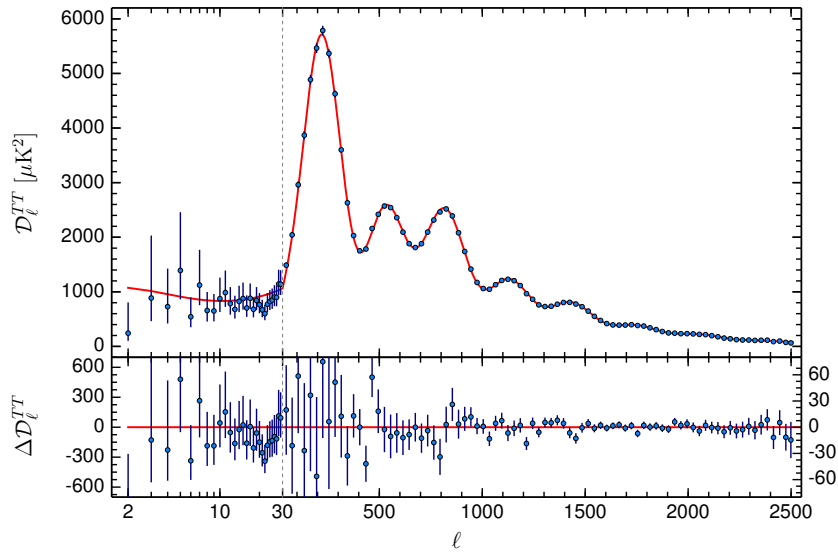


Figure 1.3: Angular power spectrum of the CMB temperature fluctuations taken from Ref. [34]. The curve represents the best assuming ΛCDM cosmological model. Residuals are shown in the bottom panel.

The various physical effects produce the intricate power spectrum, that through the precise experimental measurements of Planck, place the most stringent bounds on the total density of DM, $\Omega_{\text{DM}} h^2 = 0.1199 \pm 0.0027$ [34]. Figure 1.3 shows the power spectrum in Ref. [34] where \mathcal{D}_ℓ is the variance in temperature.

Figure 1.4 shows the consistency between the measurements of the baryon density Ω_b coming from the CMB [34] and the deuterium abundance [35]. This implies that baryons are a sub dominant component of matter in the universe, even at very early times. Suggesting that DM is some new fundamental particle that is missing from the Standard Model (SM) of particle physics².

The SM is the quantum field theory description of the most fundamental constituents of our universe. Employing local gauge symmetries, it describes particle interactions and provides some of the most precise agreement between experiment and theory

²It should be noted that *Primordial Black Holes* (PBHs) created via inflation could account for DM, but in most mass regions, this possibility is ruled out, with the possible exception of $M_{\text{PBH}} \sim 10^{-12} M_\odot$. See ref. [36] for a recent review.

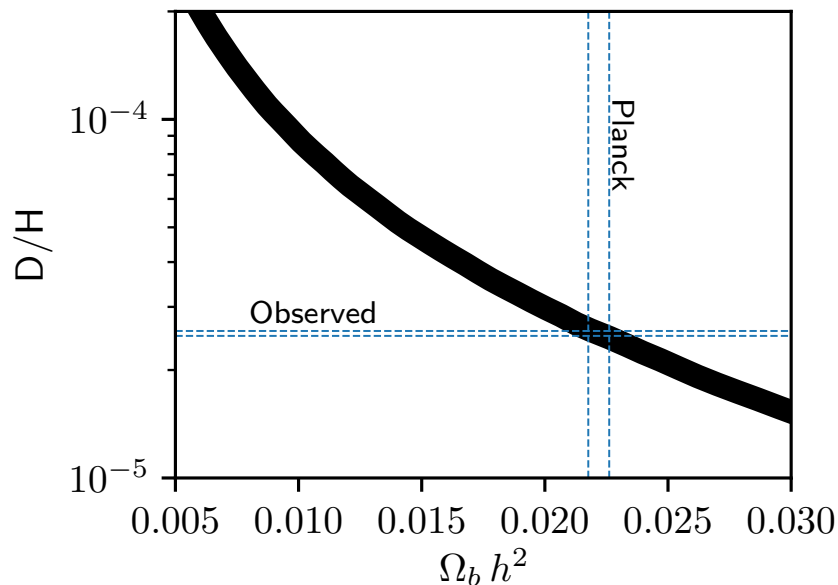


Figure 1.4: Concordance between Deuterium to Hydrogen abundance found in Ref. [35] and the the Planck collaborations result reported in Ref. [34]. The black curve corresponds to BBN calculations of primordial abundances as a function of baryon density $\Omega_b h^2$ [37].

across any discipline. The SM gauge group is $SU(3)_c \otimes SU(2)_L \otimes U(1)_Y$, where the first group corresponds to the strong force, the second describes the weak interaction and the third hypercharge. Through the Higgs mechanism, the electroweak gauge symmetry is broken, $SU(2)_L \otimes U(1)_Y \rightarrow U(1)_{EM}$, giving the bosons W^\pm and Z^0 masses. The $U(1)_{EM}$ symmetry describes electromagnetism, mediated by the massless photon.

The gauge fields are vector fields that transform in the adjoint representation, whereas the particle content, if charged under such group, transforms under the fundamental representation. The charge assignments of the SM are shown in Table 1.1, notice the different assignments for left-handed and right-handed chiral fields.

When electroweak symmetry breaking occurs, The Higgs field H , acquires a non-zero vacuum expectation value m_v providing masses to fermions via the Yukawa

	$SU(3)$	$SU(2)_L$	$U(1)_Y$
$Q_L = \begin{pmatrix} u_L \\ d_L \end{pmatrix}$	3	2	1/6
$L_l = \begin{pmatrix} \nu_L \\ l_L \end{pmatrix}$	1	2	-1/2
u_R	3	1	2/3
d_R	3	1	-1/3
l_R	1	1	-1
G_μ^a	8	1	0
W_μ^i	1	3	0
B_μ	1	1	0
H	1	2	1/2

Table 1.1: Quantum numbers for the SM fields. Remember that **1** in an $SU(N)$ group is uncharged under that group and transforms trivially, whereas **N** and $\mathbf{N}^2 - \mathbf{1}$ transform in the fundamental and adjoint representations respectively. For $U(1)$, an uncharged field has the quantum number 0. The subscripts refer to the chirality of the fields

interactions [38]

$$\mathcal{L} \supset Y_{ij}^u \bar{Q}_L^i \tilde{H} u_R^j + Y_{ij}^d \bar{Q}_L^i H d_R^j + \text{h.c.} \longrightarrow \frac{m_v}{\sqrt{2}} Y_{ij}^u \bar{u}_L^i u_R^j + \frac{m_v}{\sqrt{2}} Y_{ij}^d \bar{d}_L^i d_R^j + \text{h.c.} \quad (1.9)$$

where $\tilde{H} = i\sigma^2 H^*$ and the unitary gauge has been chosen for the Higgs field. Indices i and j run over the three generations of quarks. The Yukawa matrices Y_{ij} need not be diagonal in general. In order to diagonalise the mass terms, one transforms the SM Lagrangian via four unitary matrices, $u_{L,R} \rightarrow U_{L,R}^u u_{L,R}$ and $d_{L,R} \rightarrow U_{L,R}^d d_{L,R}$.

This is not without consequence because the charged W boson couples to both up and down quarks, leading to

$$\bar{u}_L \gamma^\mu d_L W_\mu^+ \longrightarrow \bar{u}_L \gamma^\mu (U_L^u)^\dagger \gamma^\mu U_L^d d_L W_\mu^+ = \bar{u}_L \gamma^\mu V_{\text{CKM}} d_L W_\mu^+ \quad (1.10)$$

where $V_{\text{CKM}} = (U_L^u)^\dagger U_L^d$ is the Cabibbo-Kobayashi-Maskawa (CKM) matrix [39, 40]

and can be represented as a 3×3 matrix

$$V \equiv U_u^\dagger U_d = \begin{pmatrix} V_{11} & V_{12} & V_{13} \\ V_{21} & V_{22} & V_{23} \\ V_{31} & V_{32} & V_{33} \end{pmatrix} = \begin{pmatrix} V_{ud} & V_{us} & V_{ub} \\ V_{cd} & V_{cs} & V_{cb} \\ V_{td} & V_{ts} & V_{tb} \end{pmatrix}. \quad (1.11)$$

The CKM matrix is very well measured, providing one of the minimal bars for entry that BSM models have to meet. Often BSM models adopt what is called Minimal Flavour Violation (MFV) [41, 42] which states that all new flavour changing effects follow the pattern shown in the standard model.

For leptons, mass is generated in a similar way, however neutrinos are only observed to be part of the left-handed $SU(2)_L$ doublet, so there is no renormalisable neutrino mass term in the SM,

$$\mathcal{L} \supset Y_{ij}^l \bar{L}_L^i H l_R^j + \text{h.c.} \longrightarrow \frac{v}{\sqrt{2}} Y_{ij}^l \bar{L}_L^i l_R^j + \text{h.c.} \quad (1.12)$$

For the charged leptons its observed that in the flavour basis, $Y_{ij}^l = \text{diag}(m_e, m_\mu, m_\tau)$.

Measured quark mixing and the lack of mixing in the charged lepton sector are rather constraining for BSM physics. However, there are known inconsistencies with the SM and nature. For example, neutrino flavour oscillations observed in many experiments (see refs. [43–46]) requires at least two neutrinos to have mass [47, 48]. Therefore, in the neutrino mass basis,

$$\bar{l}_L \gamma^\mu \nu_L W_\mu^+ \longrightarrow U_{\text{PMNS}}^{ij} \bar{l}_{Li} \gamma^\mu \nu_{Lj} W_\mu^+, \quad (1.13)$$

where U_{PMNS} is the Pontecorvo-Maki-Nakagawa-Sakata (PMNS) matrix and one relates the mass basis to the interaction basis via, $\nu_{Le} = \sum_i U^{1i} \nu_{Li}$. Oscillation experiments are sensitive to the parameters in the PMNS as well as the square difference of the neutrino masses $\Delta m_{ij}^2 = m_j^2 - m_i^2$.

Any theory that supersedes the SM will have to describe neutrino masses. If neutrinos are Dirac fermions, then a right handed neutrino is invoked, ν_R , for each generation with mass. Current mass bounds suggest a very small Yukawa coupling $y_\nu \approx 10^{-13}$, indicating to many that new physics is required. Interestingly, the ν_R particles are not charged via any of the gauge fields in the standard model, making it an excellent DM candidate. Below we will see that main complication comes when producing these sterile particles that in the correct amount to be DM. However, prior to this consideration the Tremaine-Gunn bound can be derived just from looking at the scale of DM structures in the Universe, this resulting in the constraint the DM mass must be above 0.4 keV [49].

If the neutrino is a Majorana fermion the only mass term is the dimension 5 Weinberg operator. Terms above dimension 4 are indicative of higher energy physics which becomes non-local at low energies. Reminiscent of the 4-Fermi theory of weak interactions [50], this approach at least provides a good explanation as to why neutrino masses are so small, since they are suppressed by the scale of the new physics. UV completions such as the seesaw mechanism often predict new particles that are DM candidates.

Inexplicably small parameters, like the neutrino and electron masses may have no further explanation. Fermion masses are technically natural, meaning their quantum corrections are proportional to the bare values. For a scalar particle like the Higgs, this is not true. In fact, the Higgs should be sensitive to any high scale physics that it couples to. Higher energy physics is expected at the Planck scale for gravitational effects and at $\sim 10^{40}$ GeV, where hypercharge develops a Landau pole, despite all this, the measured Higgs mass is 125.2 GeV [51, 52]. Many BSM models set out to remedy this and along the way predict the existence of new particles. Perhaps the most famous class of DM particle comes from supersymmetry (SUSY) [53], which predicts every SM particle has a superpartner. In order to stabilize protons, a global

symmetry named R-parity is usually invoked, which, in turn, stabilizes the lightest supersymmetric particle (LSP) [54]. A generic feature of SUSY models is that they exist at higher energies so the mass of the LSP is, in many cases, expected to be around the weak scale.

In contrast, Axion Like Particles (ALPs) are predicted to be much lighter ($m_\chi < \text{eV}$). Axions were originally introduced to solve the strong \mathcal{CP} problem, originating from the term

$$\frac{\theta}{32\pi^2} \text{Tr} [G_{\mu\nu} \tilde{G}^{\mu\nu}], \quad (1.14)$$

where θ is a dimensionless parameter, $G_{\mu\nu}$ and $\tilde{G}_{\mu\nu}$ are the QCD field strength tensor and its dual. This term is allowed via all the symmetries of the SM and contributes to the electric dipole moment of the neutron in conjunction with the quark mass matrix, M_q ,

$$\bar{\theta} = \theta + \arg(\det M_q). \quad (1.15)$$

Experimentally, the electric dipole of the neutron is yet to be measured, but results are sensitive enough to constrain $\bar{\theta} \leq 10^{-10}$, suggesting a fine tuning between θ and $\arg(\det M_q)$. The axion solution introduces a global $U(1)_{\text{PQ}}$ symmetry which is spontaneously broken, resulting in a pseudo-Goldstone boson, known as the axion [55, 56]. Nowadays ALPs find motivation from a large array of BSM models, many of which make explicit connection to DM, see Ref. [57] for a review.

The aforementioned problems with the SM could be considered small fry when one considers the observed Baryon Asymmetry of the Universe (BAU). This asymmetry is not only observed now, its been observe in both the CMB and BBN measurements. The conditions to dynamically produce BAU in the early universe are known as the Sakharov conditions [58]. They state that there must be processes that exhibit, baryon number violation, \mathcal{CP} violation and a departure from thermodynamic equilibrium. Within the SM, these processes are not present to the level required and

has motivated many extensions.

An interesting possibility is that the processes that drive the BAU also drive an asymmetry in DM, giving the abundance seen today, this is known as Asymmetric Dark Matter (ADM). Such models tend to be in the \sim GeV range [59].

Despite these issues, the SM is still tremendously predictive and manages to agree with a wide range of experiments. In order to get some hint as to how to move past the SM, there is a huge experimental and theoretical effort in testing, with ever increasing degrees of precision, SM processes. One such effort is in observations of Meson decays, where there are hints of a discrepancy. In Chapter 6 we use these hints to motivate a specific DM model.

Current efforts to improve the SM show that, in many cases, particle physicists would be looking for new particles with DM characteristics with or without the evidence from Astrophysics. The idea that DM will be explained by some extension to the SM is not only well motivated, it could also hold the key to solving other outstanding problems.

In order for DM candidates to be viable, they need to be created in the early universe, producing the correct relic abundance we observe in the CMB. Once a model and a production mechanism is chosen, constraints and predictions follow. However, as shown above there is no shortage of DM models and as will be shown below, there are multiple production mechanisms. When considering the early universe, thermodynamic principles are particularly helpful. If there is some non-gravitational coupling between DM and SM matter, as is predicted by many BSM theories, the number density, n_χ , of DM is described by the Boltzmann equations,

$$\dot{n}_\chi + 3Hn_\chi = \frac{g_\chi}{(2\pi)^3} \int C[f] \frac{d^3p_\chi}{E_\chi}, \quad (1.16)$$

where g_χ is the internal degrees of freedom, p_χ is the three-momentum and E_χ is energy. C is the collisional operator and depends on the specific model, i.e. which processes change the number density, n_χ . For example, a model that connects DM particles, χ and the SM particles, f , via $2 \rightarrow 2$ scattering only, leads to the Boltzmann equation

$$\dot{n}_\chi + 3Hn_\chi = n_f^2 \langle \sigma v \rangle_{f\bar{f} \rightarrow \chi\bar{\chi}} - n_\chi^2 \langle \sigma v \rangle_{\chi\bar{\chi} \rightarrow f\bar{f}}, \quad (1.17)$$

where $\langle \sigma v \rangle$ is the thermally averaged cross-section defined by

$$\langle \sigma v \rangle_{\chi\bar{\chi} \rightarrow f\bar{f}} \equiv \frac{1}{n_{\chi, \text{Eq}} n_{\bar{\chi}, \text{Eq}}} \int \frac{d^3 p_{\bar{\chi}}}{2E_{\bar{\chi}}} \frac{d^3 p_\chi}{2E_\chi} \sigma_{\chi\bar{\chi} \rightarrow f\bar{f}} \exp[-(E_\chi + E_{\bar{\chi}})/T], \quad (1.18)$$

where T is temperature. Thermally averaged decay rates $\langle \Gamma \rangle$ can be defined similarly. Assuming that \mathcal{CP} is not violated implies that $\langle \sigma v \rangle_{f\bar{f} \rightarrow \chi\bar{\chi}} = \langle \sigma v \rangle_{\chi\bar{\chi} \rightarrow f\bar{f}}$, leads to the simplification

$$\dot{n}_\chi + 3Hn_\chi = \langle \sigma v \rangle (n_f^2 - n_\chi^2). \quad (1.19)$$

SM particles in the early universe are in equilibrium and thus follow the corresponding thermal number densities,

$$n_{\text{rel}} = g \varepsilon_{\text{FB}} \frac{\zeta(3)}{\pi^2} T^3 \quad \text{and} \quad n_{\text{nr}} = g \left(\frac{mT}{2\pi} \right)^{3/2} e^{(\mu-m)/T}, \quad (1.20)$$

depending on whether they are relativistic or not at a given temperature. The constant ε_{FB} is just a numerical factor that is $3/4$ for Fermions and 1 for Bosons. The condition where a particle species can maintain thermal equilibrium is that the particle interaction rate, in our $2 \rightarrow 2$ example, annihilation rate, $n_\chi \langle \sigma v \rangle$, must be greater than the expansion rate, $H(t)$. As the universe cools and expands, the annihilation rate can drop below $H(T)$, at which point, the particle no longer interacts quickly enough and its comoving number density, $Y = n/s$, freezes-out. This behavior is captured by modifying Eq.(1.17) to,

$$\frac{dY}{dT} = \frac{\langle \sigma v \rangle s}{HT} (Y_\chi^2 - Y_{\text{eq}, \chi}^2), \quad (1.21)$$

where we used the conservation of entropy, i.e. sR^3 is a constant and assumed

that this process happens in the radiation dominant era so that $\dot{T} = -HT$. In the relativistic limit, $Y_{\text{eq},\chi}$, is temperature independent, meaning that the late time value for Y is simply the equilibrium value evaluated at the time of freeze out. The number density of an equilibrium species and a decoupled species today differ because the number of radiation degrees of freedom contributing to the radiation energy density, g_* , and the radiation degrees of freedom contributing to the radiation entropy density, g_{s*} change over time. They are approximately given by

$$g_* = \sum_{\text{bosons}} g_i \left(\frac{T_i}{T}\right)^4 + \frac{7}{8} \sum_{\text{fermions}} g_i \left(\frac{T_i}{T}\right)^4, \quad (1.22)$$

$$g_{s*} = \sum_{\text{bosons}} g_i \left(\frac{T_i}{T}\right)^3 + \frac{7}{8} \sum_{\text{fermions}} g_i \left(\frac{T_i}{T}\right)^3, \quad (1.23)$$

where the T_i/T factors are relevant for particles that remain relativistic but are no longer in thermal equilibrium, i.e. T_i is the temperature of decouples species i . The relationship of g_{s*}^2/g_* over temperature is shown in Figure 1.5.

As a concrete example the neutrinos freeze out at $T \sim 1$ MeV, meaning that their density is given by

$$\Omega_\nu h^2 = \frac{\sum_i s_0 Y_{\text{eq}}(T_f) h^2 m_{\nu_i}}{\rho_c} = \frac{\sum_i m_{\nu_i}}{91 \text{ eV}}, \quad (1.24)$$

where we have summed over different generations of active neutrinos. We see here that if we wanted neutrinos to play the role of hot DM, i.e. that $\Omega_\nu h^2 = 0.11$ we would need the masses of the three generations to sum to ~ 9 eV, which is of orders of magnitude higher than experimental upper bounds of 0.12 eV [60]. SM neutrinos could contribute to the measured abundance of DM in our universe, however not all measurements, our strongest measurements of the Ω_{DM} come from the CMB. SM neutrinos were relativistic at the time of recombination and therefore would not contribute to this measurement of Ω_{DM} . The effects of massive neutrinos could be felt in later stage structure formation [61].

Speculating that a relativistic particle which is coupled via a BSM gauge boson

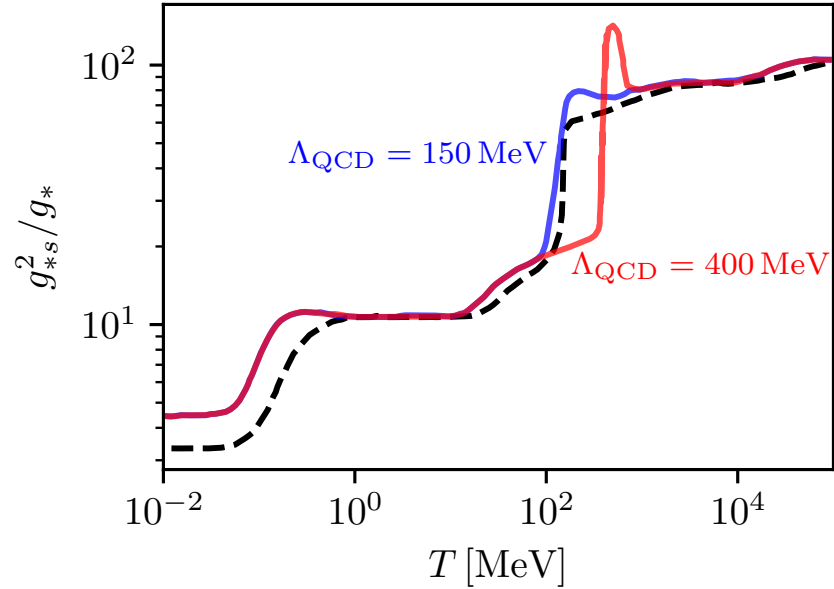


Figure 1.5: The dashed line comes from the simply counting the relativistic degrees of freedom in both Eq.(1.22) and Eq.(1.23) as contributions to the energy and entropy density respectively. Ref. [62] calculates these contributions more precisely and considers the QCD phase transition at different temperatures, which we show with solid lines. We see that the approximation holds up fairly well.

that is heavier than the weak scale, $M_{\text{BSM}} > M_Z$, doesn't help either because the changing g_* values provide the result

$$\Omega_\chi h^2 = \frac{m_\chi}{910 \text{ eV}}, \quad (1.25)$$

suggesting still a very light DM particle. A relativistically produced DM of these masses would not cool quickly enough to provide small density perturbations seen in the CMB.

For a non-relativistic particle the equilibrium comoving number density is

$$Y_{\text{eq,nr}} = \frac{45g}{2\pi^4 g_*} \sqrt{\frac{\pi}{8}} \left(\frac{m}{T}\right)^{3/2} e^{-m/T}. \quad (1.26)$$

Therefore, after introducing the variable $x = m/T$, eq.(1.21) becomes,

$$\frac{dY}{dx} = -\lambda x^{-2} \left(Y_x^2 - \bar{Y}_x^2\right), \quad (1.27)$$

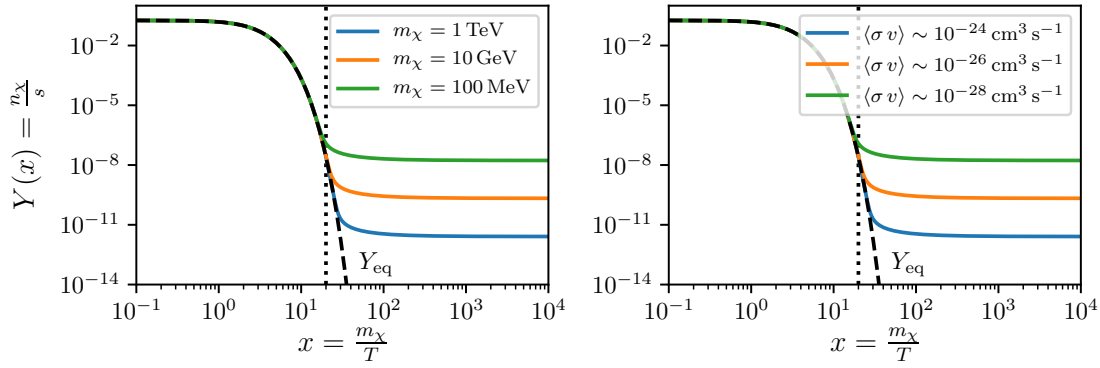


Figure 1.6: Numerical solutions to eq.(1.27) for different values of m_χ on the left and $\langle\sigma v\rangle$ on the right. A dotted line at $x = 20$ is included to show limited variation.

where

$$\lambda \simeq 0.264 \left(g_{*s}/g_*^{1/2} \right) M_{\text{Pl}} m_\chi \langle\sigma v\rangle, \quad (1.28)$$

The ratio between g_{*s} and $g_*^{1/2}$ is usefully shown in Figure 1.5. In this limit, we can expand $\langle\sigma v\rangle$ in powers of v via the plane-wave expansion,

$$\langle\sigma v\rangle \approx \langle\sigma v\rangle_s + \langle\sigma v\rangle_p v^2 + \dots \quad (1.29)$$

where the subscripts are named in accordance with plane-wave scattering nomenclature. Since $v^2 \sim T/m$, the highest order of $\lambda(x)$ is independent of velocity, i.e. x^0 .

Figure 1.6 shows the general behaviour of Y_χ as it freezes out. For a large range of masses and cross sections, the freeze out temperature is $T_f \sim 20m_\chi$. We see that Y_∞ is quite sensitive to m_χ , but since the $\rho_\chi = s_0 Y_\infty/m_\chi$ the constraint of the CMB fairly insensitive to mass, with the approximate result $\langle\sigma v\rangle \simeq 3 \times 10^{-26} \text{ cm}^3 \text{ s}^{-1}$ across the GeV to TeV range. This value for σ is very similar to that of electroweak processes. A coincidence dubbed the "WIMP miracle" which initially was very encouraging for the many extensions of the SM that predicted new physics at the weak scale.

Approximating an annihilation cross section of some weak-scale interaction $\sigma \sim$

$G_F^2 m_\chi^2$ leads to the Lee-Weinberg [63, 64] bound $m_\chi \gtrsim 6$ GeV and requiring that unitarity is respected leads to an upper bound $m_\chi \lesssim 100$ TeV [65]. Both bounds can be avoided, for example, the upper bound is alleviated for composite DM candidates and the lower bound can be circumvented for certain scalar models [66]. Despite this, these two bounds tend to define the mass window usually considered when WIMPs are being discussed. As we will see, this mass range is where many experiments are most sensitive and therefore able to probe these thermally produced candidates.

A particular DM interaction with the SM that we return to throughout this thesis is known as anapole DM [67] interaction. This refers to the lowest dimension operator that couples a Majorana fermion and a photon and respects \mathcal{CPT} symmetry,

$$\mathcal{A} \bar{\chi} \gamma^\mu \gamma^5 \chi \partial^\nu F_{\mu\nu}, \quad (1.30)$$

where $F_{\mu\nu}$ is the electromagnetic field strength tensor and \mathcal{A} has mass dimension -2 parameter, which can be mapped on to the parameters of a higher energy theory. In comparison, a Dirac fermion, has many higher dimension terms that couple to the photon including dimension 5 operators such as the magnetic and electric dipoles, making current experimental constraints more prohibitive. DM being Majorana by nature provides one with a tantalizingly simple reason for DM being so dark. Assuming that Eq.(1.30) is the only relevant interaction for annihilation, the thermally average cross section in the small m_f limit is

$$\langle \sigma_{\chi\bar{\chi} \rightarrow f\bar{f}v} \rangle = 4\mathcal{A}^2 \alpha m_\chi^2 \left(\frac{1}{x} \right) \quad (1.31)$$

where α is the fine structure constant. Notice here that this is a pure P-wave contribution, which is a consequence of Pauli blocking, where the incoming Majorana particles must have opposite spin. As we will see in Chapter 6 a more complete UV model of Majorana DM may provide alternate channels for annihilation, but the suppression of S-wave contributions remains.

More varied dark sectors are easily incorporated into this framework by introducing coupled Boltzmann equations [68]. If the mass splitting between the DM candidate and the next lightest dark sector particle is small, then the process of co-annihilation takes place, which often works by depleting the abundance, allowing for stronger couplings.

The assumption that DM at some point was in thermal equilibrium with the SM is not completely necessary to create the correct relic abundance. If the coupling to the SM is so weak that equilibrium is never achieved, the thermal bath will be able to produce DM in effectively a one way process. This leads to a slow arrival to a stable abundance. This scenario is known as the Freeze-in mechanism and provides models that couple exceptionally weakly to the SM a way to be realised as DM. These candidates are known as Feebly Interacting Massive Particles (FIMPs) [69, 70] and can produce the correct relic abundance for a wide range of masses, typically between eV and TeV. Despite the fact that FIMPs have never reached thermal equilibrium, they have been created with energy from the SM bath. If scattering is possible among the FIMPs they themselves may thermalise and reach equilibrium [71]. Other such FIMPs may be metastable and decay into a thermal DM candidate, such is the scenario of SuperWIMPs [72]. SuperWIMPs increase their abundance by the metastable decay, meaning their connection to the SM can be small.

Somewhat similar to the freeze in mechanism is the process where sterile neutrinos are created through neutrino mixing [73–75], this can result in what are known as warm DM candidates. Like in the relativistic freeze out scenario above, sterile are produced with enough kinetic energy to wash out structures that might be observable. However, if they are in the keV range, they will only affect objects below the size of a galactic sub-halo. These are known as warm DM candidates as opposed to cold DM. Determining whether DM is cold or warm is an active discussion in the community [76, 77].

The creation mechanisms above rely on fairly ordinary thermodynamic frameworks, non-thermal mechanisms are also known for the production of cosmic relics. Some of which are produced gravitationally during inflation or reheating such as WIMPZillas [78] or Despicable DM [79], they tend to predict very large masses $m_\chi > 10^{12}$ GeV. However, the misalignment mechanism [80] is a non-thermal process that allows for very light DM candidates. It occurs when a shift symmetry is broken such that a scalar field becomes very slightly massive. This scalar field in the expanding universe evolves as

$$\ddot{\phi} + 3H\dot{\phi} + m^2\phi = 0. \quad (1.32)$$

The solution of which gives a matter like evolution in the universe, i.e. $\rho_\phi \approx R^{-3}$. This mechanism is typically associated with ALPs which have some associated global U(1) symmetry breaking. The lower bound ($m_\chi < 10^{-28}$ GeV) comes from the de Broglie wavelength of ϕ having to be smaller than dwarf spheroidal galaxies.

It is clear that there are many different ways in which DM could be realised in our Universe. The above production mechanisms show that we have not constrained the possibilities much, motivating greater experimentation. Figure 1.7 schematically shows the three directions for detecting DM. These are known as indirect detection, collider detection and direct detection.

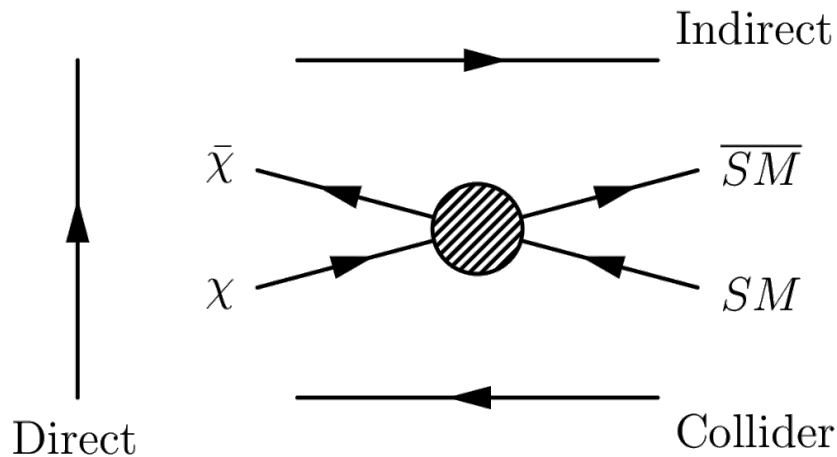


Figure 1.7: The different avenues for DM detection.

Indirect detection applies to models in which DM can annihilate or decay into some SM particles, depicted by Figure 1.7, reading the diagram left to right. Many models that are produced through thermal freeze out would produce detectable signals, with the exception of those with P-wave thermal cross sections. If the products of annihilation or decay are photons or neutrinos, they would travel to earth unperturbed. Satellite and ground based telescopes look to regions of high DM density like the center of the Milky Way, to test DM models. The Fermi Large Area Telescope (LAT) [81] is able to constrain annihilation into photons in the mass region of 100 MeV – 100 GeV. However, studies of a gamma ray excess in the center of the Milky Way have shown that the astrophysical background is difficult to separate [82]. Dwarf spheroidal galaxies are a clean DM structure to look for signals [83] because they do not contain many background sources of gamma-ray, on the other hand, they carry larger uncertainties associated with the DM structure. For masses above 100 GeV the experiments HESS [84] and HAWC [85] are more sensitive. Neutrino detectors such as IceCube [86] and Antares [87] detect high energy neutrinos as well as the direction of the source, enabling them to constrain certain sources, such as the Galactic center or the Sun, which may contain an increased DM density within it [88].

Signatures of diffuse particles in the interstellar medium such as antiprotons and positrons can be used to constrain DM models. If there is equal amounts of DM and anti DM as in the WIMP case, this could produce more SM antiparticles than predicted by astrophysics. Experiments such as AMS-02 [89] and PAMELA [90, 91] were able to constrain models in between 100 MeV – 1 TeV in DM mass.

There are a number of puzzling anomalies coming from indirect detection, such as the Galactic center excess [92, 93] and high energy IceCube events [91, 94, 95], however for the purpose of this thesis, we take the position that these are not DM events and they will be explained by astrophysics. In Chapter 6 we will incorporate constraints

from indirect detection to test a phenomenologically motivated model.

Collider searches specifically refer to the processes where DM is created via SM collisions. If the mediator particles connecting DM to the SM are heavy as with many scenarios, high energy collisions are required to produce DM efficiently. Pair production as shown in Figure 1.7 actually leaves no signature in detectors. Therefore processes that emit some visible signature as well as producing DM are constrained, such as the mono-X plus missing transverse energy signature, where X can be a jet, photon or Z^0 . The jet is required for the detector to tag the event, otherwise, the production of the DM would not be detected. Currently, the LHC [96, 97] is searching for such signals and in Chapter 6 we comment more on specific channels and future colliders.

Assuming the mediating particle has a mass much higher than the transfer momentum q , one can use an effective field theory (EFT) approach. This uses experimental data to constrain non-renormalisable operators such as,

$$\frac{\bar{\chi}\gamma_{\mu}\chi\bar{q}\gamma^{\mu}q}{\Lambda^2} \quad \text{and} \quad \frac{\bar{\chi}\gamma_{\mu}\gamma^5\chi\bar{q}\gamma^{\mu}\gamma^5q}{\Lambda^2}. \quad (1.33)$$

EFTs are most effective when you can be sure that new physics is much heavier than q . This may not be the case with the LHC. Therefore, the simplified model framework was introduced in Ref. [98] to avoid the possible break down of any EFT. In this framework, DM is accompanied by a single mediator, which has certain couplings depending on its nature. For example, a scalar mediator will only interact via scalar and psuedo-scalar interactions at tree-level.

As of yet, collider searches have not observed any non-SM signal, and therefore place constraints on DM models. In the event that DM is light and very weakly connected to the SM, perhaps by a light mediator also, searches by fixed target experiments like SHiP [99] are important. They use high luminosities to search for these new

mediators. This in essence is similar to the collider direction in Figure 1.7.

Direct detection attempts to observe scattering interactions between DM and SM matter by measuring the energy deposition from a scattering. Commonly, elastic scattering is assumed and target materials are placed in underground facilities [100,101]. A worldwide experimental effort has resulted in extremely sensitive experiments, which have probed DM interactions with ordinary matter with unprecedented precision. In the absence of confirmed DM signal, stringent upper bounds on the DM elastic scattering cross section with nuclei have been reported [102–108].

Currently, detectors that use dual phase time projection chambers (TPC), such as LUX [109], Xenon-1T [102], and PandaX [104], dominate the search for DM masses above 10 GeV. These searches utilize two types of signals: a prompt photon signal from the scintillation in the liquid xenon and a proportional charge signal amplified in the gas phase. The ratio of the two allows to distinguish electron from neutron recoils. The position of the interaction in the TPC can be determined from the drift times and light pattern of the signals, allowing to define a background-free fiducial volume due to self-shielding. The next-generation of liquid noble gas detectors, using xenon (such as LZ [110], XENONnT [111], and DARWIN [112]) or argon (DarkSide-20k [113] and DEAP [114]) will probe the parameter space of weakly interacting massive particles (WIMPs) with unprecedented precision.

However, since these experiments typically have a threshold energy of around \sim few keV, with the exception of the DarkSide-50 result [115], constraining lower mass DM is difficult. Experiments based on crystal detectors such as the germanium, SuperCDMS [116] and calcium tungstate, CRESST [107] have made substantial gains in the quest to lower the energy threshold of direct detection experiments. These experiments are capable of detecting energy deposition via phonons, however CDMS can detect ionization while CRESST detects scintillation signals. Furthermore, the

experiment NEWS-G [117] utilises new spherical proportional counters and light noble gases to search for light DM. Due their relatively light nuclei as well as low thresholds, these experiments are the prominent players in constraining DM masses below ~ 6 GeV. This comes at the price however, as these collaborations have less exposure than their heavier counterparts and therefore do not reach the same level of sensitivity.

There have been interesting recent developments both theoretically and experimental to explore other technologies for direct detection of dark matter. These have looked mainly at low mass DM models [118], which look for electron recoils, through a variety of different methods. This has also prompted the more traditional direct detection experiments to interpret their data to constrain electron recoils. For larger masses some novel searches of current experiments are being proposed [119] as well as some futuristic alternatives [120]. Within a similar mass range of the noble gas experiments, paleo-detectors [121] have recently been proposed, as well as directional detectors [122].

This Thesis reviews contributions made to the field of DM particle phenomenology, with a specific focus on what can be learned from direct detection experiments as a standalone technology and withing more global analysis strategies.

Chapter 2 expands more on the principles of direct detection, with particular attention to nuclear recoils, developing the Non-Relativistic Effect Field Theory (NREFT) framework [123, 124]. This framework was developed to allow for more model independent analyses of direct detect experiments. This prompts the discussion in Chapter 3 which reviews how data from direct detection can be interpreted statistically and how that can fit in with efforts to reconstruct parameters in the event of detection.

Chapter 4 is based on Ref. [1] and introduces RAPIDD, a surrogate model that speeds up the computation of the nuclear recoil spectrum of dark matter particles in direct detection experiments. RAPIDD replaces the exact calculation of the nuclear responses by ordinary polynomials, providing a very fast evaluation of parameter space. We validate this method on the multi-dimensional parameter space resulting from the NREFT description and include astrophysical uncertainties in the description of the dark matter halo. To demonstrate the power of this tool, we study the complementarity of different targets to discriminate simplified dark matter models.

Chapter 5 presents an investigation into the benefits of increasing the maximum nuclear recoil energy analysed in direct detection experiments [2]. In agreement with previous literature, we show that, an increased maximum energy leads to more stringent upper bounds on the DM-nucleus cross section for the NREFT operators, especially those with an explicit momentum dependence. We extend the energy region of interest to show that the optimal values of the maximum energy for xenon and argon are of the order of 500 keV and 300 keV, respectively. We then show how, if a signal compatible with DM is observed, an enlarged energy region of interest leads to a better measurement of the DM mass and couplings. We do this in two and three-dimensional parameter space. We find that this modification is an excellent way to identify the linear combination of momentum-dependent and momentum-independent operators. Finally, we show enlarging the analysis window allows us to test astrophysical parameters of the DM halo, such as the DM escape speed.

Chapter 6 presents an extension of the Standard Model that addresses the hints of lepton flavour universality violation observed in $B \rightarrow K^{(*)}l^+l^-$ decays at LHCb, while providing a viable candidate for DM [3]. The combination of cosmological and flavour constraints sets an upper limit on the dark matter and mediator masses. Using understanding from previous chapters, we predict the direct detection response

to determine whether the DM candidate can be Majorana or Dirac. Studying LHC dijet and dilepton searches, lower bounds on the dark matter and mediator masses can be set. Combining LHC constraints with the sensitivity of current and future direct detection experiments show that parts of the parameter space could be accessible in the future to multi-ton experiments. Future collider and direct DM searches complement each other to probe large areas of the parameter space for this model.

Finally in Chapter 7 concludes this thesis by reviewing the results presented, places the work within the wider search for DM and comments on prospects moving forward.

Chapter 2

Direct Detection of Dark Matter

In this chapter, we review the direct detection of DM. After discussing the general principles, we focus on the effective theory approach developed in Refs [123,124]. In Section 2.2, we provide examples of how one can trace parameters from the higher energy Lagrangian to the non-relativistic effective theory (NREFT), making use of nuclear response functions. Finally, in Section 2.3 we will review the current state-of-the-art results from direct detection experiments.

The standard picture of DM given in Chapter 1 is that the dark matter halo extends much further from the Galactic center than the observable matter. Therefore an experiment on the Earth would be immersed in the halo and may be able to detect local DM. The DM particles, here χ , traversing through the Earth would deposit some energy via scattering. For purely gravitational interactions this effect is minuscule but, with electroweak-scale interactions as expected for many candidates, interactions could be detectable.

As with any collisional process, the number of events N is given by the flux, Φ ,

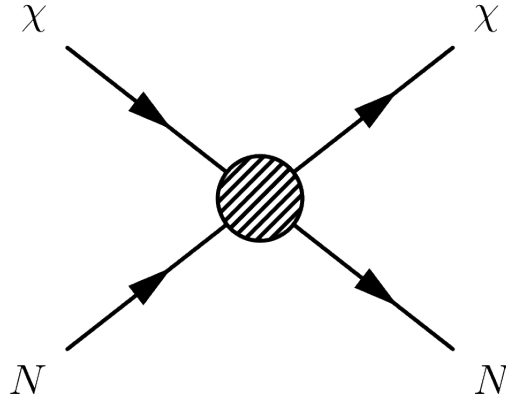


Figure 2.1: DM interacting with nucleons. The incoming and outgoing DM particles have momenta of \vec{p} and \vec{p}' , respectively, whereas incoming and outgoing nucleons have momenta \vec{k} and \vec{k}' , respectively. We choose the transfer momentum to be defined by $\vec{q} = \vec{p} - \vec{p}' = \vec{k}' - \vec{k}$

multiplied by the interaction cross-section and time. The flux of the incident DM depends on the number density, n_χ , which can be related to the local density, ρ_0 , its mass, m_χ , and the incident velocity, v , described by a distribution, $f(\vec{v})$. The expected event rate in a given energy bin, k , is then given by

$$N_k = \epsilon \int_{E_k}^{E_{k+1}} dE_R \frac{dR}{dE_R} = \frac{\rho_0 \epsilon}{m_T m_\chi} \int_{E_k}^{E_{k+1}} dE_R \int_{v_{min}} d^3v v f(\vec{v}) \frac{d\sigma_{\chi T}}{dE_R}, \quad (2.1)$$

where in the first equality, dR/dE_R , is the differential rate, often presented in differential rate units ($\text{dru} = (\text{kg days keV})^{-1}$), and is expanded in the second equality. The exposure, ϵ , is the product of detector mass, which is related to target nuclei mass, m_T and time. The integral limit v_{min} refers to the minimum velocity required to induce a recoil of energy E_R , calculated from basic kinematics,

$$v_{min} = \sqrt{m_T E_R / 2\mu_T^2} \quad (2.2)$$

where μ_T^2 is the DM-nucleus reduced mass.

The particle physics nature of the DM is encoded in the DM-nucleus differential scattering cross section, $d\sigma_{\chi T}/dE_R$ and is schematically depicted in Figure 2.1 with a blob representing any short distance physics occurring. The incoming and outgoing

DM particles, χ , have \vec{p} and \vec{p}' momenta, respectively. For the nucleon, N , they have momenta \vec{k} and \vec{k}' ¹. The transfer momentum is therefore $\vec{q} = \vec{p} - \vec{p}' = \vec{k}' - \vec{k}$. Note that processes like inelastic scattering, either the nucleon or DM could be excited to a higher energy state N' or χ' . We introduce the vectors $\vec{K} = \vec{k} + \vec{k}'$ and $\vec{P} = \vec{p} + \vec{p}'$ to keep some of the results later more concise.

Taking a DM mass on the lower end of the typical WIMP window, where $m_\chi < m_T$, and using 2.2, the maximum energy DM could deposit to a given target is proportional to both masses, $E_R \propto m_\chi^2/m_T$. For example, the Milky-Way escape velocity, $v_{\text{esc}} \sim 600 \text{ km s}^{-1}$ means that a $m_\chi \sim 6 \text{ GeV}$ DM particle will maximally be able to recoil a xenon atom by $\sim 1 \text{ keV}$. At the heavier end, DM mass becomes irrelevant and the maximum energy deposited is $\propto m_T$, for xenon we have $\sim 1 \text{ MeV}$. We will see in Chapter 5, that the point at which the maximum energy deposit becomes insensitive to DM mass is itself dependent on the target material, for Xenon this is just above $\sim 500 \text{ GeV}$.

2.1 Effective Theory of DM-nucleus interactions

The effective field theories most familiar to particle physicists are relativistic, where the known field content is combined in a gauge and Lorentz invariant way to produce a series of higher dimensional operators as discussed in Chapter 1. These operators are parameterised by their Wilson coefficients, c^i ,

$$\mathcal{L} = \mathcal{L}_{\text{SM}} + \sum_i \frac{c_{(5)}^i}{\Lambda} \mathcal{O}_i^{(5)} + \sum_i \frac{c_{(6)}^i}{\Lambda^2} \mathcal{O}_i^{(6)} + \dots, \quad (2.3)$$

and Λ is the scale of new physics. In the non-relativistic regime however, the relevant degrees of freedom are presumed to be Galilean invariant. These are quantities, such

¹Often the nucleon is taken to be at rest initially.

as the transfer momentum, \vec{q} , incident velocity, \vec{v} , and spins of the nucleons and the DM particles, \vec{S}_N, \vec{S}_χ . The resulting non-relativistic effective field theory (NREFT) is then described in terms of a Lagrangian that contains four-fermion operators of elastic scattering between a DM particle and a target nucleon,

$$\mathcal{L}_{\text{int}} = \sum_N \sum_i c_i^N \mathcal{O}_i \chi^+ \chi^- N^+ N^-. \quad (2.4)$$

In this expression, N^\pm, χ^\pm are non-relativistic fields, which are simply constructed out of quantum mechanical annihilation and creation operators. The sums over N and i are over the nucleons and operators respectively. The coefficients, c_i^N , are real parameters that will be related to the high energy theory. The operator variables of the effective Lagrangian must be invariant under Galilean transformations, which we build from the relevant degrees of freedom. Also, since interactions must be Hermitian, its customary to build operators out of Hermitian pieces,

$$i\vec{q}, \quad \vec{v}^\perp = \vec{v} + \frac{\vec{q}}{2\mu_N}, \quad \vec{S}_\chi, \quad \vec{S}_N, \quad (2.5)$$

where \vec{v}^\perp is defined such that $\vec{v}^\perp \cdot \vec{q} = 0$ due to energy conservation. If one assumes that the scattering is mediated at most by a spin-1 particle, then at most the resultant non-relativistic operator can only be quadratic in \vec{q} and \vec{v}^\perp , limiting the number of operators quite significantly. These have been summarized in table 2.1.

Notice that there is no \mathcal{O}_2 in table 2.1, this is simply the operator v^2 , which is often discarded as it cannot be produced at leading order in the non-relativistic limit [124].

For the non-relativistic fields in Eq.(2.4) we have the choice to normalise them such that their mass dimension is 1 or 3/2, so the coefficients are dimensionless or have mass dimension -2 . In the relativistic case in Eq.(2.3) the coefficients are often redefined to absorb the cut-off scale Λ , i.e. $[c_{(d)}] = \text{mass}^{-d}$. This gives an estimate for the lower limit of the new physics scale. With the NREFT Lagrangian, there is no mass scale to explicitly absorb, but by choosing the field normalisation, one

q -independent	q -dependent
$\mathcal{O}_1 = 1_X 1_N$ $\mathcal{O}_4 = \hat{\mathbf{S}}_X \cdot \hat{\mathbf{S}}_N$ $\mathcal{O}_7 = \hat{\mathbf{S}}_N \cdot \hat{\mathbf{v}}^\perp$ $\mathcal{O}_8 = \hat{\mathbf{S}}_X \cdot \hat{\mathbf{v}}^\perp$ $\mathcal{O}_{12} = \hat{\mathbf{S}}_X \cdot [\hat{\mathbf{S}}_N \times \hat{\mathbf{v}}^\perp]$	$\mathcal{O}_3 = i\hat{\mathbf{S}}_N \cdot \left[\frac{\hat{\mathbf{q}}}{m_N} \times \hat{\mathbf{v}}^\perp \right]$ $\mathcal{O}_5 = i\hat{\mathbf{S}}_X \cdot \left[\frac{\hat{\mathbf{q}}}{m_N} \times \hat{\mathbf{v}}^\perp \right]$ $\mathcal{O}_9 = i\hat{\mathbf{S}}_X \cdot \left[\hat{\mathbf{S}}_N \times \frac{\hat{\mathbf{q}}}{m_N} \right]$ $\mathcal{O}_{10} = i\hat{\mathbf{S}}_N \cdot \frac{\hat{\mathbf{q}}}{m_N}$ $\mathcal{O}_{11} = i\hat{\mathbf{S}}_X \cdot \frac{\hat{\mathbf{q}}}{m_N}$ $\mathcal{O}_{13} = i \left[\hat{\mathbf{S}}_X \cdot \hat{\mathbf{v}}^\perp \right] \left[\hat{\mathbf{S}}_N \cdot \frac{\hat{\mathbf{q}}}{m_N} \right]$ $\mathcal{O}_{14} = i \left[\hat{\mathbf{S}}_X \cdot \frac{\hat{\mathbf{q}}}{m_N} \right] \left[\hat{\mathbf{S}}_N \cdot \hat{\mathbf{v}}^\perp \right]$
q^2 -dependent	
$\mathcal{O}_6 = \left[\hat{\mathbf{S}}_X \cdot \frac{\hat{\mathbf{q}}}{m_N} \right] \left[\hat{\mathbf{S}}_N \cdot \frac{\hat{\mathbf{q}}}{m_N} \right]$ $\mathcal{O}_{15} = - \left[\hat{\mathbf{S}}_X \cdot \frac{\hat{\mathbf{q}}}{m_N} \right] \left[(\hat{\mathbf{S}}_N \times \hat{\mathbf{v}}^\perp) \cdot \frac{\hat{\mathbf{q}}}{m_N} \right]$	

Table 2.1: List of non-relativistic EFT operators for spin-1/2 and spin-1 DM particles, classified according to their dependence on the momentum exchange.

can have c 's with mass dimension -2 . Physical results of course are independent of these choices.

Since the non-relativistic fields are constructed with just creation and annihilation operators and there are no propagators in the diagram (Figure 2.1), no subtlety is required for calculating the matrix element,

$$\mathcal{M}_N = \sum_N \sum_i c_i^N \mathcal{O}_i. \quad (2.6)$$

The total DM-nucleus matrix element squared is calculated by evaluating these contributions coherently over the entire nucleus. This requires state of the art nuclear physics calculations, the results from which have been provided in the literature [123–126] and are parameterised by nuclear form factors $\mathcal{F}_{i,j}^{N,N'}$,

$$|\overline{\mathcal{M}_T}|^2 = \frac{m_T^2}{m_N m_{N'}} \sum_{N,N'} \sum_{i,j} c_i^N c_j^{N'} \mathcal{F}_{i,j}^{N,N'}, \quad (2.7)$$

where here the coefficients are chosen to be dimensionless. These form factors have very different amplitudes due to how the contributions sum coherently. For example, \mathcal{O}_1 couples to the number of nucleons in atoms which leads to the classic enhancement by atomic number squared, A^2 . In Figure 2.2 we show how these different operator responses have different relative sizes by plotting the differential rates resulting

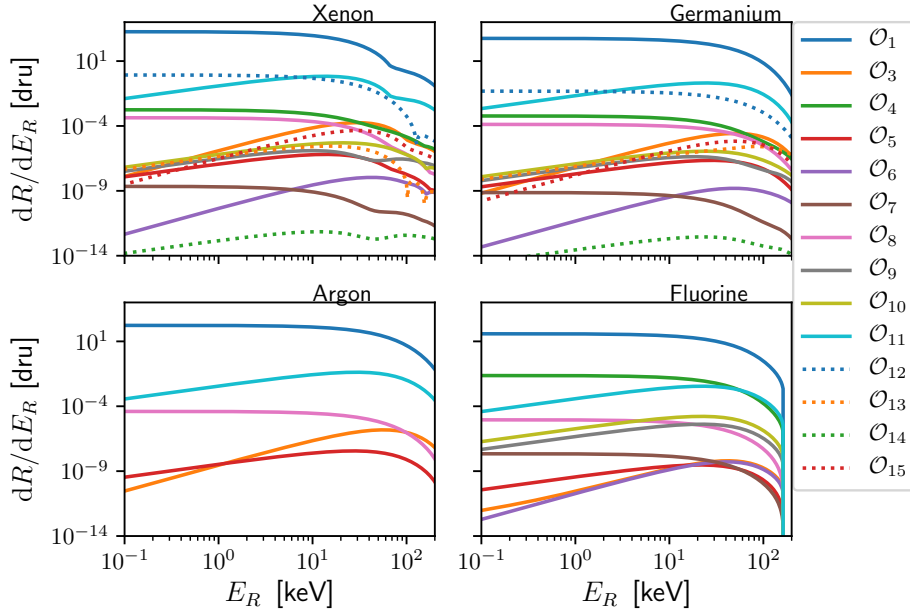


Figure 2.2: Recoil spectra for a number of common operator responses. All spectra are calculated with couplings $c_i = 1$ to give an impression of the difference in size of the responses. The mass of the DM particle provoking these spectra is $m_\chi = 100$ GeV.

from setting each operator coefficient to 1. Figure 2.2 also shows that the strength of operator response is also somewhat dependent of the target material, we have shown responses from common targets, xenon, germanium, argon and fluorine.

The spectral bumps that can be seen in xenon panel in Figure 2.2, are typical of form factors, however, since numerous isotopes are present for xenon, these resonances are smoothed out somewhat. We see that the simpler isotopes of germanium, argon and fluorine do not exhibit such resonant behaviour. One cause of the different spectra between targets is the relation (2.2). We notice that the fluorine spectra abruptly vanishes at $E_R \sim 150$ keV, this is simply the endpoint of the spectra for fluorine, which is lower than for the other target materials since it is relatively light and therefore the point where incident DM would have to be traveling at velocities greater than v_{esc} is reached earlier.

When calculating the interaction coherently over the nucleus, overlapping modes can

lead to interference terms between the following pairs of EFT operators, $(\mathcal{O}_1, \mathcal{O}_3)$, $(\mathcal{O}_4, \mathcal{O}_5)$, $(\mathcal{O}_4, \mathcal{O}_6)$, and $(\mathcal{O}_8, \mathcal{O}_9)$. Furthermore, there will always be interferences between the proton and neutron contributions across the same EFT operator, if the sign of nucleon couplings are opposite, cancellations occur. Once we have $|\overline{\mathcal{M}}_T|^2$ we can obtain the differential cross-section from standard quantum field theory [50],

$$d\sigma = \frac{1}{(2E_1)(2E_2)|\vec{v}_1 - \vec{v}_2|} |\overline{\mathcal{M}}|^2 d\Pi_{\text{LIPS}}, \quad (2.8)$$

where Π_{LIPS} is the Lorentz invariant phase space. Since direct detection experiments are insensitive to recoil direction but sensitive to recoil energy, the differential cross-section is written in the form,

$$\frac{d\sigma_{\chi T}}{dE_R} = \frac{m_T}{32\pi m_\chi^2 m_N^2} \frac{1}{v^2} \sum_{ij} \sum_{N, N'=n,p} c_i^N c_j^{N'} \mathcal{F}_{i,j}^{N, N'}(v^2, q^2), \quad (2.9)$$

which can be directly plugged into Eq. (2.1) to give the number of expected recoils in a particular energy range for a given exposure. If one had chosen the normalisation where the coefficients had mass dimension -2 , our differential cross section would be

$$\frac{d\sigma_{\chi T}}{dE_R} = \frac{m_T}{2\pi} \frac{1}{v^2} \sum_{ij} \sum_{N, N'=n,p} c_i^N c_j^{N'} \mathcal{F}_{i,j}^{N, N'}(v^2, q^2). \quad (2.10)$$

When presenting results, often the dimension -2 coefficients are multiplied by factors of the Higgs vacuum expectation value $m_v \approx 246$ GeV to estimate the scale of new physics that is mediating between DM and the SM. Interestingly however, the NREFT is not contingent on the mediator itself being heavy. As long as the incoming and outgoing particles are non-relativistic, it is consistent to incorporate light mediators into this framework.

2.2 Matching the relativistic and non-relativistic theories

In this section we will outline the procedure for going from some relativistic Lagrangian to the non-relativistic one. After introducing the general procedure, we give some illustrative examples.

The objective is to rewrite the high energy Lagrangian in terms of non-relativistic one in Eq. (2.4). First, one needs to express the Lagrangian in terms of the DM and SM currents $\mathcal{J}_{\text{DM}}\mathcal{J}_{\text{SM}}$. These currents can have a complicated Lorentz structure which depends on the underlying physics. In a t-channel scattering, the two currents are connected via a mediating particle, introducing a propagator term $\sim \frac{1}{q^2 - M^2}$, where M is the mass of the mediator. The limit where M is large is usually taken, allowing the propagator to be treated as simple contact operator. For direct detection, the typical transfer momentum in DM-nuclei interactions is $\sim \text{keV}$ and for many models of interest, mediator masses are indeed much larger. The mass dependence is usually absorbed into the coefficients at this point and normalised to the Higgs vacuum expectation value, this choice is made because in several well motivated DM models, the electroweak scale appears.

In the canonical view of EFTs, the integration of the mediator is the essential part of an effective field theory. However, for this effective theory, this is not necessary. Instead in this regime, the "effective" description comes from the fact that we need to describe the collisions between DM and composite nuclei that have the fundamental Standard Model fields embedded within them. A quark current will, for example, be of the form $\bar{q}\Gamma^a q$, where Γ represents the set of matrices in spinor-space which can be a linear combination of the basis matrices,

$$\Gamma = \{1, \gamma^5, \gamma^\mu, \gamma^\mu \gamma^5, \sigma^{\mu\nu}\}. \quad (2.11)$$

In order to determine how DM interacts with nucleons, we have to embed our quark field current into nucleon field currents. This is done by calculating the hadronic matrix element, $\langle N|\bar{q}\Gamma^q q|N\rangle$, where $|N\rangle$ represents a nucleon, and we have suppressed its momentum and spin dependence. The nucleon bilinears are constrained to respect the same global symmetries \mathcal{C} , \mathcal{P} and \mathcal{T} . For example the $\bar{\psi}\gamma^\mu\psi$ has the same symmetries as $i\bar{\psi}\sigma^{\mu\nu}q_\nu\psi$ where q_ν is the momentum running through the current, which in the direct detection case, is the transferred momentum. The quark current is thus equivalent to the following nucleon-level interaction,

$$\bar{q}\Gamma^q q \rightarrow \langle N|\bar{q}\Gamma^q q|N\rangle = \sum_j F_j^{(q,N)}(q^2)\bar{N}\Gamma^{q,j}N, \quad (2.12)$$

where the sum over j is over the different Lorentz structures that share the same symmetries as Γ^q . For each of these, the form factors $F_j^{(q,N)}(q^2)$ encode the internal structure of the nucleon. Ref [127], provides results for these form factors that are calculated using chiral perturbation theory and nonperturbative results.

Furthermore, the dominant interactions in the recoil may not necessarily result from quark interactions and instead can be due to couplings to gluons. There are certainly severe constraints on DM having any QCD charge, but interactions can arise from higher dimensions. In particular, if DM couples via some new mediator to heavy quarks, loop suppressed diagrams connecting DM to gluons will contribute the most to the cross section due to the relatively tiny distribution of these quarks in the the nucleons. The effective gluon operators are determined once again by the symmetries of the quark current and their scaling by some matching. Results are given in [128, 129] for the matching to these gluon operators.

The partonic form factors need to be included when embedding these operators into the nucleons. This requires different techniques depending on the type of gluon current. The scalar case can be derived using the QCD scale anomaly [130] whereas results for the pseudoscalar require chiral perturbation theory [127].

The embedding of the SM fields into the nucleons relies on the aforementioned separation of SM and DM currents, \mathcal{J}_{SM} and \mathcal{J}_{DM} , this is important because the hadron matrix element is calculated as a local operator expansion. This is more evident in t-channel processes, where the $\bar{q}\Gamma^a q$ vertex is in the diagram. However, the s-channel processes in direct detection arise from $\bar{\chi}\Gamma\bar{q}$ vertices, leading to nonlocal operator, requiring the we calculate $\langle N|\bar{\chi}\Gamma\bar{q}\frac{1}{s-M^2}\bar{\chi}\Gamma q|N\rangle$. The result however can still be calculated using the local operators because $s \sim (m_N + m_\chi)^2 \gg (q^2, \Lambda_{\text{QCD}})$. Therefore, one can make use of Fierz transformations [131, 132] to rewrite the interaction in terms of $\mathcal{J}_{\text{DM}}\mathcal{J}_{\text{SM}}$.

After calculating the hadron matrix elements, one is left with an expression which is in terms of DM and nucleon fields, but still described in the relativistic regime. Instead of trying to represent the fields \bar{N} and N in terms of their non-relativistic counterparts N^+ and N^- , its more straightforward to find the currents that will arise from calculating the relativistic matrix element, and then take the non-relativistic limit. Since nucleons are fermionic, this means we'll always have to take the limit of spinor currents. In the Weyl basis the fermion spinor fields take the form,

$$u(p)^s = \begin{pmatrix} \sqrt{p \cdot \sigma} \xi^s \\ \sqrt{p \cdot \bar{\sigma}} \xi^s \end{pmatrix} \quad \text{and} \quad v(p)^s = \begin{pmatrix} \sqrt{p \cdot \sigma} \eta^s \\ -\sqrt{p \cdot \bar{\sigma}} \eta^s \end{pmatrix} \quad (2.13)$$

where $\sigma^\mu = (1, \vec{\sigma})$ and $\bar{\sigma}^\mu = (1, -\vec{\sigma})$ are the four-vector generalisations of the Pauli matrices. The s superscript runs over the possible spins of the particle which will be summed. The spin operator is defined as follows $\vec{S} = \frac{1}{2}\vec{\sigma}$, ξ and η are the standard solutions the the Dirac equation in the relativistic limit. Spin can also be defined by $\vec{S} = \xi^\dagger \frac{\vec{\sigma}}{2} \xi$. Taking a first order approximation in the non-relativistic limit we get the following,

$$u(p)^s \approx \frac{1}{\sqrt{4M}} \begin{pmatrix} (2M - p \cdot \sigma) \xi^s \\ (2M + p \cdot \sigma) \xi^s \end{pmatrix}, \quad (2.14)$$

where here we have the normalisation $\bar{u}(p)u(p) = 2M$, corresponding to the non relativistic fields having mass dimension 1. When working in the convention where

the fields have mass dimension 3/2, our spinor fields are normalised such that $\bar{u}(p)u(p) = 2M$. From here, one can immediately start to take some results in the form of nucleon fermion bilinears, by defining, $\xi^\dagger \xi \equiv \mathcal{I}_N$. This gives $\bar{u}(p)u(p) = 2m_N \mathcal{I}_N$ and leads to results such as, $\bar{u}(p)i\gamma^5 u(p) = -2i\vec{q} \cdot \vec{S}$.

For bilinears with Lorentz indices, one will find a four-vector or tensor result that will be contracted with the DM current. Some useful identities are

$$\sigma_i \sigma_j = \delta_{ij} 1_2 + i\epsilon_{ijk} \sigma^k \quad \text{and} \quad \epsilon_{ijk} \epsilon_{ijk} = \delta_{ja} \delta_{kb} - \delta_{jb} \delta_{ka}. \quad (2.15)$$

which lead to results such as,

$$\bar{u}(k_2)\gamma^\mu u(k_1) = \left(\begin{array}{c} 2m_N 1_N \\ \vec{K} 1_N - 2i\vec{q} \times \vec{S}_N \end{array} \right). \quad (2.16)$$

In practice, the non-relativistic limits of different bilinear structures can be taken from published results such as [123, 133]. However, there are some cases where the results do not go to sufficiently high terms in q , which we will see with the monopole interaction below.

In the proceeding subsections, we present two characteristic examples: WIMPs and DM with photon couplings.

The WIMP particle

As discussed in Chapter 1 the original inspiration for WIMP DM was precisely the fact that a particle with weak scale interactions can thermally freeze-out, giving the correct abundance. Thus, we will start by considering a weakly interacting fermion that is mediated through the Z boson. In this case, we can integrate out

the mediator

$$\mathcal{L}_{\text{int}} = g_1 \bar{\chi} \gamma^\mu \chi Z'_\mu + \sum_q g_2 \bar{q} \gamma^\mu q Z'_\mu \quad \longrightarrow \quad \mathcal{L}_{\text{int}} = \sum_q \frac{g_1 g_2}{m_Z^2} \bar{\chi} \gamma^\mu \chi \bar{q} \gamma_\mu q, \quad (2.17)$$

giving the $\mathcal{J}_{\text{DM}}^\mu \mathcal{J}_{\text{SM}}^\mu$ structure. The quarks are embedded by evaluating the hadron matrix element (2.12). For $\bar{q} \gamma^\mu q$ there are two terms that contribute [127, 131],

$$\langle N | \bar{q} \gamma^\mu q | N \rangle = F_1^{(q,N)}(q^2) \bar{N} \gamma^\mu N + \frac{i}{2m_N} F_2^{(q,N)}(q^2) \bar{N} \sigma^{\mu\nu} q_\nu N, \quad (2.18)$$

where the two form factors F_1 and F_2 are known as Dirac and Pauli form factors. The Dirac form factor in the zero momentum limit counts the number of valence quarks in the nucleon, for example $F_1^{u,p}(0) = 2$. Therefore, assuming that g_2 is the same for all quarks, the quark level coupling will be related the nucleon coupling by a factor of 3, $g_2^N = 3g_2^q$ and will be the same for both $N = n, p$. The Pauli factor gives some description of how different quarks contribute to the nucleon magnetic moments [50]

$$F_2^{(u,p)}(0) = 1.609, \quad F_2^{(d,p)}(0) = -2.097, \quad F_2^{(s,p)}(0) = -0.064, \quad (2.19)$$

where one can use isospin symmetry to obtain the result for the neutron. Here, assuming g_2 is the same for all quarks, the nucleon coupling is $-0.552g_2^q$ for both proton and neutron.

Evaluating both the $\bar{\chi} \gamma_\mu \chi \bar{N} \gamma^\mu N$ and $\bar{\chi} \gamma_\mu \chi \frac{i}{2m_N} \bar{N} \sigma^{\mu\nu} q_\nu N$ leads to multiple terms, but focusing on the lowest order in q , we get the result,

$$\mathcal{L}_{\text{int}} = \sum_N \frac{g_1 g_2^N}{m_Z^2} \bar{\chi} \gamma_\mu \chi \bar{N} \gamma^\mu N \approx \sum_N \frac{4m_N m_\chi g_1 g_2^N}{m_Z^2} \mathcal{I}_\chi \mathcal{I}_N + \mathcal{O}(q) + \dots \quad (2.20)$$

Comparing this with table 2.1 we see we have only one operator coefficient at the lowest order in q ,

$$c_1^N = \frac{4m_N m_\chi g_1 g_2^N}{m_Z^2}. \quad (2.21)$$

To express this result in the convention of eq. (2.10), we simply divide c_1^N by $4m_N m_\chi$ and multiply by m_v^2 . Notice that in general the expectation $c_1 m_v^2 \approx 1$ may be

substantially affected by nucleon form factors in the matching calculation. In this specific case however the Dirac Form factors are order 1 numbers and do not alter the expectation that $c_1 m_v^2 \approx 1$ for a DM particle interacting via a weak scale interaction.

DM with coupling to photons

DM may also interact via the photon through some loop process [134–139]. In some BSM scenerios, this is the leading contribution. These interactions can be described in terms of an effective Lagrangian. Once more considering a DM fermion, the effective Lagrangian is

$$\mathcal{L}_{\text{int}} = \frac{d}{2} \bar{\chi} i \sigma^{\mu\nu} \gamma^5 \chi F_{\mu\nu} + \frac{\mu}{2} \bar{\chi} \sigma^{\mu\nu} \chi F_{\mu\nu} + b_\chi \bar{\chi} \gamma^\mu \chi \partial^\nu F_{\mu\nu} + \mathcal{A} \bar{\chi} \gamma^\mu \gamma^5 \chi \partial^\nu F_{\mu\nu}, \quad (2.22)$$

where these terms are known as the electric and magnetic dipole moments, the charge radius and the anapole moment interactions respectively. The first two terms have mass dimension 5 while the latter two have mass dimension 6, hence the parameters d and μ have mass dimension -1 while b_χ and \mathcal{A} have mass dimension -2 .

The photon couples to quarks via $e Q_q \bar{q} A_\mu q$. Being massless, the photon cannot be integrated out like the Z-boson was above. Including the photon propagator in the Feynman-'t Hooft gauge [50], the interaction operator becomes

$$F_{\mu\nu} \rightarrow Q_q \left[i \frac{q_\mu}{q^2} \bar{q} \gamma_\nu q - i \frac{q_\nu}{q^2} \bar{q} \gamma_\mu q \right]. \quad (2.23)$$

Noticing that both dipole moments are multiplied by a $\sigma^{\mu\nu}$ factor means we can combine the two terms into one, making use of the fact that $\sigma^{\mu\nu}$ is antisymmetric. The quark fields \bar{q}, q are embedded in the nucleon field to get a nuclear term

$$\sum_N i \frac{q_\mu}{q^2} \left[Q_N \bar{N} \gamma_\nu N + \frac{i}{2m_N} a_N \bar{N} \sigma_{\mu\nu} q^\nu N \right]. \quad (2.24)$$

Summing over the Dirac and Pauli form factor contributions gives the Q_N and a_N factors. Q_N is just the electric charge of the nucleon, while a_N are the anomalous magnetic moments of the nucleons, $a_p = 1.793$ and $a_n = -1.913$.

For the two final terms in Eq (2.22), the treatment of the photon propagator can be skipped by using its equation of motion,

$$\partial^\nu F_{\mu\nu} = -e \sum_q Q_q \bar{q} \gamma_\mu q. \quad (2.25)$$

Hence, we have a very similar structure when embedding quarks into the nucleons here. If one takes the first Gordon identity from,

$$\begin{aligned} \bar{N} \gamma^\mu N &= \frac{1}{2m_N} \bar{N} (K^\mu + i\sigma^{\mu\nu} q_\nu) N \\ \bar{N} i\sigma^{\mu\nu} \gamma^5 q_\mu N &= \bar{N} K^\mu \gamma^5 N. \end{aligned}$$

the coefficient of the $\bar{N} i\sigma^{\mu\nu} q_\nu N$ term is now $Q_N + a_N = \tilde{\mu}_N$, which is known as the nucleon magnetic moment [140], in units of the nuclear magneton $\mu_N = -e/(2m_N)$. This value is also more commonly expressed in terms of the g-factor, $g = 2\tilde{\mu}_N$.

Taking the non-relativistic limit explicitly as outlined in the previous section leaves us with the following results,

$$\frac{d}{2} \bar{\chi} i\sigma^{\mu\nu} \gamma^5 \chi F_{\mu\nu} \longrightarrow d Q_N e \frac{1}{q^2} 8m_\chi m_N^2 \mathcal{O}_{11}, \quad (2.26)$$

$$\frac{\mu}{2} \bar{\chi} \sigma^{\mu\nu} \chi F_{\mu\nu} \longrightarrow 4\mu e m_\chi m_N \left[\frac{Q_N}{4m_\chi} \mathcal{O}_1 + Q_N m_N \frac{\mathcal{O}_5}{q^2} + \frac{g_N}{2m_N} \left(\mathcal{O}_4 - \frac{m_N^2 \mathcal{O}_6}{q^2} \right) \right], \quad (2.27)$$

$$b_\chi \bar{\chi} \gamma^\mu \chi \partial^\nu F_{\mu\nu} \longrightarrow 4m_\chi m_N b_\chi e \sum_N Q_N \mathcal{O}_1, \quad (2.28)$$

$$\mathcal{A} \bar{\chi} \gamma^\mu \gamma^5 \chi \partial^\nu F_{\mu\nu} \longrightarrow 4m_\chi m_N e \mathcal{A} \sum_N (2Q_N \mathcal{O}_8 - g_N \mathcal{O}_9). \quad (2.29)$$

As mentioned above, care is required when using published results of the non-relativistic limit such as those in Refs. [123, 133]. A specific example relevant to the

models considered here is the magnetic dipole interaction, when using Ref. [133] to calculate the response, the matching gives 0, only if you go to the next order in momentum do you get the required result.

Typically, the largest of these interactions is the charge radius, followed by the dipole moments.

2.3 Current Experimental landscape

In Chapter 1 we discussed the state-of-the-art experiments in direct detection. Now that we have reviewed how direct detection works, we will present the current experimental situation. Typically, experiments present their results in the spin-independent or spin-dependent plane, which is easily related to the NREFT basis. The spin-independent cross section, σ^{SI} , is the zero-momentum cross section from the \mathcal{O}_1 interaction, and is related by the expression

$$\sigma_{\chi N}^{SI} = \frac{(c_1^N)^2}{16\pi (m_N + m_\chi)^2} = \frac{\mu_{\chi N}^2}{\pi m_v^4} (\tilde{c}_1^N)^2 \quad (2.30)$$

where the coefficient c and \tilde{c} are dimensionless, but \tilde{c} is result of the convention that normalises dimension -2 coefficients with factors of the Higgs vev, m_v . The current exclusion limits are shown in Figure 2.3. One can see the mass range that is being probed by these experiments is vast. Above ~ 10 GeV the dual phase liquid xenon experiments PandaX [104] and Xenon-1T [102] have the most stringent bounds. Below this is where lighter target experiments such as CRESST [107], Darkside-50 [115], NEWS-G [117] and CDMS [116] are able to push to lower thresholds and provide competitive constraints on lower masses, the lowest of which is NEWS-G at 0.5 GeV.

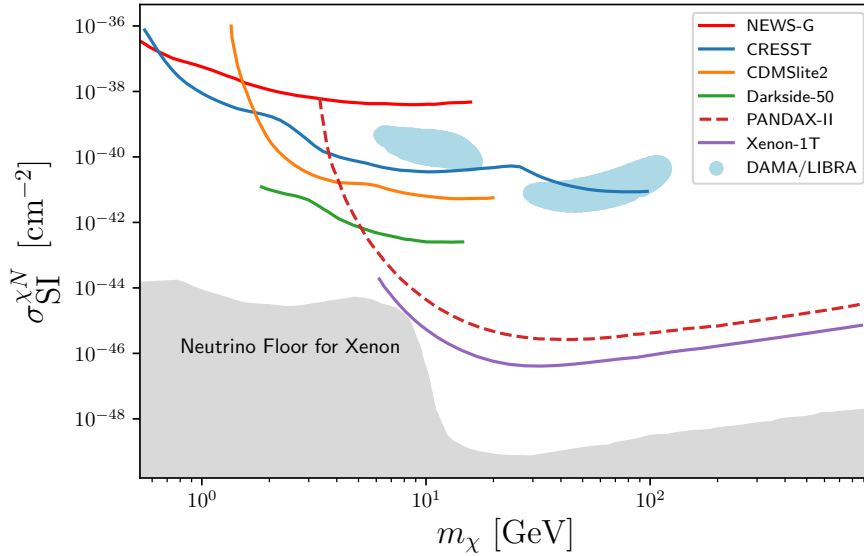


Figure 2.3: The current exclusion limits of spin-independent (\mathcal{O}_1) interactions between DM (χ) and nucleons (N) for an array of experiments. The exclusion limits presented here are to the same confidence as quoted in the relevant papers. Refs. [102, 104, 107, 115, 116] provide 90% confidence for the upper limit exclusions for PandaX, Xenon1T, CRESST, Darkside-50, NEWS-G and CDMS respectively. For DAMA, the 3σ (90% C.L.) reconstruction regions are shown [141].

Notice the DAMA/LIBRA best fit region is included here. The DAMA [142] signal has persisted despite more sensitive experiments seemingly excluding in. Confusing experimental situations like this is precisely where the large freedom from the NREFT could come in useful. Studies have shown that its becoming increasingly difficult to reconcile the situation, resorting to highly tuned models that favor specifically the Sodium or Iodine target of DAMA/LIBRA [143, 144]. Experiments such as ANAIS [145] and COSINE [146] are currently taking data with the same target material in an effort to verify the modulation signal, and have already started to rule out some parts of the DAMA region.

Also included is the neutrino floor, which represents the experimental sensitivity where the coherent neutrino background is expected to be detected in experiments [147]. The expected neutrino fluxes from the sun and the atmosphere can be found in Refs. [148–152]. We see the Xenon-1T is very close to reaching it, thus

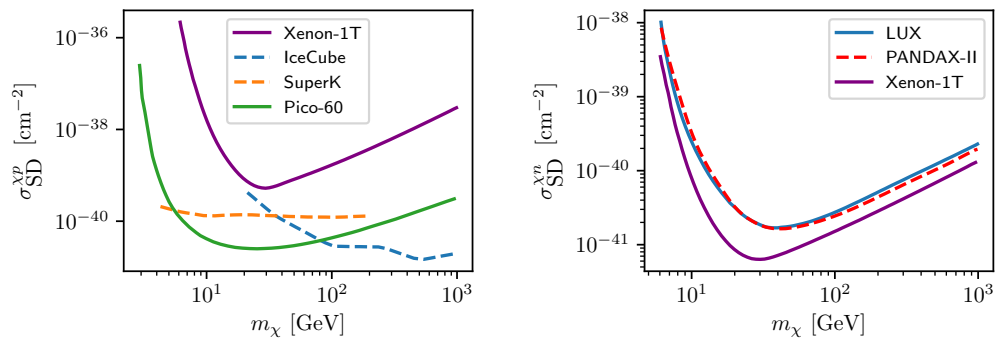


Figure 2.4: (Left) The best constraints on proton-DM spin dependent interaction, including direct detection and annihilation constraints coming from SuperK and IceCube. (Right) Constraints on the neutron-DM spin dependent interaction.

the floor that is shown in Figure 2.3 is for a xenon target [147]. As direct detection experiments improve, separating the neutrino floor from possible DM signals will become increasingly important. One way to do this is by exploiting the seasonal fluctuations of incident DM speeds in annual modulation [153], the other is by developing directional detection experiments [122], which would give important information on the origin of incident particles.

For the spin-dependent cross section the zero-momentum cross section stems from the \mathcal{O}_4 response, and is related to the coefficients by,

$$\sigma_{\chi N}^{SD} = \frac{3(c_4^N)^2}{256\pi(m_N + m_\chi)^2} = \frac{3\mu_N^2(\tilde{c}_4^N)^2}{16\pi m_v^4}. \quad (2.31)$$

Figure 2.4 provides us with the current exclusion limits for the spin-dependent interactions with protons and neutrons. Notice that for the σ_{SD}^{xp} , the leading experiment is PICO-60 [154], due to its high number of unpaired protons. Also, in this plane, the neutrino detectors Super-Kamiokande [155] and IceCube [156] are able to constraint DM interactions via capture in the sun. The σ_{SD}^{xn} interaction is probed well by the neutron rich xenon targets as seen in the right panel in Figure 2.4.

In this chapter, the details of the two dominant conventions for presenting the

operator coefficients have been kept. In proceeding chapters, we adopt the whereby c has mass dimension -2 and is multiplied by factors of m_ν .

Chapter 3

Determining Dark Matter

Properties from Direct Detection

The previous chapter reviewed the family of NREFT operators arising from elastic scattering. The nuclear response to these operators can vary differently, i.e. q -independent responses increase at $q \rightarrow 0$, whereas q -dependent interactions vanish in the same limit. Section 2.2 showed how the properties of DM and the UV model can determine which NREFT operators are at play in direct detection and how they relate. Of course, we are interested in working backwards, from experimental results to statements about the nature of DM.

Earlier work in the literature explored how DM signatures produce specific spectral shapes in the nuclear recoil spectrum, allowing one to reconstruct DM properties such as mass and cross section [157,158]. With the inclusion of the full NREFT basis, experimental information about the spectral shape allows one to distinguish non-standard momentum dependence [159]. Furthermore, this information is crucially important for background discrimination, and properly interpreting null results [160].

Additionally, the recoil spectrum is dependent on astrophysical parameters that describe our Milky Way halo [161], as well as the nuclear form factors [162]. Such complications make it more difficult to extract the particle physics information. It has been shown that using different experimental targets [163–165] is crucial for disentangling the particle physics. Combining the results from multiple targets and techniques strongly constrains theoretical models in the absence of a detection and allows for determination of the underlying physics of the interaction once a signal is seen [166–168].

When trying to determine these parameters, one has to account for sources of error under some statistical framework. Of course, when incorporating the details of direct detection experiments the reconstruction of DM parameters is subject to these statistical limitations [169]. It is important to understand these limitations when attempting to identify the right theory of DM [140, 170–173]. This is not only to ready ourselves for future experimental results, but also to perhaps identify blind-spots in the current strategy.

Adopting a completely agnostic approach, the reconstruction of DM parameters is extremely challenging in the multi-dimensional EFT parameter space. It is clear that the next generation of experiments, with their multiple targets, will be a good start in the effort to probe the general EFT parameter space [174, 175].

In order to frame the work presented in the proceeding chapters we will present some basic statistical tools in Section 3.1. This leads to a discussion on nuisance parameters, which for direct detection usually come from astrophysics which is described in Section 3.2. The final section of this chapter briefly reviews various different strategies that have been explored in the literature and will be returned to in the rest of this thesis.

3.1 Statistical tools

As described in Eq.(2.1), the recoil spectrum can be collected via a series of energy bins. Modeling each bin as a independent measurement leads to the Poisson distribution as the relevant description of probability,

$$\mathcal{P}(N_{\text{obs}}|N_{\text{th}}) = \frac{N_{\text{th}}^{N_{\text{obs}}} e^{-N_{\text{th}}}}{N_{\text{obs}}!}, \quad (3.1)$$

this gives the probability that one observes N_{obs} events given that one expects $N_{\text{th}} = N_{\text{DM}}(\Theta) + N_{\text{b}}$ for a set of parameters $\Theta = \{x, y, z, \dots\}$. Here N_{DM} is just the DM signal predicted for the parameters and N_{b} is the expected background events. The value of $N(\Theta)$ also depends on the specific model \mathcal{M}_i , where the subscript differentiates between models. Therefore, we can write the probability as $\mathcal{P}(N_{\text{obs}}|N_{\text{b}}, \Theta, \mathcal{M}_i)$. The likelihood of an experiment with multiple bins is simply the product of the Poisson distribution evaluated at each bin, i.e.

$$\text{Likelihood} = \prod_k \mathcal{P}(N_{\text{obs},k}|N_{\text{b}}, \Theta, \mathcal{M}_i). \quad (3.2)$$

Following a frequentist approach, this probability is interpreted as the frequency of the outcome of a repeatable experiment [176]. Therefore a 90% C.L. is to be interpreted as the point when 90% of experiments would have detected more than N_{obs} events given a theoretical expectation N_{th} ,

$$\sum_{m=N_{\text{obs}}+1}^{\infty} \mathcal{P}(m|N_{\text{b}}, \Theta, \mathcal{M}_i) = 0.9 \quad \rightarrow \quad \sum_{m=0}^{N_{\text{obs}}} \mathcal{P}(m|N_{\text{b}}, \Theta, \mathcal{M}_i) = 0.1. \quad (3.3)$$

For example, taking a background free experiment that observes no events ($N_{\text{b}} = N_{\text{obs}} = 0$) results in $N_{\text{DM}}^{90\%} = 2.303$. This procedure is sufficient to get an estimate for the projected sensitivity of future experiments when the expected background is separable from signal. Even after an experiment has published its results, this method can be used effectively. For example the recent XENON1T result observed $N_{\text{obs}} = 2$ events where $N_{\text{b}} = 1.62$ background events were expected from the collaboration's models [102]. Using the Poisson distribution and solving Eq.(3.3) leads to $N_{\text{DM}}^{90\%} =$

3.68. Figure 3.1 shows that this method gives fairly close agreement to the full experimental analysis as reported in Refs. [102, 177, 178]. One can see the simple Poissonian method is insufficient to match the experimental results for masses below ~ 50 GeV. This can be explained by the fact that the observed events N_{obs} are both in the high recoil region, above $E_R \sim 25$ keV. Since DM particle with masses less than 50 GeV and interacting via \mathcal{O}_1 , is expected to provoke a much greater number of recoils at lower energy, this kind of signal is very unlikely, so N_{obs} can be dismissed as background with greater confidence.

Therefore, to improve this estimate, one needs to include some information about the signal features, the Test Statistic (TS) defined by,

$$\text{TS}(\lambda) = -2 \log \left(\frac{\text{Likelihood}(N_{\text{obs}}|N_b, \Theta, \mathcal{M}_i)}{\text{Likelihood}(N_{\text{obs}}|N_b)} \right), \quad (3.4)$$

The $\text{TS}(\lambda)$ is approximately the same as a χ^2 distribution with the same number of degrees of freedom as parameters. Substituting in the Poisson distribution,

$$\text{TS}(\lambda) = \sum_k \left[-2N_{\text{obs},k} \log \left(\frac{N_{\text{DM},k} + N_{b,k}}{N_{b,k}} \right) + 2N_{\text{DM},k} \right]. \quad (3.5)$$

Note that this is not well defined at $N_{b,k} = 0$ or $N_k = 0$. To find the 90% C.L. bounds, one just looks up the corresponding χ^2 value [179] and solves for N_{DM} . This method is best suited when the experimental backgrounds are known, which is not always the case. In the case of an unknown background, one can estimate $\text{Likelihood}(N_{\text{obs}}|N_b)$ by maximising $\text{Likelihood}(N_{\text{obs}}|N_b, \Theta, \mathcal{M}_i)$ and using the result.

In the event of positive DM signal, regions of parameter space that maximise the likelihood give an indication of the parameter values, assuming model \mathcal{M}_i . This approach is particularly well suited for constructing confidence intervals to determine the true value of parameters. The intervals are defined via Wilks' theorem [176, 179, 180], making use of the cumulative distribution function $F_{\chi^2_1}$, where for the

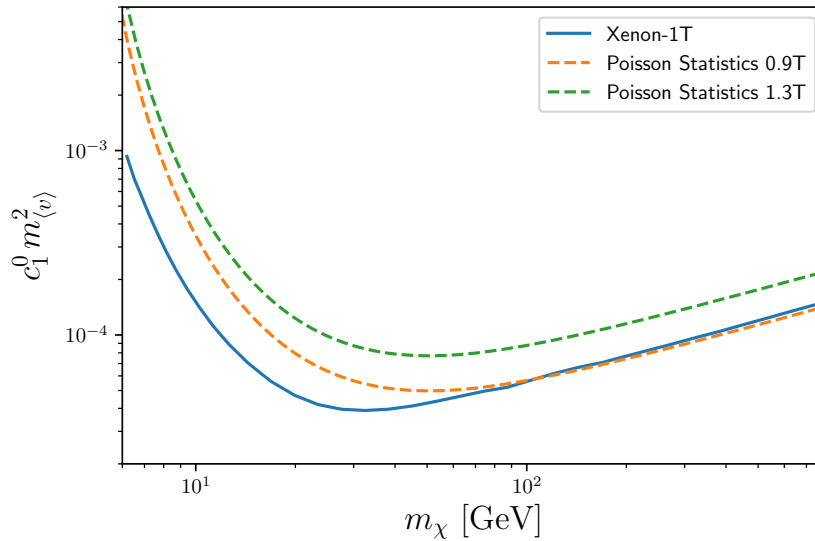


Figure 3.1: Exclusion limits published in 2018 for the XENON1T experiment [102]. We see that the naive Poissonian method is effective at replicated published experimental limits in the mass region above ~ 100 GeV.

one-dimensional interval we have,

$$-2 \log \frac{\text{Likelihood}(x)}{\max(\text{Likelihood}(x, y, z, \dots))} \leq F_{\chi_1^2}^{-1}(1 - \alpha), \quad (3.6)$$

where we have defined $\text{Likelihood}(x) = \max_{y, z, \dots}(\text{Likelihood}(x, y, z, \dots))$ and α is a number that one chooses in correspondence with their desired confidence level [179]. Furthermore, when comparing models in the frequentist picture, it is usually sufficient to compare likelihood values across different models via the ratio test which replaces the fraction in Eq.(3.4) with

$$R = \frac{\max(\text{Likelihood}(\mathcal{M}_1))}{\max(\text{Likelihood}(\mathcal{M}_2))}. \quad (3.7)$$

The Bayesian framework provides its own analogue to these intervals, known as the probability density function (p.d.f.) which describe the state of knowledge of the true value of the parameter, and for a set of continuous variables Θ is the same as the posterior probability,

$$P(\Theta|N_{\text{obs}}, \mathcal{M}) = \frac{\text{Likelihood}(N_{\text{obs}}|\Theta, \mathcal{M})p(\Theta, \mathcal{M})}{\int d\Theta \text{Likelihood}(N_{\text{obs}}|\Theta, \mathcal{M}) p(\Theta, \mathcal{M})}, \quad (3.8)$$

where $p(\Theta, \mathcal{M})$ is the prior, which is taken to be flat when there is no previous data taken into account. The integral in the denominator is known as the evidence $\varepsilon(N_{\text{obs}}|\mathcal{M}_i)$ which can be compared with other models being considered to find the probability of the model,

$$Pr(\mathcal{M}_i) = \frac{\varepsilon(N_{\text{obs}}|\mathcal{M}_i)}{\sum_j \varepsilon(N_{\text{obs}}|\mathcal{M}_j)}. \quad (3.9)$$

Bayesian methods require an integration and therefore are more computationally expensive, however when a new data set is released, one could incorporate a previous study by using the posterior probability $P(\Theta|N_{\text{obs}}, \mathcal{M}_i)$ as the prior, whereas in the frequentist framework, one is required to conduct the analysis over all previous datasets again.

Often when performing an analysis, one may use several parameters that are not known perfectly and are not being probed particularly with the experiment at hand. These are referred to as nuisance parameters and can be marginalised over to obtain the marginalised posterior

$$P(\Theta|N_{\text{obs}}, \mathcal{M}) = \int d\nu P(N_{\text{obs}}|\Theta, \nu, \mathcal{M})\mathcal{P}(\nu)\mathcal{P}(\Theta, \mathcal{M}), \quad (3.10)$$

where ν is some parameter that has a prior taken from a different set of experiments.

3.2 Astrophysical inputs and their uncertainties

Commonly, astrophysical parameters are considered as nuisance parameters in the direct detection calculations. Unlike many particle physics experiments, the incident particle beam, the DM flux in this case, is not under laboratory control. The standard practice has been to adopt an idealised model where the halo is a spherical, isotropic and smooth distribution, known as the Standard Halo Model (SHM) [181, 182]. Which

takes the form,

$$\mathcal{F}_{\text{SHM}} = \frac{\rho_0}{2\pi\sigma} \exp\left(\frac{\Psi - \frac{1}{2}v^2}{\sigma^2}\right), \quad (3.11)$$

where ρ_0 and σ are constants and $\Psi = -\Phi + \Phi_0$ is the potential defined relative to the potential at a particular point Φ_0 . The density and velocity distributions are [183],

$$\rho(x) \equiv \int d^3v \mathcal{F}(x, v) \quad \text{and} \quad f(v) \equiv \int d^3x \mathcal{F}(x, v), \quad (3.12)$$

from this definition, one can see that,

$$f(v) \propto \exp\left(-\frac{v^2}{2\sigma^2}\right) \quad (3.13)$$

which is usually considered unrealistic because the finite mass of the galaxy will have some escape velocity, v_{esc} such that, above it, $f(v)$ is zero, for $f(v)$ in Eq.(3.13), this is not the case. Practically, this is often implemented by truncating $f(v)$ at v_{esc} , creating now an unrealistic discontinuity. One can validate the use of this model to obtain results that agree with rotation curves, namely that $\rho \propto r^{-2}$, by using the Poisson's equation.

Parameter inputs for the SHM model are precisely the type of nuisance parameters that enter in the statistical analysis. In particular the local DM density, ρ_χ , the galactic escape velocity v_{esc} and the central velocity v_0 . Over the years, speculative halos with more extravagant features have been considered, such triaxiality [184], anisotropies [185–187] and substructures such as streams [188–190].

In Chapter 4 we make use of a generalised DM halo parameterisation, defined by the following velocity distribution function

$$f(v) = \left[e^{-v^2/kv_0^2} - e^{-v_{\text{esc}}^2/kv_0^2} \right]^k \Theta(v_{\text{esc}} - v), \quad (3.14)$$

which recovers the SHM distribution with a smooth transition to zero at $v \rightarrow v_{\text{esc}}$ when $k = 1$. Since this distribution is still isotropic, $d^3v f(v) = 4\pi v^2 f(v)$, one can

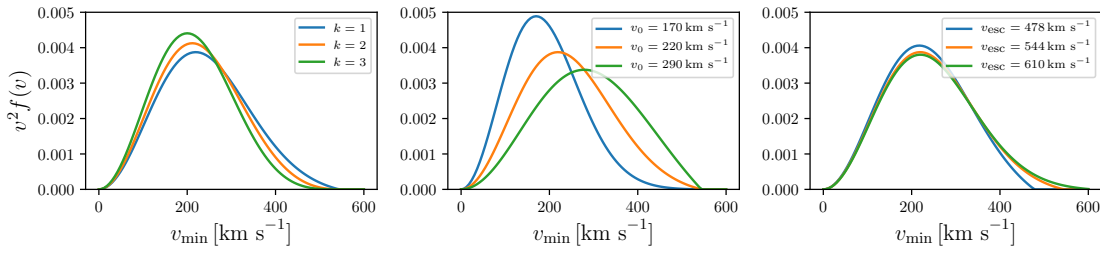


Figure 3.2: The variation of the halo distribution function Eq.(3.15) due to the nuisance parameters k , v_0 and v_{esc} . When panel is not varying a particular parameter its SHM value is taken, i.e. $k = 1$, $v_0 = 220 \text{ km s}^{-1}$ and $v_{\text{esc}} = 544 \text{ km s}^{-1}$

produce the normalised speed distribution,

$$F(v) = N_k^{-1} v^2 \left[e^{-v^2/kv_0^2} - e^{-v_{\text{esc}}^2/kv_0^2} \right]^k \Theta(v_{\text{esc}} - v), \quad (3.15)$$

where $N_k = v_0^3 e^{-y_e^2} \int_0^{y_e} dy y^2 (e^{-(y^2 - y_e^2)/k} - 1)^k$ and $y_e = v_{\text{esc}}/v_0$. Figure 3.2 shows how varying these parameters affects the high-velocity tail [185, 191–194]. We have considered variations in the halo parameters as $v_{\text{esc}} \in [478, 610] \text{ km s}^{-1}$, $v_0 \in [170, 290] \text{ km s}^{-1}$, and $k \in [0.5, 3.5]$, which are included in our scan as nuisance parameters.

When one calculates the distribution of DM velocity as seen by an Earth observer, one has to include the velocity of the Earth with respect to the Sun [195] and the circular and peculiar velocity of the Sun with respect to the Local Standard of rest. In this thesis we use the values as given in Ref. [196], i.e. $v_{\text{circ}} \approx (0, 230, 0) \text{ km s}^{-1}$ and $v_{\text{pec}} \approx (11.10, 12.24, 7.25) \text{ km s}^{-1}$. The halo integrals that contribute to velocity independent particle interactions, $\eta(v_{\text{min}})$ are shown in Figure 3.3. We see that the variations in parameters k , v_0 and v_{esc} are largest in the tail of the distribution, which is consistent with Figure 3.2. The logarithmic plot in Figure 3.3 really shows how the variation can lead a differences of orders of magnitude. However, since these differences are in the tail, these halo parameters effect parameter reconstructions for lower mass DM models (below 30 GeV). Although, as we show in Chapter 5, by extending the analysis region of experiments to include the high velocity end of

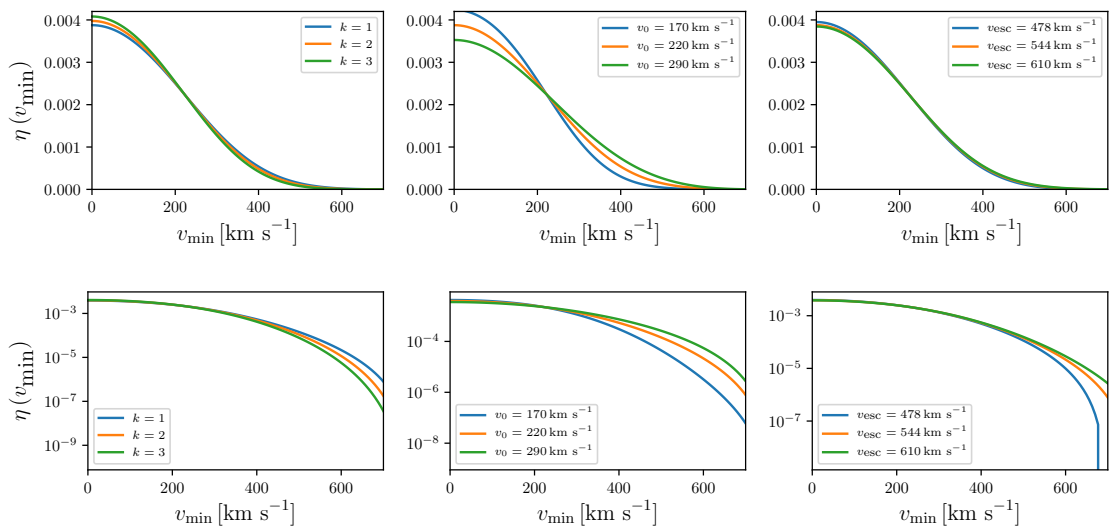


Figure 3.3: The same as Figure 3.2 but now for the halo integral $\eta(v)$. The Earth and Sun’s motions are incorporated for these evaluations. We have also shown the plots on a logarithmic because the differences in the tail of the distribution are important for the recoil spectra, especially for low DM masses.

the distribution, astrophysical uncertainties effect the particle physics interpretation even for heavier DM models.

The local DM density is also subject to observational uncertainties, and we have considered here a range $\rho_0 \in [0.2, 0.6] \text{ GeV cm}^{-3}$ [197–200]. These ranges are consistent (although broader) than those obtained in recent analysis of N-body simulations that include the effect of baryons Ref. [196, 201].

The early motivations for deviation came from both N-body simulations and the desire to understand how these astrophysical uncertainties could possibly affect direct detection. Simulations that only included collisionless cold dark matter provided evidence for departures to the standard velocity distributions [202–205], there was even evidence for anisotropic DM halos [191, 193, 206–209]. More recent simulations that include baryonic effects however, show that a SHM description seems more appropriate [196, 201]. Interestingly, recent surveys have been able to shed light on the sub-structure within the halo and are thus able to make some clear measurements of the local DM. In fact, recent Gaia [210] data presents the interesting possibility of

a stream which is impacting the Milky Way "head-on" [211]. Which could potentially see some real effect in the recoil signal for dark matter models [212].

The effects of the dark matter halo have been well explored in the literature, the key features being that any uncertainty in ρ_χ just scales with the strength of coupling whereas the velocity distribution effects primarily mass reconstruction for masses of the target $m_\chi \sim m_T$ or lower. As we will see in Chapter 5, the tail could also be important for relatively low mass DM particles, provided direct detection experiments can extend the signal region to probe it.

3.3 Analysis Strategies

Multiple strategies can be employed to let data drive the determination of particle nature of DM in an agnostic way. Here we will describe some methods put forward in the literature [168, 171, 213–216].

Perhaps the most agnostic strategy is to open up the analysis to all operator coefficients shown in Table 2.1, allowing for differences over neutron and proton couplings. This is, of course more computationally expensive, and for parameter scans leads to the computer science problem known as the curse of dimensionality [217], which refers to the fact that as you move to higher and higher dimensions, a larger proportion of the volume is in the edges. Making the situation more difficult, the number of direct detection experiments is small, which in general is insufficient to break many degeneracies. Highly degenerate parameter spaces makes high dimensional parameter scans less feasible and desirable.

Initial approaches to deal with the NREFT basis avoided this problem by assuming

that any direct detection signal will be dominated by only one operator [218, 219]. For exclusion limits, this approach is largely appropriate, with the important caveat that some models allow for interference effects that produce cancellations [127]. Furthermore, as seen in section 2.2, a dark matter model often leads to multiple responses in the NREFT basis. Although it is true that in many cases \mathcal{O}_1 is the dominant interaction by virtue of the A^2 enhancement, this assumes that coefficients are similar in size. When it comes to reconstructing parameters, including an interplay of responses would be necessary to effectively determine the dark matter parameters [127].

Another approach is to take specific UV Lagrangian terms allowing the couplings to be free but then track those relations to the corresponding EFT basis [171, 214]. This neglects the possibility of having multiple new terms in the Lagrangian which could come with different couplings. Pursuing this kind of analysis requires a parameter fit to each model you are considering and then comparing their fits in a statistically significant way. Ultimately, $Pr(\mathcal{M}_i)$ depends on the model space one is considering, therefore its necessary to include a comprehensive set.

One strategy we propose, attempts to incorporate aspects of the aforementioned frameworks in an effort to be as agnostic as reasonably possible. Using Simplified Models [98] introduced in Chapter 1 as a starting point, one can determine which NREFT operators will be non-zero, leading to different operator sets for each model, we can then allow the NREFT coefficients to be free parameters.

In Chapter 4 we consider a set of simplified DM models, in which a DM particle and a new mediator are added to the SM Lagrangian. The EFT operators for direct detection can be recovered in the non-relativistic limit [220]. These models will be labeled according to the nature of the DM and mediator as follows: SS (scalar DM with scalar or pseudoscalar mediator), SV (scalar DM with vector mediator), FS

(fermion DM with scalar or pseudoscalar mediator), FV (fermion DM with vector mediator).

The interaction Lagrangians for such models are [221],

$$\mathcal{L}_{SS} = -g_1 m_S S^\dagger S \phi - \frac{g_2}{2} S^\dagger S \phi^2 - h_1 \bar{q} q \phi - i h_2 \bar{q} \gamma^5 q \phi;$$

$$\mathcal{L}_{SV} = -\frac{g_3}{2} S^\dagger S V_\mu V^\mu - i g_4 (S^\dagger \partial_\mu S - \partial_\mu S^\dagger S) V^\mu - h_3 \bar{q} \gamma_\mu q V^\mu - h_4 \bar{q} \gamma_\mu \gamma^5 q V^\mu;$$

$$\mathcal{L}_{FS} = -\lambda_1 \bar{\chi} \chi \phi - i \lambda_2 \bar{\chi} \gamma^5 \chi \phi - h_1 \bar{q} q \phi - i h_2 \bar{q} \gamma^5 q \phi;$$

$$\mathcal{L}_{FV} = -\lambda_3 \bar{\chi} \gamma^\mu \chi V_\mu - \lambda_4 \bar{\chi} \gamma^\mu \gamma^5 \chi V_\mu - h_3 \bar{q} \gamma_\mu q V^\mu - h_4 \bar{q} \gamma_\mu \gamma^5 q V^\mu;$$

fields S and χ are for dark matter scalars or fermions respectively and ϕ and V are for scalar and vector mediators. Notice with a scalar mediator, a different hadron matrix element needs to be calculated, $\langle N | m_q \bar{q} q | N \rangle$ and $\langle N | m_q \bar{q} i \gamma^5 q | N \rangle$, leading to different values when relating couplings from (3.16) to C^p and C^n , details of which are contained in Refs. [127, 220].

With these models we assume universal quark couplings, i.e. $h_1 = h_1^u = h_1^d$. This is done to comply with MFV introduced in Chapter 1. This assumption also reduces the dimensions of the analysis. In the scalar mediating case, the often considered isospin conserving case $C^p = C^n$, is no longer the true. By following Refs. [127, 220] the results $h_1^n = 0.96 h_1^p$ and $h_2^n = 0.25 h_2^p$ can be obtained.

The leading contributions to the DM-nucleus scattering rate for each simplified DM model can be calculated using the machinery outlined in chapter 2 to get the matching,

$$\mathcal{L}_{SS}^{\text{NR}} = \frac{h_1^N g_1}{m_\phi^2} \mathcal{O}_1 + \frac{h_2^N g_1}{m_\phi^2} \mathcal{O}_{10}; \quad (3.16)$$

$$\mathcal{L}_{SV}^{\text{NR}} = \frac{-2h_3^N g_4}{m_V^2} \mathcal{O}_1 + \frac{4h_4^N g_4}{m_V^2} \mathcal{O}_7; \quad (3.17)$$

$$\mathcal{L}_{FS}^{\text{NR}} = \frac{h_1^N \lambda_1}{m_\phi^2} \mathcal{O}_1 + \frac{h_2^N \lambda_2 m_N}{m_\phi^2 m_\chi} \mathcal{O}_6 + \frac{h_2^N \lambda_1}{m_\phi^2} \mathcal{O}_{10} - \frac{h_1^N \lambda_2}{m_\phi^2} \mathcal{O}_{11}; \quad (3.18)$$

$$\mathcal{L}_{FV}^{\text{NR}} = -\frac{h_3^N \lambda_3}{m_V^2} \mathcal{O}_1 + \frac{4h_4^N \lambda_4}{m_V^2} \mathcal{O}_4 + \frac{2h_4^N \lambda_3}{m_V^2} \mathcal{O}_7 - \frac{h_3^N \lambda_4}{m_V^2} \mathcal{O}_8 - 2 \left(\frac{h_4^N \lambda_3}{m_V^2} \frac{m_N}{m_\chi} + \frac{h_3^N \lambda_4}{m_V^2} \right) \mathcal{O}_9; \quad (3.19)$$

which are consistent with Refs. [216, 220] giving the subset of NREFT responses for each model. Notice that for the (FV) model, we have 5 different operator responses coming from 4 independent couplings to the mediator, this redundancy is expressed by $c_9^N = c_8^N - c_7^N (m_N/m_\chi)$. By inspecting Table 2.1, notice that, \mathcal{O}_5 , \mathcal{O}_6 , \mathcal{O}_9 , \mathcal{O}_{10} and \mathcal{O}_{11} have a non-trivial momentum dependence.

Notice that the operators arising from this set of simplified models is not complete. If we broadened our model space to other simplified models then other operator responses would come into play. For example, a spin-1 DM candidate, mediated by a different spin-1 particle gives rise to \mathcal{O}_5 and \mathcal{O}_{14} [220, 222], whereas spin-1 DM mediated by a spin-1/2 particle [220] gives rise to \mathcal{O}_{12} . The operators such as \mathcal{O}_3 , \mathcal{O}_{13} and \mathcal{O}_{15} are not known to come at first order from any simplified model.

This framework along with considering non-standard halos introduces a non-negligible computational expense. In the next chapter we will outline a novel approach that we have developed to accurately simulate direct detection responses, including possible cancellations and variations in the halo model in a computationally cheap way.

Chapter 4

RAPIDD: Reconstruction

Algorithm of Parameters In Direct Detection

In this chapter we introduce a novel method for simulating the direct detection experiments. It was developed in order to increase the the feasibility of performing higher dimensional analyses, outlined in Chapter 3. We saw in Eq.(2.1) that in order to calculate the expected number of counts N_k in the k^{th} energy bin, one is required to perform two integrations. Additional detector effects can be included such as energy resolution, $Res(E'_R, E_R)$ which is generally incorporated as a Gaussian smearing, and energy-dependent efficiency, $\varepsilon(E_R)$.

As stated in Chapter 3 calculating Eq.(2.1) in a multidimensional parameter space can be very costly. In order to speed up this process, we have developed RAPIDD, a surrogate model that allows a fast and accurate determination of the expected DM spectrum in direct detection experiments. In particular, we have used the

PROFESSOR tool [223] to parameterise the experimental response in terms of simple polynomial functions. The polynomial fits are obtained for each individual experiment via a training process, which employs the exact calculation and the specific details of each experiment. After this (expensive) offline phase, the resulting surrogate model is considerably faster than the exact calculation, especially when the dimensionality of the parameter space is large. Thus, it is ideal to explore the general EFT parameter space, to investigate the complementarity of different targets, or to use in scans that require a large number of evaluations. In this article we validate RAPIDD, and we use it to test the identification of simplified DM models using mock direct detection data from upcoming experiments.

This chapter is organised as follows. In Section 4.1, we explain how the surrogate model RAPIDD is built. We comment on possible limitations and explain how these are dealt with in our analysis. In Section 4.2 we test RAPIDD in some simple scenarios, based on one and two effective operators to describe the DM-nucleus scattering cross section, and also including astrophysical uncertainties. To illustrate our method, in Section 4.3, we apply it to study the reconstruction of parameters to the simplified model approach described in chapter 3, involving up to four different operators, employing three different experimental targets. Finally, our conclusions are presented in Section 4.4.

4.1 Parametrization of the DM detection rate

In this section, we explain the construction of a surrogate model to compute the expected number of DM events in direct detection experiments. Our goal is to speed up the computation without losing precision, then to adapt it to explore multi-dimensional parameter spaces and large scans. To this aim, we have developed

RAPIDD (Reconstruction Algorithm of Parameters In Direct Detection), a Python code based on the PROFESSOR tool (used extensively in particle collider analyses).

The idea of replacing the expensive part of a calculation with an approximate model is certainly not new. In fact a very similar approach taken in this work has been successfully applied in the field of collider physics. Where parameters of Monte-Carlo programs were optimised using numerical χ^2 minimisation [224] or constrain to effective field theory operators in BSM physics scenarios [225–227].

The objective function of our optimization problem is a binned likelihood, constructed from a signal prediction and data (we will use mock data to simulate hypothetical future results) as defined in Eq (3.2) over k bins. We assume that each experimental dataset follows an independent Poissonian distribution, so the full likelihood function is equivalent to the product of the likelihoods for each experiment $\prod_a \text{Likelihood}(N_{\text{obs},a} | N_b, \Theta, \mathcal{M}_i)$.

Traditionally, such analyses are conducted by interfacing a likelihood evaluator with the signal generating code directly. Modern statistical tools are very efficient and especially the introduction of nested sampling prevents wasting CPU cycles on points of the parameter space where the likelihood is low. However, this approach relies on exactly evaluating the signal prediction at every iteration which in turn means that the run-time of the likelihood evaluation is dominated by the run-time of the signal prediction of eq.(2.1). This effectively limits its applicability to low-dimensional parameter spaces or more general to cases where the statistical analysis does not become prohibitively expensive.

In this work we replace each exact N_k^g with an ordinary polynomial that has been trained on a sample of N_k^g at various points of the model parameter space, Θ , using PROFESSOR. In that sense, our surrogate model is simply a collection of polynomials

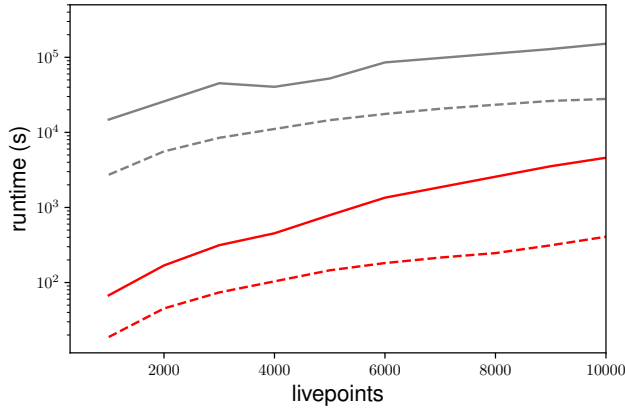


Figure 4.1: Execution time of the surrogate model RAPIDD (red lines) as a function of the number livepoints used in MultiNest runs [228, 229]. For reference, the gray lines represent the runtime of the full physics code. The solid (dashed) lines correspond to the case without (with) astrophysical uncertainties.

and the computational gain is due to the polynomials being much cheaper to evaluate than the true N_k^a in eq. (3.2). In Figure 4.1 we compare the execution time of our surrogate model with that of the full physics code as a function of the number of livepoints used in MultiNest. We have observed a consistent improvement of approximately two orders of magnitude in the speed of the computation in the simplest runs with a small number of parameters.

It goes without saying that the method allows for other parametrization functions. We choose polynomials, however, as they are numerically robust, easy to understand and relatively cheap to train. Their usage is further motivated by the fact that the number of DM events in a given energy bin, given by equation (2.1), is in general a smooth function of the DM parameters (mass and couplings) in a given energy range. There are exceptions to this mild behaviour that will require a more careful treatment, namely accidental cancellations due to interference terms between different operators, and threshold effects for low DM masses. We briefly summarise PROFESSOR here before addressing these points.

The objective of PROFESSOR is to translate the exact signal prediction in equa-

tion (2.1) for each bin, $N_k^a(\Theta)$, into an ordinary polynomial, $\mathcal{P}_k^a(\Theta)$. To do so we first choose a polynomial order \mathcal{O} appropriate for the physics problem at hand. With \mathcal{O} and Θ given, the structure of the polynomial is fixed. What remains to be done is to determine the N_{coeffs} coefficients, $d_{k,l}^a$, that allow to approximate the true behaviour of $N_k^a(\Theta)$ such that

$$N_k^a(\Theta) \approx \mathcal{P}_k^a(\Theta) = \sum_{l=1}^{N_{\text{coeffs}}} d_{k,l}^a \tilde{\Theta}_l \equiv \mathbf{d}_k^a \cdot \tilde{\Theta}, \quad (4.1)$$

where $\tilde{\Theta}_l$ are suitable combinations of the actual parameters¹, Θ .

The algorithm to determine \mathbf{d}_k^a requires the knowledge of the exact $N_k^a(\Theta)$ at some randomly sampled points of the parameter space. Having sampled and evaluated N_k^a for at least N_{coeffs} points (a task that can trivially be parallelised) we can construct a matrix equation

$$\vec{N}_k^a = M_{\tilde{\Theta}} \cdot \mathbf{d}_k^a, \quad (4.2)$$

where $M_{\tilde{\Theta}}$ is a matrix where each row contains the values of $\tilde{\Theta}$ for each sampled point, and \vec{N}_k^a is a vector of the resulting number of events. This allows us to solve for \mathbf{d}_k^a using the (pseudo-) inverse of $M_{\tilde{\Theta}}$, which in the PROFESSOR program is evaluated by means of a singular value decomposition.

The minimal number of points (i.e. fully determined matrix) is given by the number of coefficients of an r-th order polynomial in D dimensions. The exact number is given in [223]. We found it beneficial to oversample by approximately a factor of 2 in order to have greater statistics when validating our parameterization.

Although extremely robust and justified whenever Taylor's theorem applies, the validity of the polynomial approximation is not guaranteed and must be checked before attempting any likelihood evaluation. For the most part, standard techniques

¹ For example, for a quadratic polynomial in a two dimensional parameter space $\Theta = (m_\chi, c_1) = (x, y)$, these would take on the form $\mathbf{d}_k^a = (\alpha, \beta_x, \beta_y, \gamma_{xx}, \gamma_{xy}, \gamma_{yy})$, and $\tilde{\Theta} = (1, x, y, x^2, xy, y^2)$.

such as checking the polynomial prediction against its own exact inputs provided by the PROFESSOR toolkit were used. In this work specifically we were confronted with the following limitations:

- (i) Low-mass DM: The number of expected DM events for a given energy bin is in general a smooth function of the DM mass (and therefore susceptible to be fit by a polynomial). The only subtlety to take into account is that, for a given DM mass, there is a maximum recoil energy, given by

$$E_R^{max} = 2 \frac{\mu_{\chi T}^2}{m_T} v_{esc}^2, \quad (4.3)$$

where v_{esc} is the escape velocity in the DM halo. If the incident particle is light enough, experiments will be able to probe the end point of the spectrum, which means that N_k^a is zero above a given energy bin. In our parametrisation, this discontinuity is difficult to fit precisely with a polynomial function. We have circumvented this difficulty by multiplying by a Heaviside step function which automatically incorporates condition (5.2).

- (ii) Accidental cancellations: as already mentioned in the introduction, there are interference terms between the different isospin contributions for each operator, as well as between some of the EFT operators. These subtleties are difficult to capture with the single polynomial approximation proposed in eq.(4.1). Instead, we have found that it is much more convenient to use various polynomials (one for each effective operator, including also the interference term), as follows

$$N_k^a(\Theta) \approx \sum_{ij} \sum_{\tau, \tau'=0,1} \mathcal{P}_k^{a,i,j,\tau,\tau'}(\Theta). \quad (4.4)$$

Building the parametrisation in this way makes the training stage quicker, because the required number of sample points is reduced. Solving equation (4.2) for the coefficients in a lower dimension is also quicker than in a higher dimension, which compensates for building multiple polynomials for each di-

Target	Exposure	Energy window	Bin No
Xe	5.6×10^6 kg days	3-30 keV	27
Ge	91250 kg days	0.35-50 keV	49
Ar	7.3×10^6 kg days	5.0-30 keV	24

Table 4.1: Specifications of the direct detection experiments considered in this chapter. Bin no. refers to the number of equally spaced bins we use for each target.

mension.

- (iii) Precision loss: For consistency, we have monitored the precision of the surrogate model by comparing the DM spectrum obtained for the best fit point with the surrogate model and with the physics code. We have found that in general the agreement was excellent, well below 1% for the examples shown in this paper. We have found that precision can be lost in some cases of high dimensionality, but that this behaviour can be corrected if a higher order in the polynomial fit is used. Likewise, the surrogate model can be less precise towards the edges of the parameter space used in the training phase. This is easily avoided by training the surrogate model in a wider window than for the intended use.

4.2 Examples

In this section we consider various simple examples that allow us to validate our surrogate model. We have selected various DM benchmark points that are within the reach of future G2 experiments and we have attempted to reconstruct the DM parameters (mass and couplings) using RAPIDD, and compare it with the full calculation.

In Table 4.1, we summarise the experimental configurations that we have considered in this work. These were motivated by future direct detection experiments. The

energy ranges were chosen so as to mimic the planned G2 experiments SuperCDMS [230] (for Ge and Si), LZ, XENON1T, PandaX [104, 231, 232] (for Xe) and DarkSide [112] (for Ar). The values for the exposures have been chosen to mimic G2 for xenon and argon targets with LZ [231] (~ 15 tonne year) and Darkside-20k (~ 20 tonne year) respectively. On the other hand, to maximise the complementarity, we chose a even further future germanium experiment, with roughly five times the expected exposure of SuperCDMS [230] (2.04×10^4 kg days). It is important to note, however, that at this point we are not interested in replicating the whole experimental setup, and for simplicity we also assume a constant efficiency, $\varepsilon(E_R) = 1$, and perfect energy resolution, $Res(E'_R, E_R) = \delta(E'_R - E_R)$, in Eq. (2.1). These quantities vary from experiment to experiment, and can be straightforwardly incorporated in our method, only having a cost in the initial training time.

The parameter reconstruction is carried out using MultiNest 2.9 [228, 229], which is interfaced with RAPIDD. In order to test the results with the full computation, we also interface MultiNest to our own numerical code that computes the number of recoil events using Eq.(2.1). In both cases, we use the same definition for the likelihood, based on a binned analysis of the resulting data. Scans are performed with 15000 live points and a tolerance of 0.0001 to reach a good sampling of the profile likelihood (defined below) as found in Ref. [233].

The experimental data consists of the predicted sets of binned DM rates for each target, $\mathbf{D} = (\{\lambda_k^a\})$. The parameter space is therefore $\Theta = (m_\chi, c_i^r)$. Logarithmic priors are assumed for the EFT couplings and for the DM mass. Regarding the properties of the DM halo, in the first examples we will consider the Standard Halo Model (SHM). The SHM is characterised by an isotropic Maxwell-Boltzmann velocity distribution function [234] in Eq. 2.1. We have used the following values for the local dark matter density, $\rho_0 = 0.4 \text{ GeV cm}^{-3}$, central velocity, $v_0 = 220 \text{ km s}^{-1}$, and escape velocity, $v_{esc} = 544 \text{ km s}^{-1}$. In this first example, we have not incorporated

uncertainties in these quantities, but we will address this in Section 4.2, together with the generalisation to other DM halos.

One operator: spin-independent scattering

In order to tune our method, we have started with a canonical scenario, where the DM-nucleus scattering cross section is described by a single operator. We have chosen \mathcal{O}_1 , which corresponds to the standard spin-independent scattering, and we have assumed that the couplings of the DM to protons and neutrons are equal. We are therefore left with a two-dimensional parameter space (m_χ, c_1^0) .

We have chosen two benchmark points, a low mass case with $m_\chi = 30$ GeV and a higher mass case, where $m_\chi = 100$ GeV. The coupling to \mathcal{O}_1 is $c_1^0 = m_\nu^2 \tilde{c}_1^0 = 5 \times 10^{-5}$ in both cases. Where we can relate these values to the zero-velocity spin-independent DM-nucleon scattering cross-section in Eq(2.30). In these examples we are considering purely isoscalar couplings ($c_i^p = c_i^n = c_i^0$). The parameterization was trained using 1000 random points in the (m_χ, c_1^0) plane.

In Figure 4.2 we show the reconstruction of DM parameters for both benchmark points, the light mass, which is shaded red, and the high mass which is shaded blue. The black lines indicate the 2σ (95% C.L.) and 1σ (68% C.L.) regions calculated by the physics code. We have assumed observation in a future xenon experiment with setup as in Table 4.1. The best fit points are, respectively, $(m_\chi, c_1^0) = (30.0 \text{ GeV}, 5.00 \times 10^{-5})$ and $(99.7 \text{ GeV}, 4.99 \times 10^{-5})$, and the 1σ and 2σ regions span the same areas. Without having lost accuracy, the great advantage of the parametrisation method is its speed. While the full computation took approximately 40 minutes for each example, the results using the surrogate model took just 10 seconds (after an initial training phase of approximately 2 minutes). To calculate

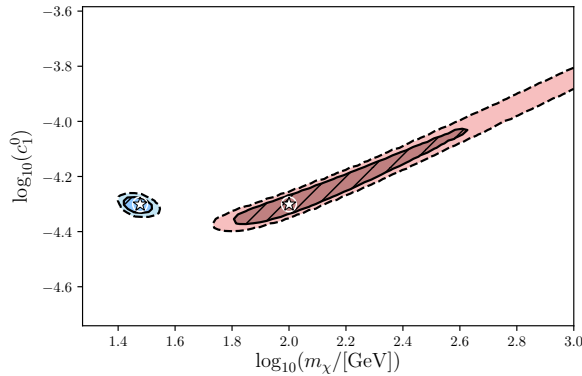


Figure 4.2: Reconstruction of DM parameters in the (m_χ, c_1^0) plane for two benchmark points. The best-fit point and 1σ (68% C.L.) and 2σ (95% C.L.) regions are shown for the results obtained with RAPIDD (red cross and shaded areas) and the full physics code (black stars and solid and dashed black lines).

the contours in these plots we have used functions provided by Superplot [180].

As mentioned in Section 4.1, low DM masses are a potential challenge for our surrogate model. With this test we have shown that RAPIDD is reliable in this mass regime.

Operator interference and isospin-violating couplings

As explained in Chapter 2, each operator’s response is summed over proton and neutron interaction (or equivalently, isoscalar and isovector interactions). Likewise, there are interference terms among some of the EFT operators. Due to the resulting interference terms, accidental cancellations can occur between these responses. For example, the interaction rate of isospin-violating dark matter [235–238] is extremely sensitive to the nuclear target. In fact, for specific choices of DM couplings to protons and neutrons, one can greatly suppress the expected rate in certain targets, a strategy that has been employed to try to reconcile positive DM hints (such as

DAMA and CoGeNT) with the negative results from other experiments (mainly XENON). For a recent review on isospin-violating DM models, see Ref. [239].

This finely tuned cancellation is a challenge for our parametrisation technique. In particular, we have checked that a polynomial approximation of the total response, dR/dE_R , is unable to properly capture this subtle behaviour. As already mentioned in Section 4.1, this problem can be addressed by using independent parametrisations for each isospin contribution and for each interference term, as in equation (4.4). In this particular example, we will use different polynomials for each of the three contributions, \mathcal{P}_k^{00} , \mathcal{P}_k^{10} , and \mathcal{P}_k^{11} . Each of these vary smoothly with the input parameters (m_χ , c_1^0 , c_1^1) and this ensures a much more reliable reconstruction, including cancellations.

We show in Figure 4.3 the results of a three-dimensional scan (m_χ , c_1^0 , c_1^1) for a benchmark point that exhibits a large degree of fine-tuning. When comparing to the result using the full calculation, we can observe that our parametrisation method recovers the correct shape of the reconstructed areas, including the region where the negative interference takes place. As in previous examples, the time employed by our method was considerably shorter. Notice that the best fit point in our reconstruction (red cross) does not coincide with that of the nominal point (black star). However, the best-fit point calculated by RAPIDD is well within the 1σ contour.

Having proved that this prescription treats cancellations accurately, RAPIDD's default setting is to produce output from a series of polynomials as described in equation (4.4).

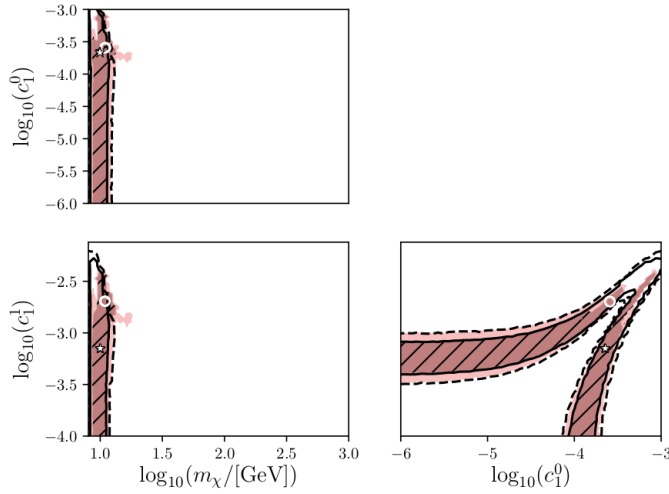


Figure 4.3: Reconstruction of DM parameters in (m_χ, c_1^0, c_1^1) . The best-fit point and 1σ (68% C.L.) and 2σ (95% C.L.) regions are shown for the results obtained with RAPIDD (red cross and shaded areas) and the full physics code (black star and solid and dashed black lines).

Generalised DM halos

As reviewed in Chapter 3 the SHM is the canonical choice used to present the results from direct detection experiments. It is particularly convenient because the velocity integral can be solved analytically, which greatly reduces computing time. However, as seen previously, there are strong motivations to move beyond the SHM, and when we do, direct detection experiments are affected by these variations [161,164,240–242], especially when probing low-mass DM candidates [241]. For example, changes in the velocity distribution function can significantly alter the population of DM particles with enough speed to produce recoils above the experimental threshold.

Our surrogate model can be easily adjusted to a general velocity distribution function. In fact, it is for general halos that this method is more advantageous: whereas the full calculation relies on numerically solving the velocity integral, in our method, this only has to be done in the training phase.

As a final test of our method, we have applied our reconstruction routine to the same example as in the previous subsections, but considering a generalised DM halo, defined by Eqn.(3.14), considering variations in the halo parameters as $v_{esc} \in [478, 610] \text{ km s}^{-1}$, $v_0 \in [170, 290] \text{ km s}^{-1}$, $k \in [0.5, 3.5]$ as well as $\rho_0 \in [0.2, 0.6] \text{ GeV cm}^{-3}$ [197–200], which are included in our scan as nuisance parameters. These ranges are consistent (although broader) than those obtained in recent analysis of N-body simulations that include the effect of baryons Ref. [196, 201].

Figure 4.4 shows the resulting reconstruction of DM parameters in this generalised halo. As expected, the 1σ and 2σ regions are wider as a consequence of astrophysical uncertainties. Since the benchmark point in this example is of relatively high mass, our xenon experiment will not probe the tail of the halo function. Therefore, remembering the results from Section 3.2, uncertainties in k , v_0 and v_{esc} will not provide large variations in our parameter reconstruction. Instead, the uncertainty in ρ_χ provides a simple scaling uncertainty in the strength of coupling. This can be seen when we compare Figure 4.4 to the higher mass BP in Figure 4.2, the contours are simply fatter.

As for validating RAPIDD, like in the previous examples, we observe no difference between the results obtained with RAPIDD and those obtained with the full physics code. We therefore conclude that our surrogate model is fast and reliable, and easily applicable to generalised DM halos.

Finally, RAPIDD can also incorporate velocity distribution functions which are defined as a function of the velocity, but not necessarily given by an analytical formula. This is useful to interpret results from numerical simulations (see e.g., Refs. [196, 242]).

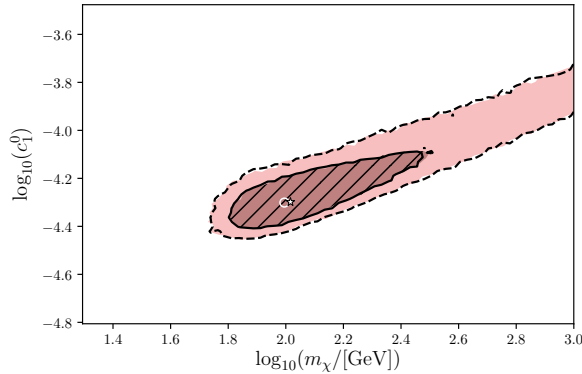


Figure 4.4: Reconstruction of DM parameters in the (m_χ, c_1^0) plane when astrophysical uncertainties are included. The best-fit point and 1σ (68% C.L.) and 2σ (95% C.L.) regions are shown for the results obtained with RAPIDD (red cross and shaded areas) and the full physics code (black star and solid and dashed black lines).

4.3 Simplified dark matter models

Having proved the reliability and speed of RAPIDD in the previous section, we will now exploit this tool to illustrate how future data might constrain DM parameters in a multi-dimensional parameter space. In this section we consider a set of simplified DM models, as described in chapter 3. The EFT operators for direct detection can be recovered in the non-relativistic limit [220]. For concreteness, the relation between models and operators is as follows: SS $\{\mathcal{O}_1, \mathcal{O}_{10}\}$, SV $\{\mathcal{O}_1, \mathcal{O}_7\}$, FS $\{\mathcal{O}_1, \mathcal{O}_6, \mathcal{O}_{10}, \mathcal{O}_{11}\}$, FV $\{\mathcal{O}_1, \mathcal{O}_4, \mathcal{O}_7, \mathcal{O}_8, \mathcal{O}_9\}$.

We will consider a hypothetical future situation in which several direct detection experiments observe an excess in their data that can be attributed to DM particles. We will attempt to reconstruct the data within the context of different simplified models. As already mentioned in Chapter 3, in general, a single experimental target is unable to unambiguously determine the DM couplings, thus we consider a signal in three targets, Ge, Xe, and Ar.

Name	Model	DM Parameters	N_{Xe}	N_{Ge}	N_{Ar}
BP1	SS	$m_\chi = 10 \text{ GeV}$ $c_1 = 1 \times 10^{-4}$ $c_{10} = 5$	93	10	50
BP2	SS	$m_\chi = 100 \text{ GeV}$ $c_1 = 3 \times 10^{-5}$ $c_{10} = 5 \times 10^{-1}$	206	2	30
BP3	FS	$m_\chi = 30 \text{ GeV}$ $c_1 = 0.0$ $c_6 = 60$ $c_{10} = 0.0$ $c_{11} = 0.0$	256	1	0

Table 4.2: Benchmark points considered in this chapter. They all satisfy experimental constraints from direct detection experiments, and are within the reach of next generation detectors. For reference, we indicate the total number of DM events expected in each of the experimental configurations of Table 4.1.

We have selected a number of benchmark points, shown in Table 4.2, all of which satisfied the experimental bounds from direct detection experiments prior to XENON1T results. We include one example with a low-mass DM particle (BP1) and another one with a heavier candidate (BP2), since they give rise to different issues in the parameter reconstruction. We have also chosen a point motivated by Pseudoscalar-mediated DM [140, 237] (BP3).

As mentioned in Chapter 3 we have assumed universal couplings of the DM to quarks, which leads to a specific relation between the isoscalar and isovector components of the DM-nucleus coupling [216], thereby effectively reducing the dimensionality of the parameter space. Here we have presented our benchmark point in terms nucleon independent couplings, but quark universality requires that $c_1^p = c_1(1.96/2.0) = c_1^n/0.96$ and $c_{10}^p = c_{10}(1.6) = c_{10}^n/0.25$ for the SS BPs, whereas for the FS BP isospin is conserved $c_i^p = c_i^n = c_i$.

For each benchmark point, we have generated mock data for the experimental setups of Table 4.2. Then, using this data, we have attempted to reconstruct the

DM parameters (mass and couplings) for each simplified DM model (SS, SV, FS, FV) using RAPIDD linked with MultiNest. In all cases, we have computed the reconstruction corresponding to each individual target, as well as the one resulting from the combination of data from the three targets. For brevity, we only show the resulting profile likelihoods in the multi-dimensional parameter space to describe some results more clearly, the most important result from this section is the DM spectra corresponding to the best-fit points in each model.

BP1 (light DM):

Our first benchmark point, with $m_\chi = 10$ GeV, is an example of low-mass DM candidate which provokes both the \mathcal{O}_1 and \mathcal{O}_{10} responses at similar strengths. Ordinarily, these operators are fairly distinguishable since they have different momentum dependence (q^0 and q^1 for \mathcal{O}_1 and \mathcal{O}_{10} respectively). However, due to the small DM mass, the characteristic peak of \mathcal{O}_{10} spectrum is below the analysis threshold for xenon and therefore, can be mistaken for the typical exponential behaviour of a q -independent response. This is a challenge for parameter reconstruction that can be alleviated through the use of multiple targets. The profile likelihoods shown in Figure 4.5 illustrate this point very well.

Figure 4.5 shows the the 2σ contours of single target experiments such as xenon, germanium and argon with colors blue, green and orange respectively. For the low masses that we are considering, the responses of operators \mathcal{O}_1 and \mathcal{O}_{10} are very similar in both germanium and xenon. When you consider both experiments simultaneously you start to see tension between them, exhibited by the contours in the $\{\mathcal{O}_1, \mathcal{O}_{10}\}$ plane, which start to separate in the low c_1 region. However, these two targets are unable to resolve the degeneracy and in principle, only are able to place an upper bound on the corresponding couplings.

We can observe this effect in the $\{\mathcal{O}_1, \mathcal{O}_{10}\}$ plane of Figure 4.5, where the germanium contours are not closed. The argon target plays a pivotal role in breaking the degeneracy by virtue of the detector being insensitive to the spin-dependent interaction \mathcal{O}_{10} . The insensitivity is shown by the orange vertical contour in the $\{\mathcal{O}_1, \mathcal{O}_{10}\}$ plane. When running the reconstruction with all experiments, closed contours in SS are achieved.

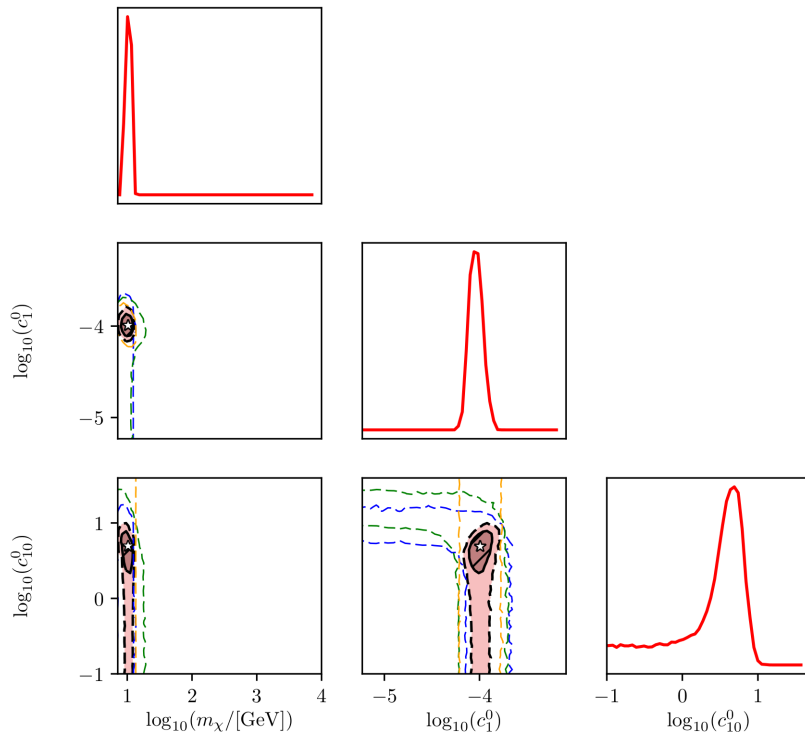


Figure 4.5: Profile likelihood for the reconstruction of DM parameters for the simulated data of benchmark point BP1, using simplified model SS. Dashed blue, green, and orange lines correspond to the 2σ (95% C.L.) contours obtained for individual targets of xenon, germanium, and argon. The light and dark pink shaded regions bounded by black dashed and solid lines correspond to the 1σ (68% C.L.) and 2σ (95% C.L.) contours obtained for the combination of the three targets. The best fit point is represented by an white star. For reference, the one-dimensional profile likelihoods are also shown.

The full reconstructions for the SV, FS and FV models are not shown because they tell a very similar story, with the exception that for the fermion DM models, there is much greater freedom with coefficients. This translates into great blocks of

unconstrained parameter space, and contours which are unable to be closed.

In Figure 4.6, we show the DM differential rate obtained for the best fit points in each simplified model and target. The different columns represent, from left to right, SS, SV, FS, and FV, and the different rows represent, from top to bottom, Ge, Xe, and Ar. The vertical grey dashed lines represent the energy range used in the fit for each target. In each plot, the red line corresponds to the differential rate predicted by the benchmark point (BP1), and the thick, dashed, black line is the differential rate obtained for the best-fit point (combining the data of the three targets). The individual contributions from NREFT operators are shown by means of a dot-dashed lines (for operators with a canonical momentum dependence) and dotted lines (for operators with an extra momentum-dependence). The table below the plot indicates the parameters for the best-fit point in each simplified model, using the same colour code as the figure.

As the results show, the DM mass is very well-reconstructed around the nominal value. Given the small DM mass, the end-point of the DM spectrum falls within the energy range analysed in the three experiments. Notice that this argument is independent of the effective operator (the right mass is obtained in all scenarios), and therefore it does not help in discriminating the different models.

In all four models, the reconstruction favours a leading contribution from operator \mathcal{O}_1 , consistent with the original benchmark point. The small contribution from a momentum-dependent operator is either attributed to \mathcal{O}_{10} , (in SS and FS) or \mathcal{O}_9 (in FV).

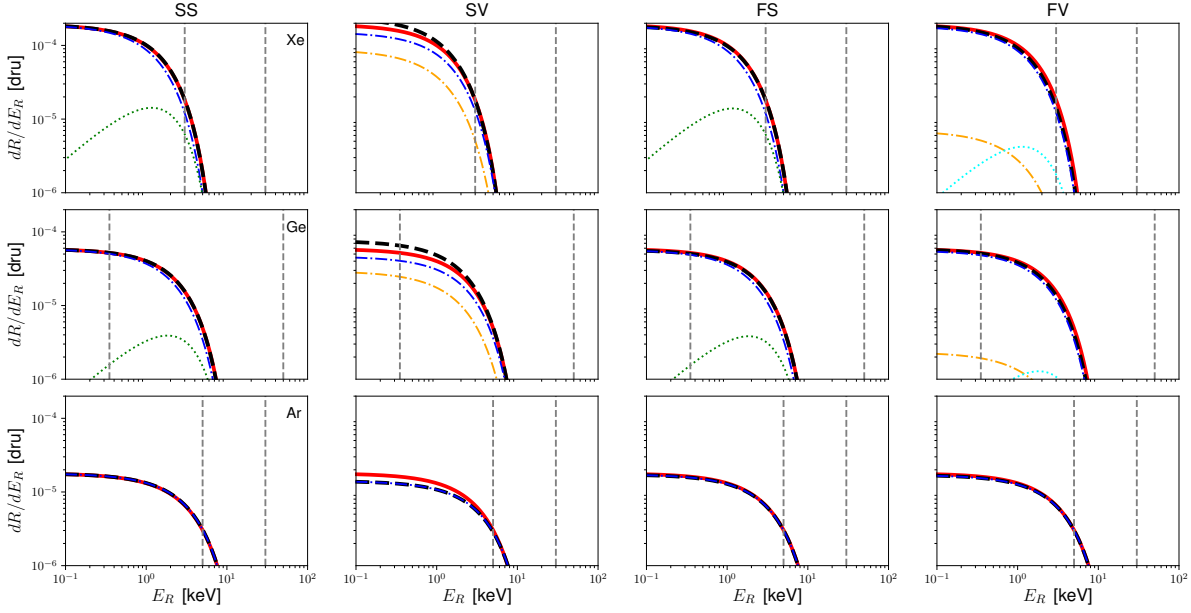
In fact the FV example is particularly interesting in this case because given the shape of \mathcal{O}_9 , one might assume that a better fit should be achievable. Remember however that the size of c_9 directly implicates the size of both c_7 and c_8 . Both \mathcal{O}_7

and \mathcal{O}_8 have similar spectra to \mathcal{O}_1 but importantly are different in the tail, and thus unable to be viable replacement for c_1 . Therefore, both contributions have to be kept to a minimum, restricting the effect \mathcal{O}_9 can have.

In order to quantify and compare the goodness of the resulting fits, we have computed the log-likelihood of each best-fit point, as given by the likelihood. We can observe that a relatively good fit is obtained in all four scenarios, with a slight preference for the right model SS and also FS (but only in the scenario where FS→SS).

Notice that in this kind of analysis, it is customary to compare hypothesis by means of the Bayesian evidence, however, we are dealing with models of different dimensionality and we would observe the rather trivial result that models with more free parameters are favoured. As explained for example in Ref. [218], one could start by calculating the evidence for 2D slices of the parameter space and thus identify the most likely set of parameters before moving to larger dimensions.

Finally, as a consistency check, we have compared the binned DM spectrum for the best fit points obtained with RAPIDD and with the full physics code. We have observed that the number of DM events per bin obtained with the surrogate model and the real one differ by less than 1% when fourth order polynomials are employed for models SS, SV, and FS. We have found that model FV requires a fifth order polynomial to attain the same degree of precision.



$m_\chi = 10.3 \text{ GeV}$ $c_1 = 1.01 \times 10^{-4}$ $c_{10} = 4.89$	$m_\chi = 11.2 \text{ GeV}$ $c_1 = 9.23 \times 10^{-5}$ $c_7 = 69.4$	$m_\chi = 10.3 \text{ GeV}$ $c_1 = 9.93 \times 10^{-5}$ $c_6 = 24.1$ $c_{10} = 4.80$ $c_{11} = 1.10 \times 10^{-4}$	$m_\chi = 10.5 \text{ GeV}$ $c_1 = 9.85 \times 10^{-5}$ $c_4 = 4.30 \times 10^{-3}$ $c_7 = 18.7$ $c_8 = 1.52 \times 10^{-2}$ $c_9 = -1.66$
$\log \mathcal{L}(SS) = -29.9$	$\log \mathcal{L}(SV) = -30.3$	$\log \mathcal{L}(FS) = -29.9$	$\log \mathcal{L}(FV) = -33.9$

Figure 4.6: Reconstruction of parameters for BP1: Differential rate as a function of the recoil energy corresponding to the best fit point in each simplified models (columns) and for each of the experimental targets (rows). The thick black line corresponds to the full differential rate obtained from the best fit point (after combination of data from the three targets) in each of the simplified models. For reference, the thick red line shows the differential rate corresponding to the benchmark point. The thin dotted (dot-dashed) lines represent the individual contributions from momentum dependent (independent) operators. The vertical dashed lines delimit the energy range explored for each target. The table indicates the parameters for the best fit points in each case (using the same colour code as the lines in the plots), and the value for its log-likelihood calculated using eq. 3.2. Gray shading is used to denote the true model (SS in this case).

BP2 (Heavy DM)

We now turn our attention to a larger value of the DM mass. Benchmark point BP2 features a 100 GeV particle. This implies that the resulting spectrum is flatter and displaced towards larger values of the recoil energy. It should be noted that with the configurations chosen in Table 4.1, only the xenon and argon targets would be sensitive to this signal. Since we have assumed a smaller exposure for germanium, the expected number of events for this target is merely $N_{\text{Ge}} = 1$, which only leads an upper bound in the corresponding couplings.

Due to the heavier DM mass, the endpoint of the recoil spectrum lies beyond the energy window of all three targets, which makes its reconstruction more difficult. Moreover, the (small) contribution from the momentum-dependent operator \mathcal{O}_{10} flattens out the spectrum at large energies. This is properly identified in models SS and FS (for which the resulting value of c_{10} is comparable to that of the original benchmark point), resulting also in a very good reconstruction of the DM mass. However, in the SV model for which there is no momentum-dependent operator and for FV where \mathcal{O}_9 is severely constrained by its relation to \mathcal{O}_7 and \mathcal{O}_8 , the best fit is obtained for a much larger value of the DM mass (in model SV the best fit is actually towards the boundary of the reconstructed area with $m_\chi \sim 1000$ GeV), so as to compensate for the flatter spectrum.

To illustrate this point, the full profile likelihood in the whole parameter space can be found in Figures 4.7 (SS), 4.8 (SV). As we see in these plots, the reconstructed DM mass has a large uncertainty, and even if the right value is obtained for the best-fit point (model SS), the 2σ region is unbounded from above. This effect is well known, and is exacerbated by astrophysical uncertainties in the DM escape velocity [164, 243]. Possible ways to improve this from the experimental side will be discussed more in Chapter 5.

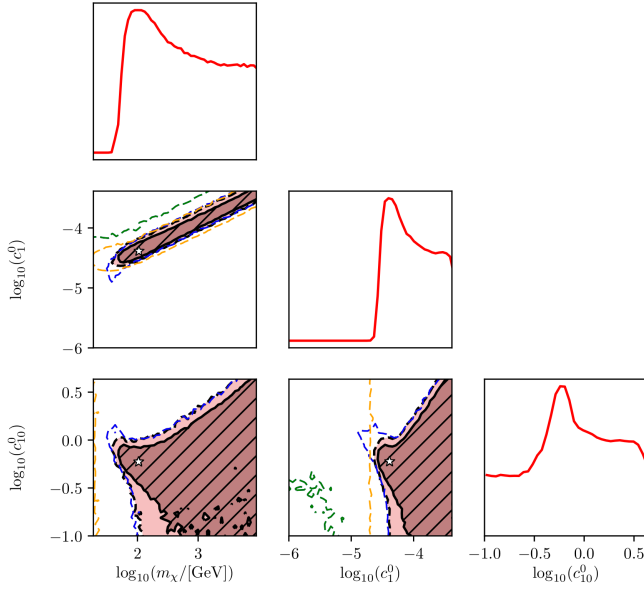


Figure 4.7: Profile likelihood for the reconstruction of DM parameters for the simulated data of benchmark point BP2, using simplified model SS. Much like Figure 4.5, dashed blue, green, and orange lines correspond to the 2σ (95% C.L.) contours obtained for individual targets of xenon, germanium, and argon. The light and dark pink shaded regions bounded by black dashed and solid lines correspond to the 1σ (68% C.L.) and 2σ (95% C.L.) contours obtained for the combination of the three targets. The best fit point is represented by an white star. For reference, the one-dimensional profile likelihoods are also shown.

Perhaps more subtly, however, is the fact that the vector mediated model is unable to reproduce this extra flatness coming from the secondary response \mathcal{O}_{10} . We see in the 1D profile likelihood in Figure 4.8 there seems to be very little preference for a particular mass and it in fact disfavours the "true" mass of BP2. When we compare this to Figure 4.7 we see a preference for a specific mass.

However, statistically speaking, both interpretations are still completely valid as we can see in the Figure 4.10. This Figure shows how well all models are able to reproduce the spectrum. Where the most important spectra for this data set are the xenon and argon ones. Once again we see $FS \rightarrow SS$ with the best-fit point. We do see however that if germanium exposure such that the signal was seen clearly, the models SV and FV would be less able to match the data. Furthermore, Figure 4.10

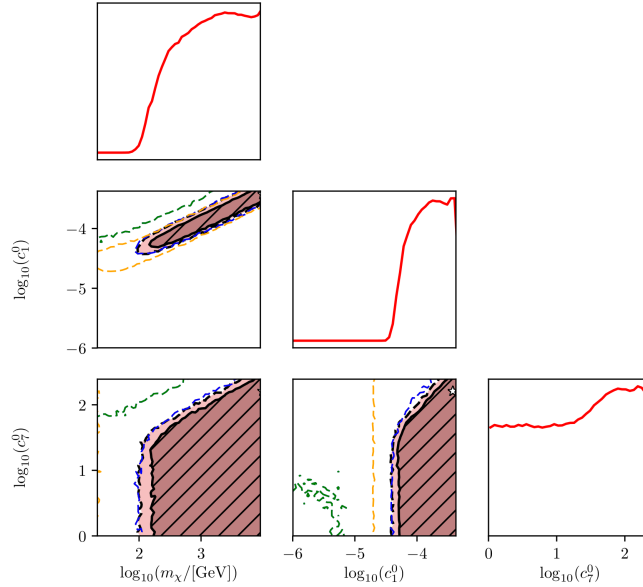


Figure 4.8: The same as in Figure 4.7, but for simplified model SV.

shows that pushing the signal region of interest ROI to higher recoil energies will improve model discrimination.

In the table below Figure 4.10, the recoil spectra of the reconstructed points are very similar for models SS and FS. This is not surprising, since once more the response in both cases is dominated by the same set of operators. These two models are difficult to disentangle using direct detection alone, but as recent analyses points out, a combination with LHC data could shed light onto the nature of the DM and the mediator [244].

The goodness of the fit for models SV and FV is not much worse, but the reconstructed areas are extremely degenerate. For example in model FV there is a complete degeneracy between operators \mathcal{O}_1 , \mathcal{O}_4 , \mathcal{O}_7 and \mathcal{O}_8 as shown in Figure 4.9. The severe degeneracies are not present in the results for BP1 and this is because the tail of the spectrum is being probed in experiments. It is this region that allows one to make some discrimination between these operators. Moreover, in the high m_χ limit

the \mathcal{O}_9 coefficient becomes completely dependent on c_8 and due to the dominance in strength of the \mathcal{O}_8 form factors over that of \mathcal{O}_9 , there is no chance of using \mathcal{O}_9 to flatten the spectrum in the way that \mathcal{O}_{10} does for the scalar mediated models.

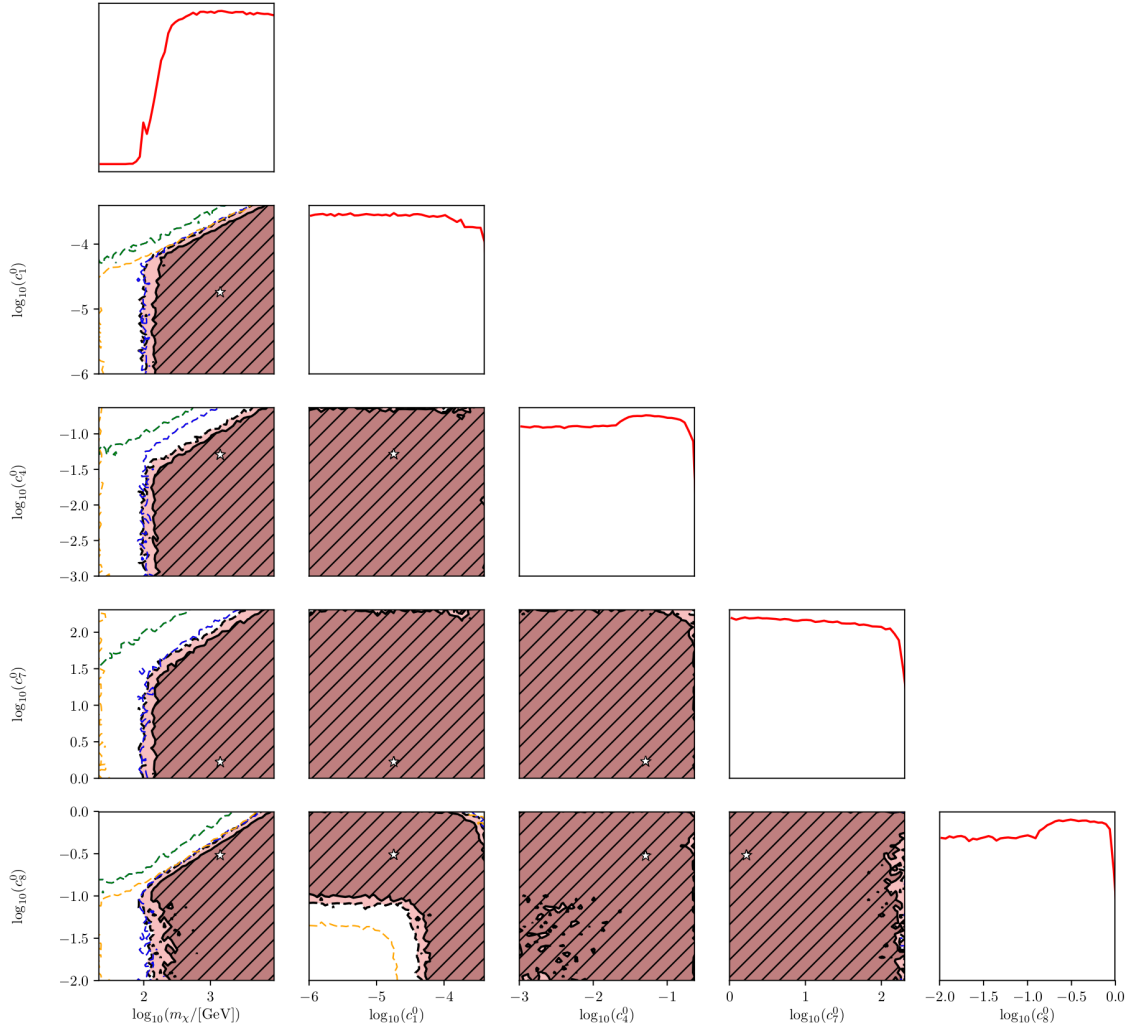
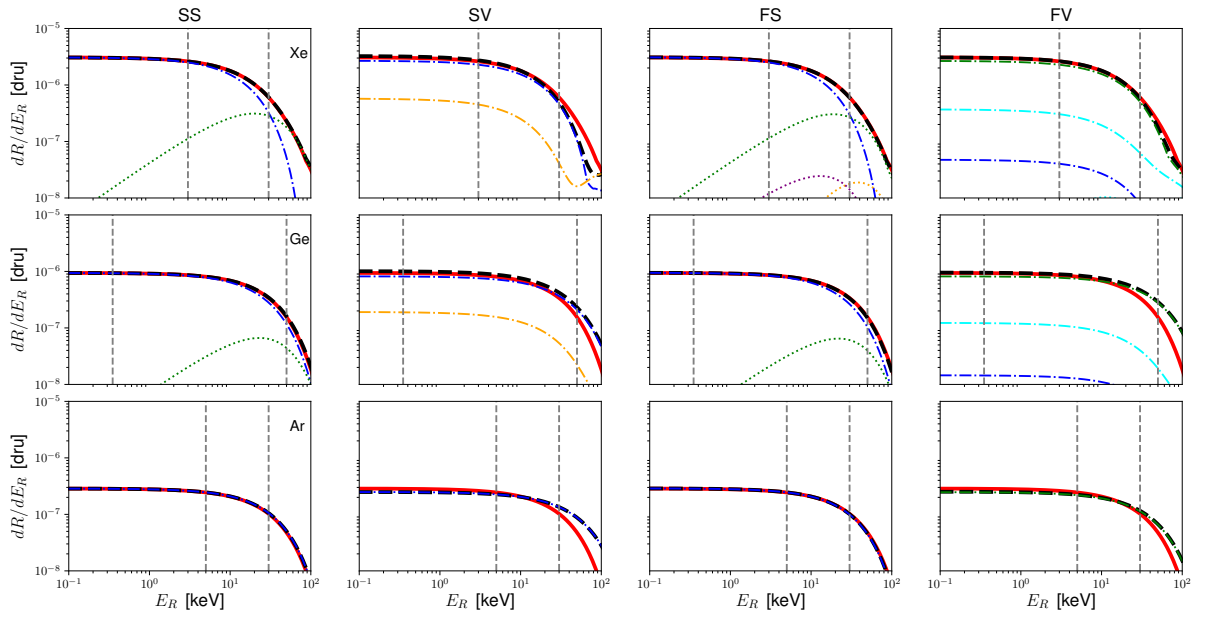


Figure 4.9: The same as in Figure 4.7, but for simplified model FV.



$m_\chi = 105 \text{ GeV}$ $c_1 = 4.11 \times 10^{-5}$ $c_{10} = 0.595$	$m_\chi = 989 \text{ GeV}$ $c_1 = 3.79 \times 10^{-4}$ $c_7 = 161$	$m_\chi = 95.7 \text{ GeV}$ $c_1 = 3.90 \times 10^{-5}$ $c_6 = 3.22$ $c_{10} = 0.570$ $c_{11} = 1.85 \times 10^{-4}$	$m_\chi = 1403 \text{ GeV}$ $c_1 = 1.81 \times 10^{-5}$ $c_4 = 5.14 \times 10^{-2}$ $c_7 = 1.69$ $c_8 = 3.04 \times 10^{-1}$ $c_9 = 0.303$
$\log \mathcal{L}(SS) = -85.2$	$\log \mathcal{L}(SV) = -86.0$	$\log \mathcal{L}(FS) = -85.2$	$\log \mathcal{L}(FV) = -85.4$

Figure 4.10: The same as in Figure 4.6, but for benchmark point BP2.

Momentum-dependent DM (BP3)

Finally, we have selected an example based on fermion DM with a pure pseudo-scalar mediator (model FS with only operator \mathcal{O}_6), since this gives rise to a very characteristic spectrum which vanishes at small recoil energies. Notice that given our choice of parameters for benchmark point BP3 of Table 4.2, only xenon sees a relevant number of DM events, since the exposure in germanium is insufficient and \mathcal{O}_6 does not produce a response in Argon. However, the data from the other targets is still useful to set up upper bounds on specific operators as we see in Figure 4.11 and Figure 4.12.

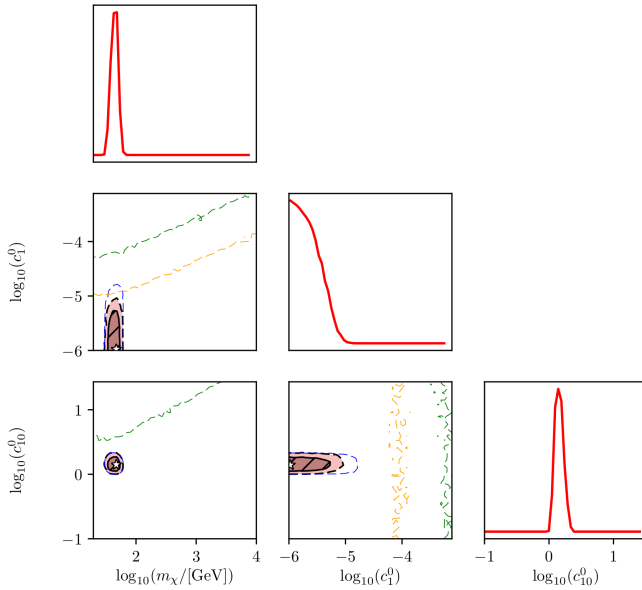


Figure 4.11: Profile likelihood for the reconstruction of DM parameters for the simulated data of benchmark point BP3, using simplified model SS. Much like Figure 4.5, dashed blue, green, and orange lines correspond to the 2σ (95% C.L.) contours obtained for individual targets of xenon, germanium, and argon. The light and dark pink shaded regions bounded by black dashed and solid lines correspond to the 1σ (68% C.L.) and 2σ (95% C.L.) contours obtained for the combination of the three targets. The best fit point is represented by an white star. For reference, the one-dimensional profile likelihoods are also shown.

In Figure 4.11 we see that germanium and argon targets are able to improve the

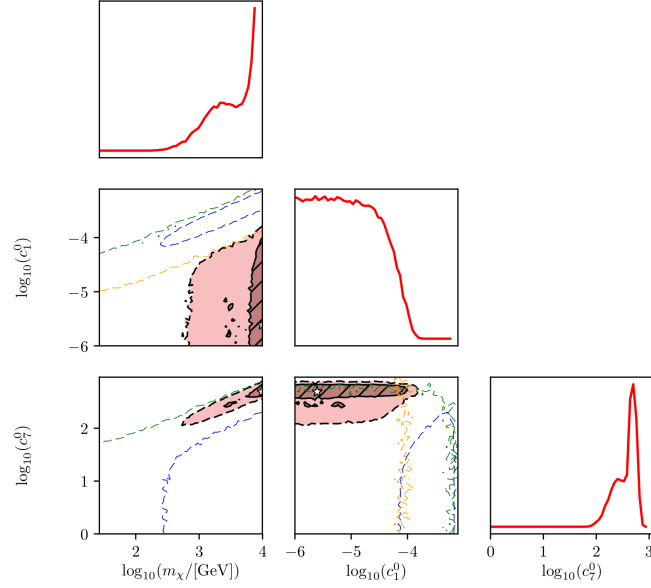


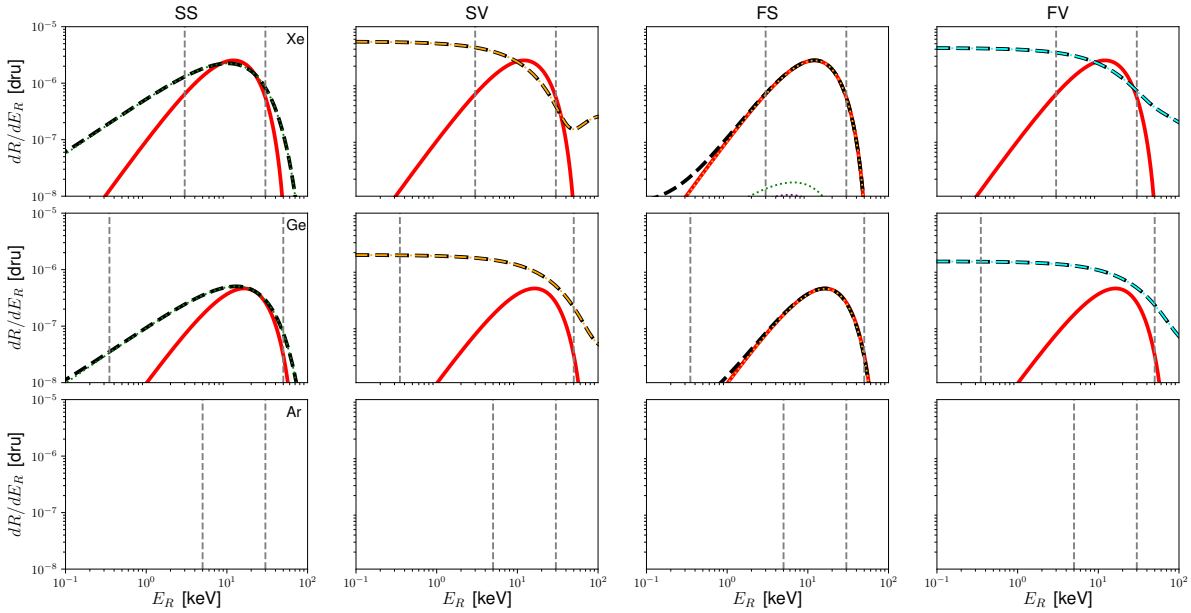
Figure 4.12: The same as in Figure 4.11, but for simplified model SV.

reconstruction only in a small way. For example the $\{m_\chi, c_1\}$ plane shows how argon can provide some complementarity by restricting some parameter values allowed by xenon alone. In model SS, the best fit is obtained for large \mathcal{O}_{10} , as it has a non-trivial momentum dependence, much like the BP's \mathcal{O}_6 leading response. We have not shown the FS profile likelihoods, but they quite clearly favor \mathcal{O}_6 responses.

Complementarity really comes into play when the wrong model is being considered. Taking the SV scan in Figure 4.12, one can see in the $\{m_\chi, c_1\}$ plane how the argon exclusion is completely inconsistent with the best fit region from the xenon experiment. A similar situation occurs for the FV scan. The substantial tension between the areas obtained using only xenon data and those using the other targets, causes problems for interpreting the data for these models. If only xenon data is considered, the best fit areas favour a leading contribution from operator \mathcal{O}_1 . When argon data is included, the best-fit area corresponds to large values of \mathcal{O}_7 in model SV or \mathcal{O}_4 in FV (to which argon is insensitive). It is also worth noting that without this tension we know that the \mathcal{O}_1 would be a bad fit to the \mathcal{O}_6 signal, but the tension

between experiments is valuable information when trying to find the best model.

Figure 4.13 shows the differential DM rate corresponding to the best fit points in each model. We can now observe that only the right scenario (FS) produces a good fit to the signal and this is because $FS \rightarrow SS$ is no longer possible. The reason is that \mathcal{O}_6 is the only operator of the set considered here that is q^2 dependent. In contrast, \mathcal{O}_{10} only depends on q and thus leads to a different shape. As the table below Figure 4.13 shows, the statistically preferred model coincides with the true model quite unequivocally.



$m_\chi = 47.0 \text{ GeV}$ $c_1 = 1.06 \times 10^{-6}$ $c_{10} = 1.39$	$m_\chi = 9920 \text{ GeV}$ $c_1 = 2.48 \times 10^{-6}$ $c_7 = 4.91 \times 10^2$	$m_\chi = 30.9 \text{ GeV}$ $c_1 = 1.00 \times 10^{-6}$ $c_6 = 59, 8$ $c_{10} = 0.126$ $c_{11} = 1.02 \times 10^{-4}$	$m_\chi = 9966 \text{ GeV}$ $c_1 = 2.35 \times 10^{-6}$ $c_4 = 0.469$ $c_7 = 1.40$ $c_8 = 1.21 \times 10^{-2}$ $c_9 = 1.20 \times 10^{-2}$
$\log \mathcal{L}(SS) = -62.6$	$\log \mathcal{L}(SV) = -103$	$\log \mathcal{L}(FS) = -58.9$	$\log \mathcal{L}(FV) = -84.4$

Figure 4.13: The same as in Figure 4.6, but for benchmark point BP3. No events are expected for argon in the last row of plots.

As in previous examples, we have checked the accuracy of the surrogate model in the best fit points, obtaining a difference of less than a 1% with the full physics

computation.

4.4 Summary

In this chapter we have introduced RAPIDD, a surrogate model to compute the binned DM spectrum in direct detection experiments. RAPIDD substitutes the full physics computation with a much faster parametrisation in terms of ordinary polynomials of the DM mass and couplings. The surrogate model is initially trained for a given choice of parameters using the full calculation of the DM rate for a given set of direct detection experiments. The parametrisation is then extracted using the PROFESSOR tool.

We have validated our surrogate model using a range of examples that explore the reconstruction of DM parameters using mock-data in the multi-dimensional parameter space of effective field theories motivated from simplified DM models. We have identified and overcome two difficulties, corresponding to the case of low-mass dark matter and the interference between different operators. We have also checked that RAPIDD can successfully incorporate a generic DM halo, as such obtained from N-body simulations, and include astrophysical uncertainties in the halo parameters. In a few selected benchmark points, we have compared our results with those of the full physics calculation, obtaining a perfect agreement and a runtime approximately two orders of magnitude smaller.

As a final test of the full potential of RAPIDD, we have attempted the reconstruction of DM parameters in the context of a set of simplified models using three experimental setups, inspired by future DM detectors. We have considered the cases of scalar and fermion DM particles, with either scalar or vector mediators. In these models,

the dimensionality of the parameter space (once astrophysical uncertainties are included as nuisance parameters) ranges from six to nine dimensions and include operators with non trivial momentum dependence. We have found that fourth order polynomials provide a good fit, with errors smaller than 1%, except for the example with highest dimensionality, where fifth order polynomials were required. Using three experimental targets (Ge, Xe, and Ar), we have illustrated the advantage of target complementarity. Although in general, the right model cannot be fully determined due to the limitations of experimental data, analyses like this one can be used to assess the suitability of future experimental targets.

In conclusion, RAPIDD is well suited to perform fast and accurate scans in a large number of dimensions. It is therefore ideal to explore the wide parameter space of effective field theory operators and could be used by experimental collaborations for a quick interpretation of their results. RAPIDD can also be used in scans that require a large number of evaluations, such as in global scans of particle physics models.

Chapter 5

Improving the Reach of Direct Detection

The tools developed in the previous chapter are ideal to test the performance of future detectors and thus optimise them during the design phase. In this chapter we review Ref. [2], where we investigated the benefits of increasing the maximum nuclear recoil energy analysed in DM direct detection experiments. We extend the energy region of interest (ROI) and show improvements in sensitivity and parameter reconstruction, particular for determining the DM mass. We see that the optimal values of the maximum energy for xenon and argon are of the order of 500 keV and 300 keV, respectively. With this improved set up we return to three-dimensional parameter reconstructions and apply it to the specific case of scalar DM and anapole DM. We find that opening the energy ROI is an excellent way to identify the linear combination of momentum-dependent and momentum-independent operators, and it is crucial to correctly distinguish these models and could well improve the results seen in Chapter 4. Finally, we show how an enlarged energy ROI also allows us to test astrophysical parameters of the DM halo, such as the DM escape speed.

In order to optimise the discovery potential of current and future detectors, one must have an excellent control over the experimental background, either by reducing it through the use of shielding and employing extremely radiopure materials or by understanding any source of irreducible background. Likewise, the characteristics of the expected signature from DM interactions must be well known, as this defines the region of interest in which a signal might be expected.

As we showed in Chapter 2 the velocity and momentum-independent spin-independent (SI) and spin-dependent (SD) operators, are often considered to interpret results from direct detection experiments and derive bounds on the DM-nucleon scattering cross section. For these operators, the expected nuclear recoil spectrum is approximately exponential, with most of the signal concentrated in the keV and sub-keV region and a slope that decreases with increasing DM mass. Thus, in order to capture most of the DM signal, a great effort is made in lowering the experimental energy threshold. This also helps probing lighter DM particles, which leave a smaller energy deposit in the detector.

However, as seen previously the shape of the DM spectrum changes substantially for other EFT operators, mainly for those with a non-trivial momentum dependence, which display a characteristic bump at large recoil energies [116]. Likewise, the higher end of the recoil spectrum is particularly sensitive to some of the astrophysical parameters, as seen in Chapter 3. All of this motivates widening the energy window analysed in direct detection experiments.

The possibility of extending the energy range of direct detection to include the high energy end of the recoil spectrum has been addressed in the literature. Earlier work in this area [245–248] studied inelastic and exothermic DM [246, 248, 249], and more recent works have pointed out the effects on EFT operators for elastic scattering [152, 171, 250]. The prospects of reconstructing the DM speed distribution

and particle physics parameters from direct detection data for an extended energy window up to 1 MeV has also been studied in ref. [251] for the canonical SI cross section.

In this chapter, we will study in detail the advantages of extending the energy window, with emphasis on xenon and argon based detectors. We consider large values for the maximum nuclear recoil energy, and study the optimal energy ranges for xenon and argon to maximise the sensitivity to EFT operators. Then, assuming a DM detection, we investigate how an extended energy range improves the reconstruction of DM parameters (mass and couplings), incorporating the effect of nuclear form factors and the neutrino floor in this energy range. We also extend our study to investigate how a larger energy range can give us access to some astrophysical parameters of the DM halo.

This chapter is organised as follows. In Section 5.1, we discuss what the experimental prospects are for going to higher energies. In Section 5.2, we explain the various aspects of DM detection that would benefit from an increase in the maximum energy, thereby utilizing a larger part of the overall spectrum. This will lead to a significant improvement in the exclusion limits for momentum-dependent EFT operators, a better reconstruction of the DM mass and couplings, and a better sensitivity to astrophysical parameters such as the escape speed. Finally, our conclusions are presented in Section 5.3.

5.1 Energy Region of Interest in direct detection experiments

The region of interest (ROI), defined as the range between the minimum (threshold) energy, E_R^{\min} , and a maximum energy E_R^{\max} , is normally chosen to maximise the potential for DM discovery while keeping the background under control. For simplicity, in this chapter we continue to assume $\varepsilon(E_R) = 1$. Furthermore, in this chapter, until explicitly stated, we will assume the SHM for the local DM distribution with parameters given in Table 5.2, when we consider an alternative halo model motivated by recent hydrodynamic simulations.

In Chapter 4 we saw that momentum-dependent operators can arise via simplified models. However, here we return to the case of the only dimension six operator that interacts with the electromagnetic field for Majorana particles [67]. This is the anapole DM interaction introduced in Chapter 2 and defined by the interaction Lagrangian $\mathcal{L}_{\text{int}} = \mathcal{A} \bar{\chi} \gamma^\mu \gamma^5 \chi \partial_\nu F^{\mu\nu}$. We saw explicitly that in the non-relativistic limit, the effective operator for anapole interactions, \mathcal{O}_A , is a linear combination of the momentum-independent operator \mathcal{O}_8 and the momentum-dependent \mathcal{O}_9 with the Lagrangian as follows [133, 140, 177],

$$\mathcal{L}_A = \sum_{N=p,n} \mathcal{A} e(2Q_N \mathcal{O}_8 - g_N \mathcal{O}_9) \chi^+ \chi N^+ N, \quad (5.1)$$

where e is the electron charge, Q_N is the nucleon charge, and g_N are the nucleon g-factors ($g_p = 5.59$ and $g_n = 3.83$). We can parameterize the coupling strength as $\sigma_A = \mathcal{A}^2 \mu_N^2 / \pi$ [140].

In this work, we focus on the effect of higher recoil energies in noble liquid detectors which employ either liquid xenon or liquid argon. Although the qualitative results can be extrapolated to other targets and experiments, the main advantage is for

heavy DM particles, where noble liquid detectors excel.

The primary DM signature is the spectrum of nuclear recoils reconstructed using the resulting charge and light signals in liquid and double phase noble gas detectors. There are also a series of background sources that limit the experimental sensitivity. These originate either from natural radioactivity, mostly from naturally occurring ^{238}U and ^{232}Th chains, as well as cosmic muon and spallation induced fission products. The dominant backgrounds for many DM searches are neutrons that interact with nuclei in the detector target via elastic scattering. This produces a nuclear recoil similar to the expected signal. High energy cosmogenic neutrons of up to a few GeV might be produced by spallation reactions of cosmic muons on nuclei in the detector or the surrounding rock. Further (α, n) reactions where an α particle can initiate nuclear reactions in the target nucleus while emitting a neutron and spontaneous fission reactions produce neutrons at moderately low energies of around a few MeV. Just as for standard low recoil DM searches, such energy depositions can end up in the region of interest for our searches. Typically the background levels decrease by orders of magnitude from the low energy DM search region of 10 keV to higher energies above 100 keV [252]. Thus searches in the high nuclear recoil energy range can achieve very good sensitivities.

DM is expected to scatter only once in the detector because of its low interaction probability. In contrast most backgrounds are expected to scatter multiple times. Therefore experimentally these backgrounds are identified and rejected by removing multiple scatter events. In the case of high energy nuclear recoils certain instrumental background processes (such as accidental coincidence between single-electron and single-photon noise) might become relatively more important. Another type of instrumental background relevant for the high nuclear energy regime occurs when one of the multiple scatters takes place outside of the sensitive volume and the other one inside the sensitive volume. Then the multiple scatter is mis-characterized as

single-scatter and also its charge yield is not properly reconstructed. These effects are highly dependent on detector geometry and cannot be generally assessed here.

When reconstructing the energy of an incoming particle from the measured light and charge yields, calibration data is necessary. Current noble liquid detectors have developed a comprehensive understanding of backgrounds and calibrations for low recoil energies. If the energy ROI is to be widened, these studies have to be extended as well. The energy scale is determined either directly by using mono-energetic neutron sources or by comparing measured neutron energy with simulations. While the former method is more robust, only a fairly small amount of possible neutron sources can be used. Monte Carlo simulations can be used over a wider energy range, but they require additional assumptions and have large uncertainties. Currently energies only up to about 76 keV nuclear recoil energy are calibrated, although with good accuracy [253].

Presently the highest energy calibrations performed are using D–D neutron generators, providing neutrons of about 2.5 MeV, thus leading to maximal recoils in liquid xenon of about 76 keV [253]. D–T neutron generators could provide much higher energies, up to about 14.1 MeV, enabling the calibration of nuclear recoils up to an energy of approximately 430 keV in a xenon detector which is very well suited to the extended search window which we propose in this work. Argon, because of its lower atomic mass, can use the same sources to calibrate recoils of about 230 and 1300 keV, respectively [254].

In this analysis, we consider two simplified xenon and argon experimental setups, shown in table 5.1, which are motivated by future detectors such as LZ, XENONnT, PandaX, and DARWIN [104, 112, 231, 232] (for Xe), as well as DarkSide and DEAP [112, 114] (for Ar). For each of these setups, we have adopted two configurations: a *nominal* range for the energy ROI, based on current specifications, and an *extended*

Target	Exposure [ton yr]	Nominal ROI [keV]	Extended ROI [keV]
Xe	15.3	3 – 30	3 – 500
Ar	20	5 – 50	5 – 300

Table 5.1: Specifications of the xenon and argon experiments considered in this work inspired by future LZ [232] and DarkSide [112] experiments, respectively.

ROI motivated by the possible improvements in calibrating/reducing the high energy background, as explained in the previous section.

Notice that when considering nuclear recoils at high energies, such approximate nuclear responses can be subject to uncertainties [255]. There are also chiral effective theory effects which can induce corrections to the recoil spectra due to inter-nucleon interactions mediated by meson exchange [256, 257]. These can, in turn, alter the shape of the nuclear responses [125]. We have not included these uncertainties in our analysis. On the one hand, they would not alter the end point of the nuclear recoil spectrum as this only depends on kinematics. On the other hand, the changes in the shape can be relevant for momentum-dependent operators. Determining how much these uncertainties translate into uncertainties on the exclusion limits or parameter reconstruction is beyond the scope of this work. Nonetheless, this work can be seen as a motivation to better understand such uncertainties.

Opening the energy ROI could also improve searches for inelastic scattering where the target nucleus becomes excited. Inelastic scattering has been studied before for a xenon target, since the low-lying excitations of ^{129}Xe (39.6 keV) and ^{131}Xe (80.2 keV) are within the nominal ROI [258, 259]. More nuclear transitions could be accessible with an increased ROI, for example, the first excitation of ^{132}Xe (668 keV), which has a large isotopic abundance. However, at these energies, only the high speed tail of the local DM velocity distribution would be probed, weakening the strength of the signal. The de-excitation of the nucleus would produce a photon, requiring a dedicated search strategy in direct detection. The ^{129}Xe and ^{131}Xe transitions are

produced by a change in nuclear spin, constraining the type of interactions producing them. State-of-the-art calculations for such transitions exist for the axial-vector current $(\bar{\chi}\gamma^\mu\gamma^5\chi)(\bar{q}\gamma^\mu\gamma^5q)$ [260, 261], which refers to the spin-dependent interaction (\mathcal{O}_4). Some of the interactions we consider in this work would be able to excite the xenon isotopes, however a calculation of the form factor for this transition is beyond the scope of this study. Inelastic scattering is in general sub-dominant [259], but studying this signal could be important for improving parameter reconstruction.

5.2 Benefits of enlarging the energy window

In this section we provide concrete examples that illustrate the advantages of enlarging the energy window in the search for DM signals. We will address the effect that a wider ROI has on deriving exclusion limits for EFT operators if no DM signal is found, on the reconstruction of DM parameters in the event of a positive signal, and on gaining sensitivity to the astrophysical parameters describing the DM halo.

Exclusion limits

The first advantage of increasing the energy range in direct detection data analysis is to obtain better upper bounds on the DM-nucleus cross section, if no excess over the background is found. This argument strongly relies on the expected recoil spectrum from DM interactions and therefore it varies significantly for different EFT operators.

In particular, for the canonical SI and SD (\mathcal{O}_1 and \mathcal{O}_4 , respectively) the nuclear recoil spectrum has an approximate exponential behaviour as a function of the recoil energy. A similar behaviour is observed for those EFT operators without an

explicit momentum dependence, namely $\mathcal{O}_{7,8,12}$, although the different form factors induce some variation. In general, if DM interactions are dominated by any of these operators one would expect that most of the DM signal is concentrated at low energies, and thus the usual strategy of lowering the energy threshold to enlarge the ROI would be optimal. On the other hand, the recoil spectrum for operators with an explicit momentum dependence exhibit a characteristic peak at high energies, and vanish when $E_R \rightarrow 0$. The position of this peak is shifted to higher energies as the mass of the DM particle increases. The structure of the nuclear form factors at high energy can also induce further features in the recoil spectrum. Recalling table 2.1, this applies to the vast majority of EFT operators $\mathcal{O}_{3,5,6,9,10,11,13,14,15}$. As we saw in Chapter 4, \mathcal{O}_6 depends quadratically on the transferred momentum, and has a very unique spectral shape. For these operators, it is possible that a significant part of the signal lies at large recoil energies and could be missed if the analysis window is not large enough [152, 250].

To illustrate the discussion above, in Figure 5.1 we compare the recoil spectrum of a typical q -independent operator (\mathcal{O}_1) with that of a q -dependent operator (\mathcal{O}_{10}), and a q^2 -dependent operator (\mathcal{O}_6), as they would be observed in a xenon detector. We also include the non-trivial example of an anapole interaction, which involves a linear combination of operators \mathcal{O}_8 and \mathcal{O}_9 . We display the spectra for three DM masses, $m_\chi = 100, 500, \text{ and } 1000 \text{ GeV}$, and fix the couplings such that each example produces 100 nuclear recoil events in the nominal energy range $[3, 30] \text{ keV}$. The vertical dashed lines represent the maximum energy in the nominal and extended ROI cases, namely $E_R^{\text{max}} = 30 \text{ and } 500 \text{ keV}$, respectively.

Irrespective of the EFT operator, the DM spectrum for elastic scattering displays a maximum energy as a function of the DM escape speed from the Galaxy, v_{esc} , and

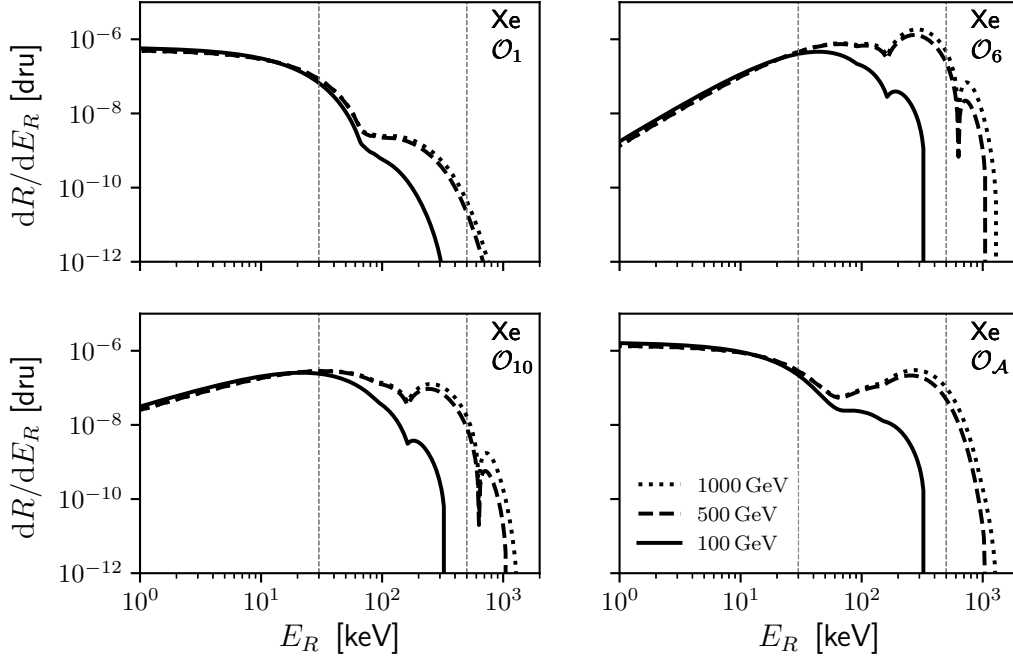


Figure 5.1: The expected recoil spectrum for EFT operators, \mathcal{O}_1 (top left panel), \mathcal{O}_6 (top right panel), \mathcal{O}_{10} (bottom left panel), and for anapole interactions (bottom right panel) in a xenon experiment. The DM mass is chosen to be $m_\chi = 100$ GeV (solid), 500 GeV (dashed), and 1000 GeV (dotted). The vertical dashed lines represent $E_R^{\max} = 30$ keV and 500 keV. The coupling for each operator has been fixed to produce 100 events in the energy range $[3, 30]$ keV.

the DM and target nucleus masses,

$$E_R^{\text{end}} = 2 \frac{m_\chi^2 m_N}{(m_\chi + m_N)^2} v_{\text{esc}}^2. \quad (5.2)$$

For large DM masses, the maximum energy is a function of the target mass, $E_R^{\text{end}} \approx 2m_N v_{\text{esc}}^2$. Using the SHM parameters, we obtain $E_R^{\text{end}} \approx 1600$ keV for a xenon target and $E_R^{\text{end}} \approx 500$ keV for an argon target.

As we can observe, if E_R^{\max} is increased, a significant part of the DM signal for momentum-dependent operators can be accessed, especially for heavy DM particles, with a more substantial improvement for \mathcal{O}_6 . In the case of anapole interactions, an enlarged energy range would allow us to probe the region where the momentum-independent \mathcal{O}_8 dominates over the momentum-dependent \mathcal{O}_9 (which displays a

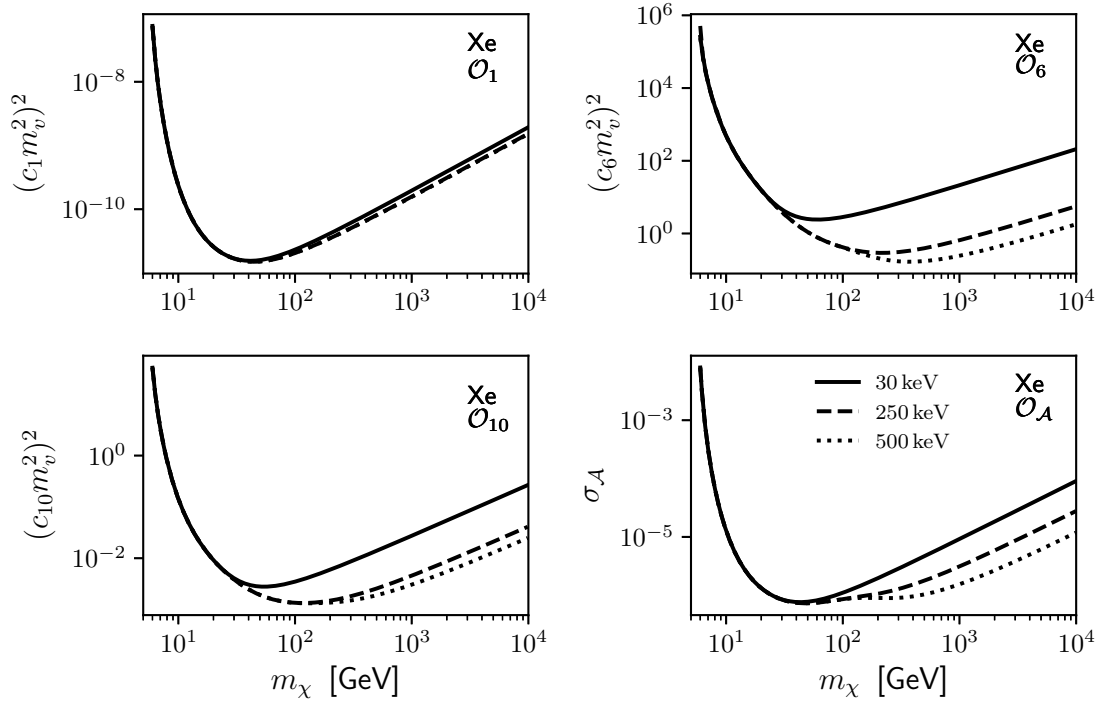


Figure 5.2: Projected exclusion limits for a xenon detector for EFT operators, \mathcal{O}_1 , \mathcal{O}_6 , \mathcal{O}_{10} , and for anapole interactions. The solid, dashed, and dotted lines correspond to $E_R^{\max} = 30, 250$ and 500 keV, respectively.

bump at large energies).

In Figure 5.2 we present the upper limits at 90% confidence level on the c_1^2 , c_6^2 , and c_{10}^2 coefficients, as well as on the coupling of the anapole moment \mathcal{A} , assuming no DM signal in a xenon detector with an exposure of 15.3 ton yr (as given in table 5.1). The solid, dashed, and dotted lines show the results for $E_R^{\max} = 30, 250$ and 500 keV, respectively. As we can observe, the improvement for momentum-independent operators (such as \mathcal{O}_1) is negligible, whereas momentum-dependent operators greatly benefit from the increased energy range. In the case of \mathcal{O}_6 , the exclusion limit can improve by more than one order of magnitude for DM masses above $m_\chi \approx 300$ GeV.

We have explicitly checked that in the case of a xenon detector, the improvement in the exclusion limits that one obtains when E_R^{\max} increases from 500 keV to 1600 keV

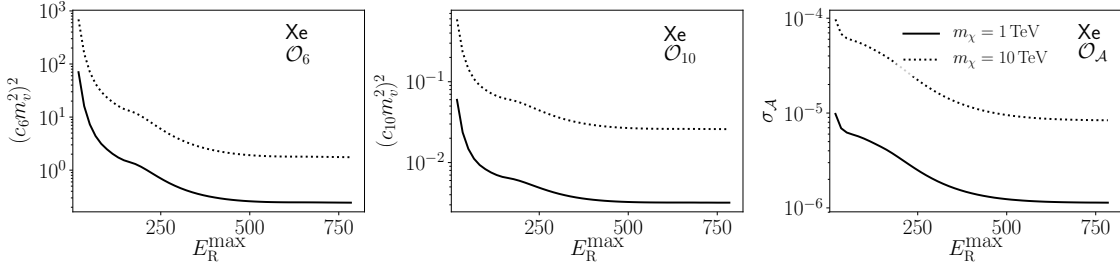


Figure 5.3: The sensitivity of Xenon experiments as a function of the E_R^{\max} in the experiment. We show the results for two heavy DM particles $m_\chi = 1$ TeV (solid) and $m_\chi = 10$ TeV (dashed).

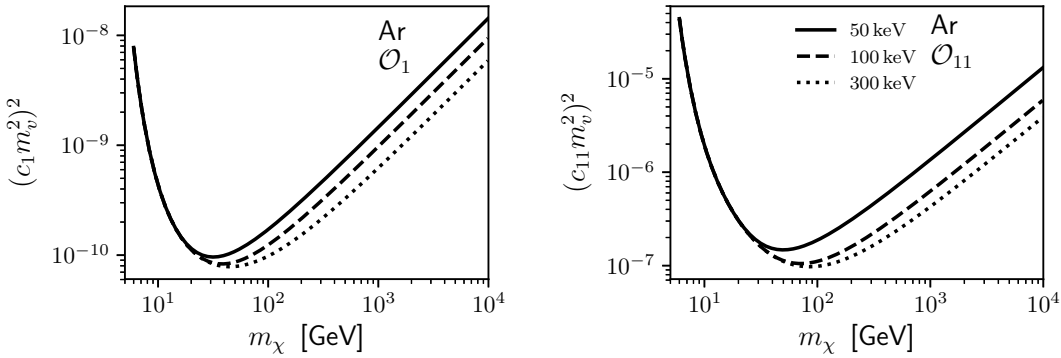


Figure 5.4: Projected exclusion limits for an argon detector for EFT operators, \mathcal{O}_1 and \mathcal{O}_{11} . The solid, dashed, and dotted lines correspond to $E_R^{\max} = 50, 100$ and 300 keV, respectively.

is minimal, and therefore the optimal value of the maximum recoil energy is $E_R^{\max} \approx 500$ keV. In Figure 5.3 how this was determined, where the coupling value the experiment is sensitive to, for exposure in table 5.1 at $m_\chi = 10^4$, is plotted as a function of E_R^{\max} .

We obtain qualitatively similar results for an argon detector. Figure 5.4 shows the exclusion limits obtained for operators \mathcal{O}_1 and the q -dependent \mathcal{O}_{11} . Notice that argon is insensitive to \mathcal{O}_6 and \mathcal{O}_{10} . We present the results for $E_R^{\max} = 50, 100$, and 300 keV. Once again, the improvement in momentum-independent operators is marginal, but the sensitivity for momentum-dependent ones is greatly enhanced. The improvement for higher values of E_R^{\max} is minimal and hence the optimal value of the maximum energy for an argon detector is $E_R^{\max} \approx 300$ keV.

We have checked that the results for other momentum-dependent operators are qualitatively similar to those of \mathcal{O}_{10} , with small differences that can be attributed to the corresponding form factors.

Dark matter parameter reconstruction

In this section we will examine how increasing E_R^{\max} effects the inference of the mass and couplings of the DM particle from the nuclear recoil spectrum as discussed in Chapter 3 and Refs. [157–159]. From the discussion in the previous section, we can imagine that an increased energy range in the analysis window would lead to a better measurement of the recoil spectrum and, consequently, to a better measurement of the DM parameters.

In particular, the endpoint of the nuclear recoil spectrum, E_R^{end} (see eq. 5.2), provides a good measurement of the DM mass, irrespective of the EFT operator. This complements other information that can be obtained from the spectral shape.

As we can observe in Figure 5.1, the endpoint for a 100 GeV DM particle is above the canonical energy window considered in xenon experiments, but could be observed with a larger E_R^{\max} . Notice that in the limit of very heavy DM particles, the endpoint is only a function of the target mass and therefore the capability of reconstruction is eventually lost.

We have chosen a set of representative benchmark points and use eq. (2.1) to compute the simulated spectrum, N_k^{obs} , which we take as the *observed* event rate. We explore the DM parameter space and for each point, $\lambda = \{m_\chi, c_i\}$, in the DM mass and EFT coupling plane, we compute the expected number of DM events in a given energy bin, $N_k(\lambda)$. We then construct the same binned likelihood as in Chapters

3 (Eq.3.2). We assume here a bin width of 1 keV in the nominal ROIs. For the extended ROIs we increase the bin size to 50 keV in xenon and 10 keV in argon¹. In order to calculate the profile likelihood and to effectively scan the parameter space, we use MultiNest [228]. The confidence intervals in the parameter space are then extracted using Superplot [180]. To speed up the computation of the number of DM events in the EFT framework, we use the surrogate model RAPIDD [1].

In order to quantify the improvement in the DM mass reconstruction when the energy range is extended, we simulate a future DM excess, assuming a given EFT operator and DM mass. Then we attempt to reconstruct it using the binned likelihood defined in eq. (3.2). By construction, the best fit point coincides with the simulated DM mass, but we also determine the 1σ confidence interval of the reconstructed masses, $(m_{1\sigma}^-, m_{1\sigma}^+)$, from which we define

$$\Delta_m = \left(\frac{m_{1\sigma}^-}{m_\chi}, \frac{m_{1\sigma}^+}{m_\chi} \right). \quad (5.3)$$

Where the true value is at $\Delta_m = 1$ and $\Delta_m \in [0, \infty]$. For concreteness, we will consider benchmark points that predict observation of 100 DM-induced nuclear recoil events in the nominal ROI.

Figure 5.5 shows the resulting Δ_m as a function of the DM mass for a reconstruction using 100 events for each value of the DM mass. From the left to right panels, we present the results for EFT operators \mathcal{O}_1 , \mathcal{O}_6 , and \mathcal{O}_{11} . The different coloured areas correspond to different energy ROIs, with $E_R^{\max} = 30, 250, \text{ and } 500$ keV.

Let us first concentrate on the canonical spin-independent operator \mathcal{O}_1 . For the nominal ROI, with $E_R^{\max} = 30$ keV the 1σ region is unbounded from above for DM masses above 60 GeV, something we observed with the results for BP2 in our sim-

¹Lacking information about energy calibration in the extended ROI, we have decided to take a conservative approach and increase the bin size. A smaller bin size could in principle lead to a better parameter reconstruction.

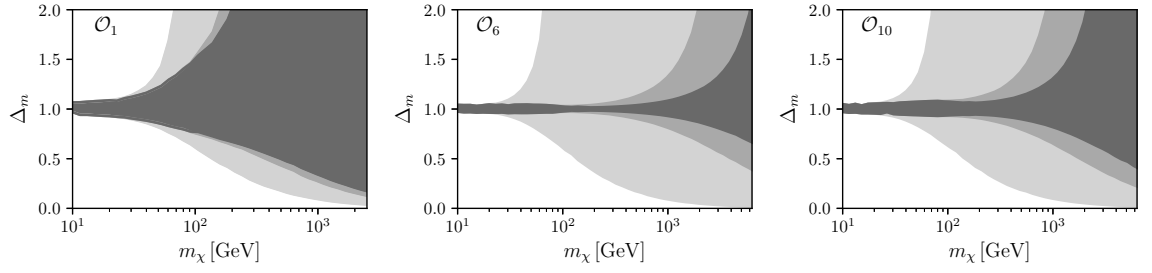


Figure 5.5: Mass reconstruction parameter, Δ_m (defined in eq. 5.3), as a function of the DM mass for operators \mathcal{O}_1 , \mathcal{O}_6 , and \mathcal{O}_{10} from the left to right panels in a xenon detector. We have assumed a benchmark point, for each value of the DM mass, that produces 100 nuclear recoil events. The light to dark grey regions correspond to different energy ROIs, with $E_R^{\max} = 30, 250, 500$ keV, respectively.

plified model example in Chapter 4. As E_R^{\max} increases, larger DM masses can be accessed and with $E_R^{\max} = 250$ keV one can successfully reconstruct DM masses up to 100 GeV. Meaning perhaps, in the case study of Chapter 4, we could have differentiated between scalar and vector mediated particle models. The optimal energy range of $E_R^{\max} = 500$ keV would allow us to reconstruct DM masses up to just 200 GeV. For any DM mass above this value, there is no upper bound in the reconstructed value. Interestingly, the lower limit of the reconstruction also benefits from a larger E_R^{\max} . It should also be noted that the relative improvement in reconstruction from having a maximum energy above 500 keV is minimal. The reconstruction for 100 nuclear recoil events shows that the limitation in the reconstruction of DM masses is not due to poor statistics. Indeed, even with a larger number of events, there is no proper DM mass reconstruction for \mathcal{O}_1 above $m_\chi \sim 200$ GeV.

The benefit of enlarging the energy ROI is more pronounced for momentum-dependent operators, such as \mathcal{O}_6 and \mathcal{O}_{10} . In both cases, increasing E_R^{\max} leads to a much better DM mass reconstruction, where DM masses as heavy as $m_\chi \sim 2$ TeV can be resolved. This is in contrast with the nominal ROI, which only allows reconstruction up to $m_\chi \sim 60$ GeV. It should be noted that even when the upper limit of the reconstructed mass becomes unbounded ($\Delta_m \rightarrow \infty$) the lower limit can still improve substantially

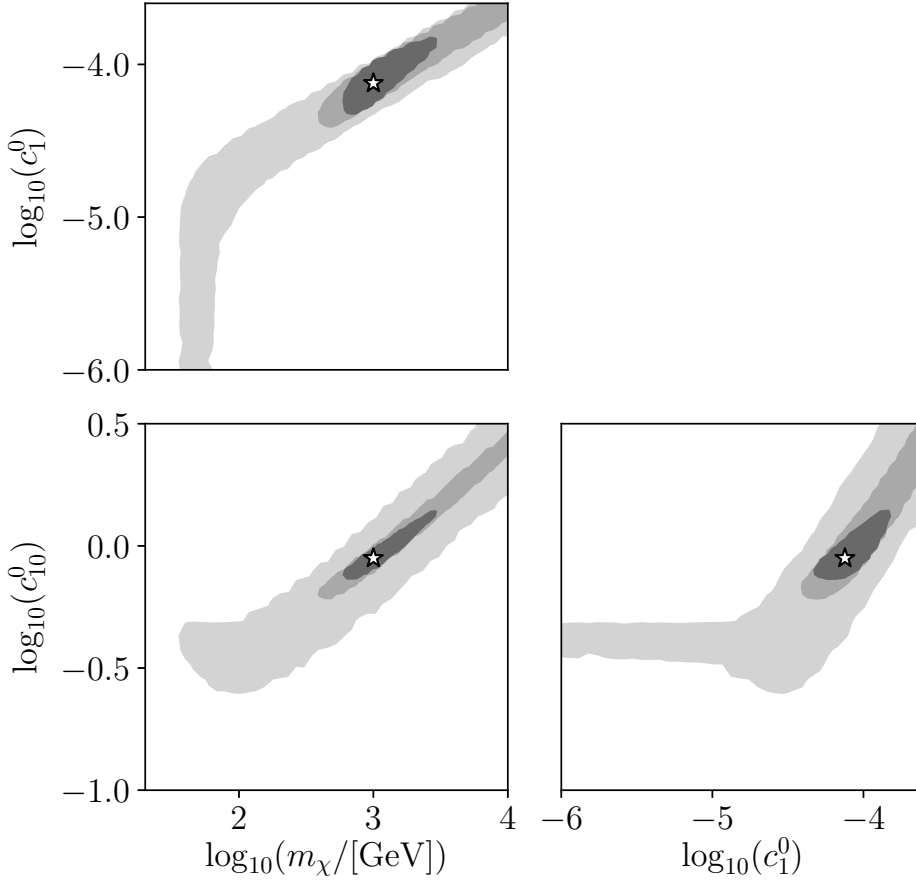


Figure 5.6: Results from a 3D parameter scan, fitting mock data from our benchmark point with mass $m_\chi = 1$ TeV and a coupling to \mathcal{O}_1 and \mathcal{O}_{10} which produces 100 counts in the $[3, 30]$ keV window. The 2σ countours are shown from light gray to dark gray for $E_R^{\text{max}} = 30, 250$ and 500 keV, respectively. The white star represents the benchmark point.

if E_R^{max} is further increased.

Having a good reconstruction of the DM mass also helps in measuring the DM couplings and removing degeneracies in the parameter space. We illustrate this with an example, motivated by the case of scalar DM with a scalar mediator, in which the parameter space is three-dimensional and consists of the DM mass and operators \mathcal{O}_1 and \mathcal{O}_{10} . We have selected a benchmark point with $m_\chi = 1$ TeV and equal contributions from \mathcal{O}_1 and \mathcal{O}_{10} that give 100 counts in the usual $[3, 30]$ keV energy window. This benchmark point is special because, as we saw in the discussion above, m_χ values can be bounded from above in the extended energy ROI. Figure 5.6

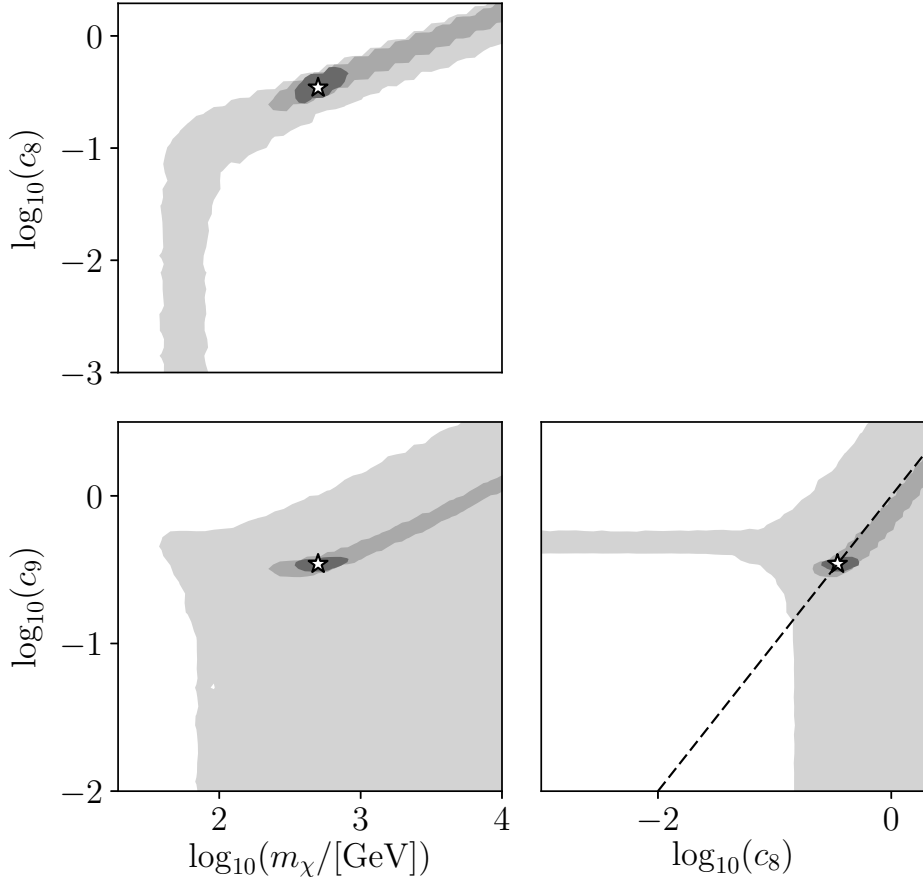


Figure 5.7: Same as figure 5.6 but for $m_\chi = 500$ GeV and a coupling via the anapole moment. The black dashed line in the (c_9, c_8) plane represents the relation among these couplings in an anapole DM model.

represents the 2σ reconstructed region in the 3D parameter space $(m_\chi, c_1^0, c_{10}^0)$ for the three choices $E_R^{\text{max}} = 30, 250, \text{ and } 500$ keV. As we can observe, the nominal ROI is insufficient to determine any of the three parameters and large degeneracies are observed in the three planes.

For example, the data can be consistent with light DM that interacts mainly through \mathcal{O}_{10} or with heavier DM and a linear combination of \mathcal{O}_1 and \mathcal{O}_{10} . When the energy ROI is extended, the light DM solution disappears and eventually, with $E_R^{\text{max}} = 500$ keV, a full reconstruction of the three parameters is possible.

As a second example, we have selected a benchmark point that corresponds to

anapole DM, with $m_\chi = 500$ GeV and $c_8 = c_8^p = 2\mathcal{A}e$, $c_8^n = 0$, $c_9 = c_8 = -(2/g_p)c_9^p = -(2/g_n)c_9^n$. For simplicity we have already imposed the correct relation among the couplings to protons and neutrons and we have attempted to reconstruct the DM parameters in the 3D plane (m_χ, c_8, c_9) . The results are shown in Figure 5.7, and in the (c_8, c_9) plane we indicate the anapole relation between both couplings by means of a dashed black line. As in the previous example, the results with the nominal ROI are not sufficient to provide a good measurement of any of the parameters and large degeneracies are visible. For $E_R^{\max} = 250$ keV, the region with low DM mass and a leading \mathcal{O}_9 contribution disappears and although there is still a residual degeneracy in the (c_8, c_9) plane, the results already reproduce the anapole relation along the dashed line. Notice that, from the spectrum in the bottom right panel of Figure 5.1, we can see that this energy is enough to observe the characteristic shape of \mathcal{O}_9 but it is insufficient to measure the end point of the spectrum. With the extended ROI ($E_R^{\max} = 500$ keV), a good measurement is obtained for the three parameters. Without enlarging the energy ROI, it would be impossible to properly identify this scenario as anapole DM.

Astrophysical uncertainties

In this section we examine whether this experimental setup will improve our understanding about astrophysical uncertainties as introduced in Chapter 3. In an attempt to conduct a more refined analysis, we have opted to consider self consistent halos as opposed to treating all astrophysical parameters as nuisance parameters as in Chapter 4.

The way we obtained internally consistent velocity distributions is to extract them from cosmological simulations. High resolution cosmological simulations including baryonic physics have recently become available and are able to reproduce import-

Parameter	v_{peak} [km s ⁻¹]	v_c [km s ⁻¹]	v_{esc} [km s ⁻¹]	ρ_0 [GeV cm ⁻³]
SHM	220	220	544	0.4
EAGLE	288.64	254.06	874.76	0.68

Table 5.2: The peak speed of the Maxwellian velocity distribution, local circular speed, Galactic escape speed, and the local DM density assumed in the SHM (row 1) and extracted from the simulated MW-like galaxy in the EAGLE simulation farthest from the SHM (row 2).

ant galactic properties with significant agreement with observations. Recently it was shown that the local DM velocity distribution extracted from state-of-the-art hydrodynamic simulations fit a Maxwellian distribution well, but with a peak speed which can be different from the local circular speed [196, 242, 262, 263]. Ref. [196] used the EAGLE and APOSTLE high resolution simulations which include both DM and baryons and identified 14 simulated Milky Way-like galaxies by taking into account observational constraints on the Milky Way. The range of the best fit peak speeds of the Maxwellian distribution for the simulated Milky Way-like galaxies was found to be 223 – 289 km/s. To include in the analysis of direct detection data the largest possible deviation with respect to the SHM predicted by simulations, we will consider the simulated MW-like galaxy in EAGLE/APOSTLE with the local DM velocity distribution furthest from the SHM. The parameters of this halo, along with the fiducial parameters of the SHM are given in table 5.2. For both halo models, we consider the same velocity of the Earth with respect to the Sun and the peculiar velocity of the Sun discussed in Chapter 3 and as given in ref. [196].

For the current recoil energy range probed by direct detection experiments, uncertainties in the high velocity tail of the DM velocity distribution become especially important for light DM masses. This is because for a fixed maximum recoil energy, low DM masses lead to a high minimum DM speed, v_{min} , where the experiments probe the tail of the DM velocity distribution. In particular, the range of the best fit peak speeds for the Maxwellian velocity distribution allowed by hydrodynamic simulations of MW-like galaxies [196, 242] translates into an uncertainty in the allowed regions or exclusion limits set by direct detection experiments, for low mass (10’s

of GeV) DM particles. However, if the maximum recoil energy in an experiment is significantly increased, even larger DM masses (100's of GeV) lead to high v_{\min} , where the experiments become sensitive to the tails of the DM velocity distribution.

In order to disentangle astrophysical uncertainties, one has to consider results from multiple targets. As discussed extensively in the literature, this complementarity will also help with particle parameter reconstruction [163–167, 264]. Hence, we will once again consider future Xe and Ar detectors. To determine whether increasing the energy window will help us overcome astrophysical uncertainties for large DM masses, we produce a series of data resulting in 100 and 1000 counts in the two detector configurations given in table 5.1, for a 100 GeV DM, and arising from the two halo models (SHM and EAGLE) we are considering, which we take as the *true* halo model. We then perform a parameter reconstruction for each experiment separately, assuming the SHM for both cases. If one was to observe some tension between the two experiments, it would suggest that the assumption of the SHM is incorrect.

Figure 5.8 shows the profile likelihood for the reconstruction of DM parameters for a 100 GeV benchmark point that produces 100 counts in our Xe (red) and Ar (blue) detector configurations using the *nominal* (top row) and *extended* (bottom row) ROIs given in table 5.1, for a coupling to \mathcal{O}_1 . It is clear from Figure 5.8 that by opening the energy window for both experiments, we achieve stronger constraints on the coupling and DM mass and this in turn can put tension between the two experiments for the EAGLE halo model. However, we see that with 100 counts this tension is not very strong, and it would be difficult to rule out the SHM at high significance.

There are some general comments to be made. If the halo assumed in the reconstruction of the DM parameters has a v_{esc} below the *true* value, then the spectra will

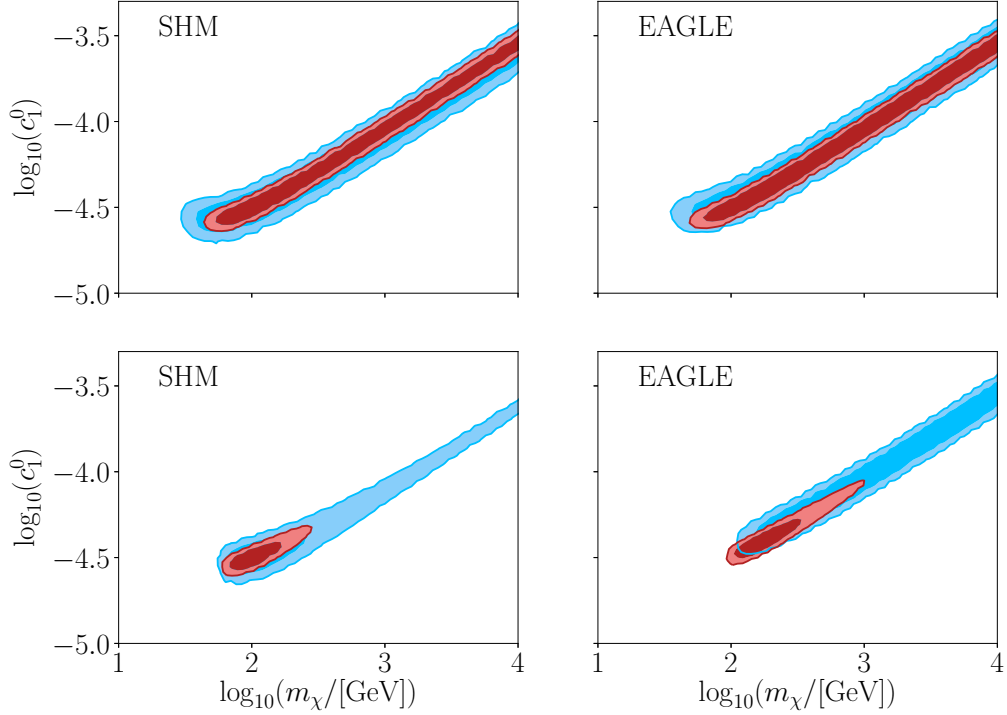


Figure 5.8: Profile likelihoods for the reconstruction of DM parameters for a 100 GeV DM benchmark point that produces 100 counts in our future Xe and Ar detector configurations given in table 5.1, for a coupling only to \mathcal{O}_1 . Red and blue shaded regions correspond to 2σ (light shade) and 1σ (dark shade) regions obtained from the individual targets of Xe and Ar, respectively. The top row corresponds to the *nominal* configuration of the experiments assuming an energy window of [3, 30] keV for Xe and [5, 50] keV for Ar. The bottom row corresponds to the *extended* configuration assuming an energy window of [3, 500] keV for Xe and [5, 300] keV for Ar. The left and right panels correspond to the SHM and EAGLE halo models, respectively, which were assumed to generate the data (i.e. the *true* halo model). Every parameter scan has been performed assuming the SHM with values given in table 5.2.

appear to come from a DM particle with a larger m_χ . Notice that the smaller the mass of the target nucleus, the greater the effect. Furthermore, for $m_\chi \gg m_N$, the higher the value of m_χ , the higher is the coupling strength, causing the reconstructed region to move upwards. This can be seen in Figure 5.8, where the reconstructed region for the EAGLE halo which has a larger escape speed compared to the SHM, is shifted to masses larger than 100 GeV. This shift is even larger for the Ar experiment which has a smaller target nucleus mass. These results complement the findings of

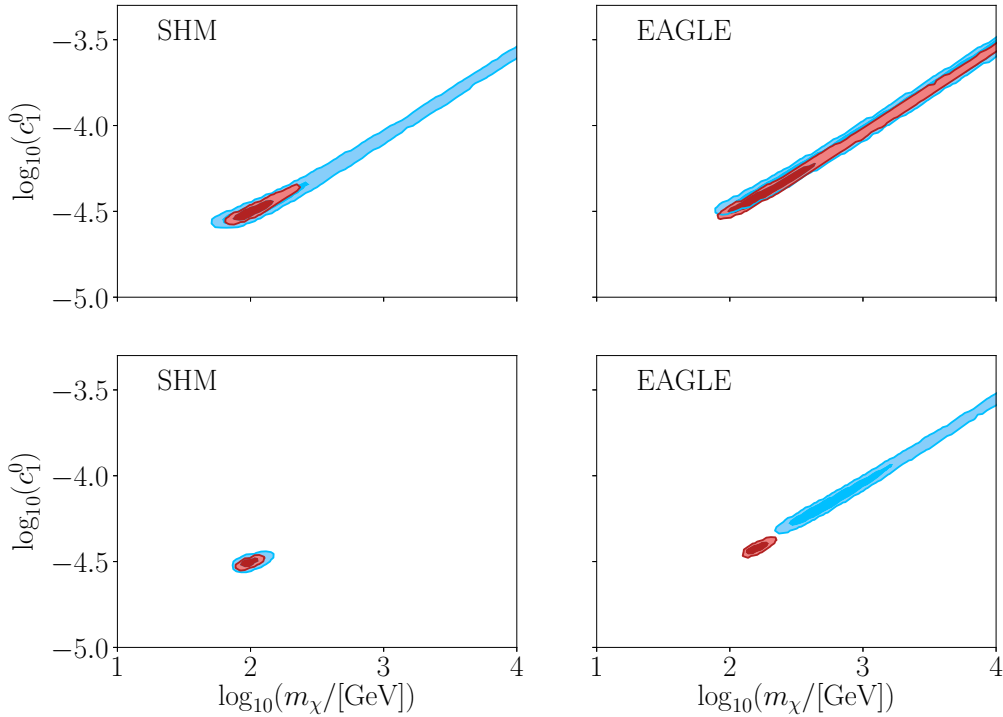


Figure 5.9: Same as figure 5.8, but with an experimental exposure increased by a factor of 10, i.e. a benchmark point that produces 1000 counts.

Ref. [251], where it was found that the reconstructed areas could significantly improve with an extended analysis window. Our results strengthen the complementary role between xenon and argon targets for the study of large mass DM.

In order to see whether greater statistics would improve our ability to distinguish between different halos we ran the analysis again but with ten times the original exposure given in table 5.1 for both the Xe and Ar experiments. To do this, we had to include the neutrino floor as a known background into the calculation. Figure 5.9 shows the results for the \mathcal{O}_1 benchmark that produces a 1000 counts. We see that for both halos, the different experiments are completely consistent in the nominal setup. Once we open the energy window we start to have tension between different experiments for the EAGLE halo. In particular, the 2σ regions for the different detectors are completely separated for the EAGLE halo, and hence the SHM could

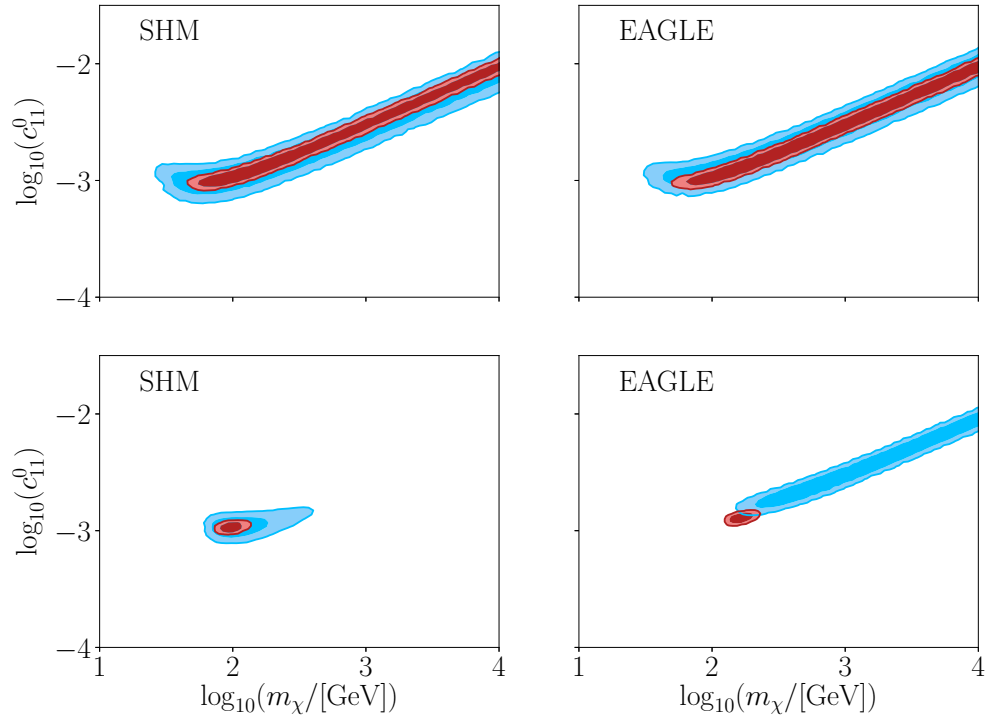


Figure 5.10: Same as figure 5.8 but with a coupling only to operator \mathcal{O}_{11} .

be ruled out in this case.

As an example of an operator with a different behavior with respect to \mathcal{O}_1 , we next consider the \mathcal{O}_{11} operator which exhibits a q -dependence. Figure 5.10 shows the results for coupling to \mathcal{O}_{11} for a 100 GeV benchmark point that produces 100 counts in Xe and Ar. We can see that even with a 100 counts, when the energy window is opened, \mathcal{O}_{11} interactions can cause greater tension between the two experiments for the EAGLE halo, resulting in separated 1σ regions for Xe and Ar.

5.3 Summary

In this chapter based on the article [2], we have investigated the benefits of enlarging the region of interest of the nuclear recoil energy in the analysis of direct DM detection data. In particular, we have studied how increasing the maximum recoil energy, E_R^{\max} , will allow us to extract more information from the tail of the nuclear recoil spectrum. We have concentrated on elastic DM-nucleus scattering and considered an EFT approach to describe the interaction. Focusing on future xenon and argon detectors, we have investigated the implications that a larger E_R^{\max} has on setting limits on DM couplings, on measuring the DM parameters, and on obtaining information about the astrophysical parameters of the DM halo.

In agreement with previous studies, we find that a larger E_R^{\max} would lead to more stringent upper bounds on the DM-nucleus cross section, especially for momentum-dependent operators. For example, in xenon experiments, the sensitivity to \mathcal{O}_6 and \mathcal{O}_{10} can increase by approximately an order of magnitude for DM masses above approximately 300 GeV, and in argon a similar improvement can be achieved for \mathcal{O}_{11} . We have determined that the optimal values of the maximum energy are $E_R^{\max} \approx 500$ keV for xenon and $E_R^{\max} \approx 300$ keV for argon. This would require a good knowledge of the experimental background at those energies, as well as proper calibration (that could be achieved using a D–T source).

We have also studied how well the mass and couplings of the DM particle could be reconstructed from future data if an excess over the background is observed. We point out that a larger E_R^{\max} would allow for a much better measurement of the DM mass, mainly from the observation of the end-point of the nuclear recoil spectrum. For momentum-independent operators, the improvement is modest. For example, in the case of \mathcal{O}_1 the extended ROI allows to reconstruct DM masses up to approximately 200 GeV. However, the improvement for momentum-dependent

operators is much more impressive. For example, for operator \mathcal{O}_6 DM masses as large as 2 TeV can be reconstructed with an extended ROI.

Furthermore, we showed how this improvement can translate to three-dimensional parameter reconstruction, concentrating on two examples: scalar DM with scalar mediator, and anapole DM. Our results show that opening the energy ROI is an excellent way to identify the linear combination of momentum-dependent and momentum-independent operators. This is crucial to distinguish different DM models in the range of heavy DM masses.

Finally, we have shown that an extended energy ROI can also be used to test astrophysical parameters of the DM halo, such as the DM escape speed. In a series of examples, we have simulated direct detection data using two different halo models and attempted to reconstruct the DM couplings and mass using the Standard Halo Model. We have observed that an extended ROI and target complementarity can help in identifying when the wrong hypothesis is used in the data analysis.

Chapter 6

Potential hints of Dark Matter from Flavour Anomalies

6.1 Introduction

So far we have explored solely direct detection and how to optimise the discovery potential as well as discrimination power of the experiments. In this chapter however, we present a study of a specific DM model, motivated by potential anomalies found in studies of meson decays as mentioned in Chapter 1. Once a specific model has been chosen, it becomes an imperative to show that it does in fact provide a candidate for DM, i.e. that it is created to the correct abundance (outlined in Chapter 1), and that it is not already excluded by current experimental bounds.

The specific processes that motivate the model in this chapter are B meson decays. The rates of which have been reported as anomalous by the LHCb, hinting at the possibility of lepton flavour universality violation [265, 266]. The SM predicts equal

rates for the processes $B \rightarrow K^{(*)}\mu^+\mu^-$ and $B \rightarrow K^{(*)}e^+e^-$, and it is customary to study the ratios of these branching fractions, defined as $R(K)$ and $R(K^*)$, since the dependencies on hadronic matrix elements (and associated uncertainties) cancel out [267]. The measurements of these hadronically clean observables deviate consistently (although perhaps with not enough statistical significance) from the SM prediction $R(K^{(*)}) = 1$ [268]. These hints are complemented by measurements of other observables that are more sensitive to hadronic physics. In particular, the differential branching fractions [265, 266, 269] and angular observables [270–277] associated to the processes $B \rightarrow \phi\mu^+\mu^-$ and $B \rightarrow K^{(*)}\mu^+\mu^-$ also deviate from the SM predictions. Interestingly, all the apparent anomalies involve the transition $b \rightarrow s\mu^+\mu^-$.

In order to account for these experimental results, one can modify the SM effective Hamiltonian, which involves penguin and box diagrams, by including one-loop contributions from new exotic particles. A full classification of the various particle combinations, considering different gauge representations, was presented in Refs. [278, 279]. Among the different models, some featured neutral scalar or fermions that, if stable, could play the role of dark matter (DM)¹. The first possibility was investigated in Ref. [305], where it was found that the large new couplings required to reproduce the correct DM relic abundance induce sizeable 1-loop contributions to DM-nucleon scattering, leading to very strong limits from direct detection experiments. In addition, as reported by [306], the Higgs portal coupling typically dominates over other new physics effects. The second possibility was addressed in Ref. [307], where the fermionic dark matter field was accompanied by one additional scalar and one additional coloured fermion.

¹An alternative to this one-loop solution is to consider Z' [280, 281] or leptoquark [282, 283] tree-level contributions, see e.g., Ref. [284] and references therein. The DM problem has been addressed in the framework of these constructions [285], see e.g., Refs. [286–300] for the Z' , and Refs. [301–304] for the leptoquark models.

In this work, we consider a modification of the model of Ref. [307]. Namely, we will also assume a fermionic dark matter particle, but with two extra scalar fields, one of which has a colour charge. On top of this, we include the latest SM theoretical prediction for the mass difference in B_s -mixing [308], which differs from the experimental observation by 1.8σ . In order to reduce this tension and provide an explanation for the B anomalies, complex couplings are needed, leading to new CP-violation sources, a scenario that has not been studied in the context of one-loop models so far. We explore the parameter space of this model, taking into account all the flavour observables, DM constraints, and LHC collider signatures.

In Section 6.2, we introduce the details of the particle physics model, address the constraints from the observed DM relic abundance and B_s -mixing and discuss the implications on the model's parameter space. In Section 6.3, we compute the DM-nucleus scattering cross section and study current constraints and the future reach of direct DM detection experiments. Finally, in Section 6.4, we investigate the possibility of observing this scenario at the LHC, for which we take into account dijet and dimuon searches. We also include a projection of the potential reach of the High Luminosity phase of the LHC. We then combine these results with the direct detection projections and constraints. A summary is presented in Section 6.5.

6.2 Our model

The model considered is one in which the DM particle is a Majorana fermion, χ , with two extra scalar fields, ϕ_q and ϕ_l , which couple to left-handed quarks and leptons, respectively². The interactions between the new particles and the SM are described

²As we will comment in Section 6.3, the alternative construction with Dirac DM is ruled out mainly by experimental results from direct DM detection.

	$SU(3)$	$SU(2)_L$	$U(1)_Y$	\mathcal{Z}_2
ϕ_q	3	2	1/6	-1
ϕ_l	1	2	-1/2	-1
χ	1	1	0	-1

Table 6.1: Quantum numbers of the new fields. We also indicate the charges under \mathcal{Z}_2 .

by the Lagrangian,

$$\mathcal{L}_{\text{int}}^{\text{NP}} = \lambda_{Q_i} \bar{Q}_i \phi_q P_R \chi + \lambda_{L_i} \bar{L}_i \phi_l P_R \chi + \text{h.c.}, \quad (6.1)$$

where Q_i and L_i denote the SM left-handed quark and lepton doublets of each generation, and λ_{Q_i} and λ_{L_i} are the corresponding new couplings. The quantum numbers for the new fields are summarised in Table 6.1. We impose a \mathcal{Z}_2 parity under which the SM fields are invariant, and which guarantees the stability of the DM candidate, as long as $m_{\phi_{q,l}} > m_\chi$. Upon rotation from the electroweak to the quark mass eigenbasis, the couplings λ_{Q_i} are rotated in flavour space. Assuming that the electroweak and mass eigenbasis are aligned for the leptons and down-type quarks, the couplings to the up-type quarks are generated by the CKM rotation as follows:

$$\lambda_{Q_i} \bar{Q}_i \rightarrow \lambda_{Q_j} (\bar{u}_{L,i} V_{ij}, \bar{d}_{L,j}). \quad (6.2)$$

From now on, we will denote the couplings in the mass eigenbasis with the corresponding quark or lepton label. These couplings are, in general, complex.

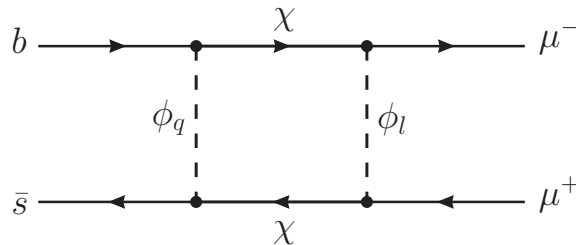


Figure 6.1: One-loop diagram contribution from the new particles to the $b \rightarrow s \mu^+ \mu^-$ transitions.

This model induces new physics contributions to flavour observables at the loop

level. In particular, a new box diagram appears for the $b \rightarrow s\mu^+\mu^-$ transition, as shown in Figure 6.1. These effects can be described using a relativistic effective field theory approach, thus parameterising the new contributions as corrections to the corresponding Wilson coefficients of the effective Hamiltonian,

$$\mathcal{H}_{\text{eff}}^{\mu^+\mu^-} = -\frac{4G_F}{\sqrt{2}}V_{tb}V_{ts}^*(C_9\mathcal{O}_9 + C'_9\mathcal{O}'_9 + C_{10}\mathcal{O}_{10} + C'_{10}\mathcal{O}'_{10}) + \text{h.c.}, \quad (6.3)$$

where the effective operators $\mathcal{O}_9, \mathcal{O}'_9, \mathcal{O}_{10}, \mathcal{O}'_{10}$ are defined as:

$$\mathcal{O}_9 = \frac{\alpha_{\text{em}}}{4\pi}(\bar{s}\gamma^\mu P_L b)(\bar{\mu}\gamma_\mu\mu), \quad (6.4)$$

$$\mathcal{O}'_9 = \frac{\alpha_{\text{em}}}{4\pi}(\bar{s}\gamma^\mu P_R b)(\bar{\mu}\gamma_\mu\mu), \quad (6.5)$$

$$\mathcal{O}_{10} = \frac{\alpha_{\text{em}}}{4\pi}(\bar{s}\gamma^\mu P_L b)(\bar{\mu}\gamma_\mu\gamma_5\mu), \quad (6.6)$$

$$\mathcal{O}'_{10} = \frac{\alpha_{\text{em}}}{4\pi}(\bar{s}\gamma^\mu P_R b)(\bar{\mu}\gamma_\mu\gamma_5\mu). \quad (6.7)$$

The Wilson coefficients $C_9, C'_9, C_{10}, C'_{10}$ contain both the SM and new physics (NP) contributions,

$$\begin{aligned} C_9 &= C_9^{\text{SM}} + C_9^{\text{NP}}, \\ C_{10} &= C_{10}^{\text{SM}} + C_{10}^{\text{NP}}, \end{aligned} \quad (6.8)$$

with the primed coefficients defined in an equivalent way.

Global fits [284, 309–317] have been used to determine the new physics contribution to the Wilson coefficients in order to reproduce the observed experimental results. These fits favour $C_9^{\text{NP}} = -C_{10}^{\text{NP}}$, and suggest that no new physics is required for operators involving electrons or tau leptons. Because of this, we assume negligible couplings to the first quark generation (i.e., $\lambda_{Q_1} = 0$) and to the first and third lepton generations (i.e., $\lambda_e = \lambda_\tau = 0$). This provides an explanation for the $R_{K^{(*)}}$ anomalies, while relaxing the bounds from other searches.

Therefore, in total, we are left with six free parameters in this model, namely the masses of the three new particles ($m_\chi, m_{\phi_l}, m_{\phi_q}$), and the couplings to b -type

quarks, s -type quarks, and leptons $(\lambda_b, \lambda_s, \lambda_\mu)$.

It should be noted that the couplings $\lambda_1|\phi_l|^2|H|^2$ and $\lambda_2|\phi_q|^2|H|^2$ are allowed by gauge symmetry in the Lagrangian of Eq. (6.1). However, they only lead to an overall shift to the masses of ϕ_l and ϕ_q after electroweak symmetry breaking since the couplings to the Higgs play no phenomenological role in the relevant range of $\phi_{l,q}$ masses. Likewise, the terms $\lambda_3|\phi_l H|^2$ and $\lambda_4|\phi_q H|^2$ are also allowed by gauge symmetry. They typically induce a small split in the masses of the neutral and charged components of the doublets ϕ_l and ϕ_q in the range of $\phi_{l,q}$ masses that survive the collider constraints. Finally, a term of the form $(\phi_l H)^2$ can lead to large contributions to neutrino masses at one loop, which forces the corresponding coupling to be extremely small [307]. We will neglect these couplings in the following.

As mentioned above, similar models have been discussed in the literature, featuring either scalar DM [305, 318–320] or fermionic DM [307]. Our model differs from that of Ref. [307] in that we have two extra scalar fields which couple to the lepton or quark sectors.

Dark matter relic abundance and indirect detection constraints

In order for χ to be a viable DM candidate, it must reproduce the observed relic abundance, which can be inferred from Planck satellite data to be $\Omega h^2 = 0.1199 \pm 0.0022$ [34]. The pair-annihilation proceeds through the two t -channel diagrams with ϕ_q and ϕ_l , shown in Figure 6.2, allows for a relic abundance to be realised via thermal freeze-out discussed in Chapter 1.

The stringent flavour constraints force the couplings to quarks to be much smaller

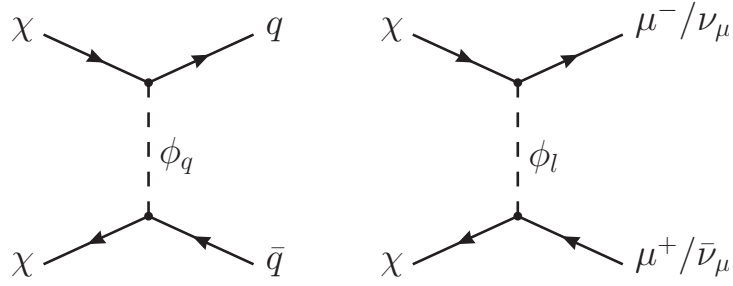


Figure 6.2: Tree-level contributions to the DM pair annihilation.

than the couplings to leptons (muons and neutrinos), and the combination of flavour and collider bounds impose $m_{\phi_q} > m_{\phi_l}$, with coloured scalars generally above 1 TeV. Therefore DM annihilation into a $\mu^- \mu^+$ or $\nu_\mu \bar{\nu}_\mu$ pair is the dominant channel. The thermally-averaged annihilation cross section, $\langle \sigma v \rangle$, can be expressed as a plane wave expansion in terms of the dimensionless parameter $x = m_\chi/T$. As with the case where the Majorana fermion annihilates primarily through the anapole interaction (Eq.(1.31)), the zero-velocity term is helicity suppressed, and the leading contribution comes from the linear term in $1/x$ [321],

$$\langle \sigma v \rangle = 2 \frac{|\lambda_\mu|^4 m_\chi^2 (m_{\phi_l}^4 + m_\chi^4)}{16\pi (m_{\phi_l}^2 + m_\chi^2)^4} \frac{1}{x}, \quad (6.9)$$

where we have neglected the muon and the neutrino masses. In order to reproduce the correct relic abundance, we can now impose $\langle \sigma v \rangle = 2.2 \times 10^{-26} \text{ cm}^3 \text{ s}^{-1}$ (where $x \sim 20$ at freeze-out) [322].

If our DM candidate were a Dirac fermion, the helicity suppression would not be present and the dominant contribution would be velocity independent, meaning that $\langle \sigma v \rangle$ today is the same as at the time of freeze out. Figure 6.3 shows how indirect detection constraints impact the Dirac case. AMS [323, 324] and Fermi [325] exclude a cross section today that provides the correct relic abundance below $m_\chi \sim 20$ GeV. In the velocity dependent Majorana case, the expected thermal cross-section is much lower due to the difference of velocities in the Galaxy today and the time of freeze-out.

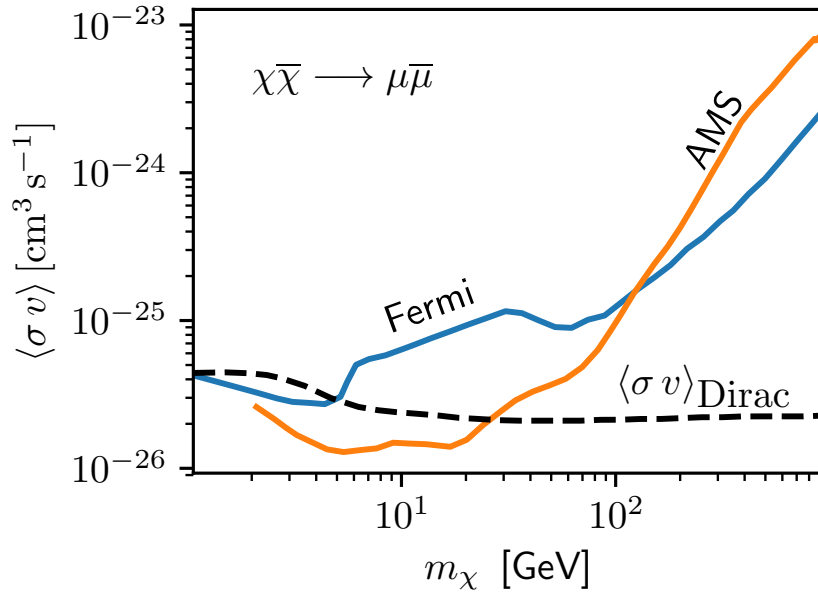


Figure 6.3: The indirect detection constraints for the annihilation to muons from Fermi [325] and AMS [323, 324]. The thermal cross sections today is shown for the Dirac DM candidate in this model.

We will use Eq.(6.9) and the relic abundance condition to fix m_{ϕ_i} as a function of the other parameters, thus effectively reducing by one the number of free parameters.

B_s -mixing and other flavour constraints

This model introduces new couplings to the s and b quarks (and to the rest of the quarks by rotation of the CKM matrix). We must therefore incorporate constraints from B meson physics.

The most relevant bounds are those that involve $b \rightarrow s\mu^+\mu^-$ transitions. The new physics contribution to the Wilson coefficient comes from box and photon-penguin

diagrams [278, 279], $C_9^{\text{NP}} = C_9^{\text{box}} + C_9^\gamma$, with³

$$\begin{aligned} C_9^{\text{box}} &= \frac{\sqrt{2}}{128\pi\alpha_{\text{em}}G_F m_\psi^2} \frac{\lambda_s \lambda_b^*}{V_{tb} V_{ts}^*} |\lambda_\mu|^2 (F(x_q, x_l) + 2G(x_q, x_l)) , \\ C_9^\gamma &= \frac{\sqrt{2}}{8G_F m_\psi^2} \frac{\lambda_s \lambda_b^*}{V_{tb} V_{ts}^*} F_9(x_q) , \end{aligned} \quad (6.10)$$

where we have defined the dimensionless variables $x_q = m_{\phi_q}^2/m_\chi^2$ and $x_l = m_{\phi_l}^2/m_\chi^2$, and the loop functions are:

$$\begin{aligned} F(x, y) &= \frac{1}{(1-x)(1-y)} + \frac{x^2 \log x}{(1-x)^2(x-y)} + \frac{y^2 \log y}{(1-y)^2(y-x)} , \\ G(x, y) &= \frac{1}{(1-x)(1-y)} + \frac{x \log x}{(1-x)^2(x-y)} + \frac{y \log y}{(1-y)^2(y-x)} , \\ F_9(x) &= \frac{-2x^3 + 9x^2 - 18x + 6 \log x + 11}{36(x-1)^4} . \end{aligned} \quad (6.11)$$

The term $G(x_q, x_l)$ vanishes if χ is a Dirac particle.

In order to constrain the Wilson coefficients we use the first global fit that takes into account the possibility that C_9 and C_{10} are complex [326]. This is a scenario that arises when new CP-violation sources are introduced, and has not been studied in detail in the literature so far.

Likewise, the new physics contribution to B_s -mixing can be parameterised in terms of an effective Hamiltonian,

$$\mathcal{H}_{\text{eff}}^{b\bar{s}} = C_{B\bar{B}}^{\text{NP}} (\bar{s}_\alpha \gamma^\mu P_L b_\alpha) (\bar{s}_\beta \gamma_\mu P_L b_\beta) , \quad (6.12)$$

where α and β are colour indices. The new physics contribution to the Wilson coefficient is given by

$$C_{B\bar{B}}^{\text{NP}} = \frac{1}{128\pi^2 m_\psi^2} (\lambda_s \lambda_b^*)^2 (F(x_q, x_q) + 2G(x_q, x_q)) , \quad (6.13)$$

where the loop functions F and G were already defined in Eq. (6.11).

³We have neglected the Z -penguin contribution to C_9^{NP} , since it is suppressed by $(m_b/m_Z)^2$ and is subdominant compared to the photon exchange.

In order to quantify the allowed magnitude of the Wilson coefficient C_{BB}^{NP} , we follow the steps of [308] and introduce a complex parameter Δ in the following way:

$$\frac{M_{12}^{\text{SM}} + M_{12}^{\text{NP}}}{M_{12}^{\text{SM}}} \equiv |\Delta| e^{i\phi_\Delta}, \quad (6.14)$$

where M_{12}^{SM} and M_{12}^{NP} describe the SM and new physics contributions to B_s -mixing, and their values are given by the corresponding box diagrams. The complex phase, ϕ_Δ , quantifies the CP-violating effects introduced by the imaginary parts of the new couplings. We find:

$$\begin{aligned} |\Delta| &= \frac{\Delta M_s^{\text{exp}}}{\Delta M_s^{\text{SM}}} = \left| 1 + \frac{C_{BB}^{\text{NP}}}{C_{BB}^{\text{SM}}} \right|, \\ \phi_\Delta &= \text{Arg} \left(1 + \frac{C_{BB}^{\text{NP}}}{C_{BB}^{\text{SM}}} \right), \end{aligned} \quad (6.15)$$

where ΔM_s is the mass difference of the mass eigenstates of the B_s meson.

The parameter $|\Delta|$ can be constrained using the most precise experimental measurement of ΔM_s [327] and the last update on its theoretical prediction [308], which show a 1.8σ difference,

$$\begin{aligned} \Delta M_s^{\text{exp}} &= (17.757 \pm 0.021) \text{ ps}^{-1}, \\ \Delta M_s^{\text{SM}} &= (20.01 \pm 1.25) \text{ ps}^{-1}. \end{aligned} \quad (6.16)$$

The dominant uncertainties in the calculation of ΔM_s^{SM} come from lattice predictions for the non-perturbative bag parameter, \mathcal{B} , and decay constant, f_{B_s} , and to a lesser extent from the uncertainty in the values of CKM elements. Both of these errors have been considerably reduced since the last theory update for the mass difference [328]. The last average given by the lattice community [329] gives significantly more precise values for \mathcal{B} and f_{B_s} .

From these values, one can infer $|\Delta| = 0.887 \pm 0.055$, and using the data provided in Ref. [308] we obtain $C_{BB}^{\text{SM}} = 4.897 \times 10^{-5} \text{ TeV}^{-2}$. Using Eq. (6.15) we find that

the Wilson coefficient has to satisfy

$$\sqrt{\left(1 + \frac{\text{Re } C_{BB}^{\text{NP}}}{C_{BB}^{\text{SM}}}\right)^2 + \left(\frac{\text{Im } C_{BB}^{\text{NP}}}{C_{BB}^{\text{SM}}}\right)^2} \in [0.777, 0.998] \quad (2\sigma). \quad (6.17)$$

CP-violating effects are further constrained by the CP asymmetry of the golden mode $B_s \rightarrow J/\psi \phi$ [327],

$$A_{\text{CP}}^{\text{mix}}(B_s \rightarrow J/\psi \phi) = \sin(\phi_\Delta - 2\beta_s) = -0.021 \pm 0.031, \quad (6.18)$$

where $\beta_s = 0.01852 \pm 0.00032$ [330], and penguin contributions are neglected. Using Eq. (6.15), this can be interpreted as an additional constraint on the real and imaginary parts of C_{BB}^{NP} (and in turn, on the real and imaginary parts of the couplings $\lambda_s \lambda_b^*$).

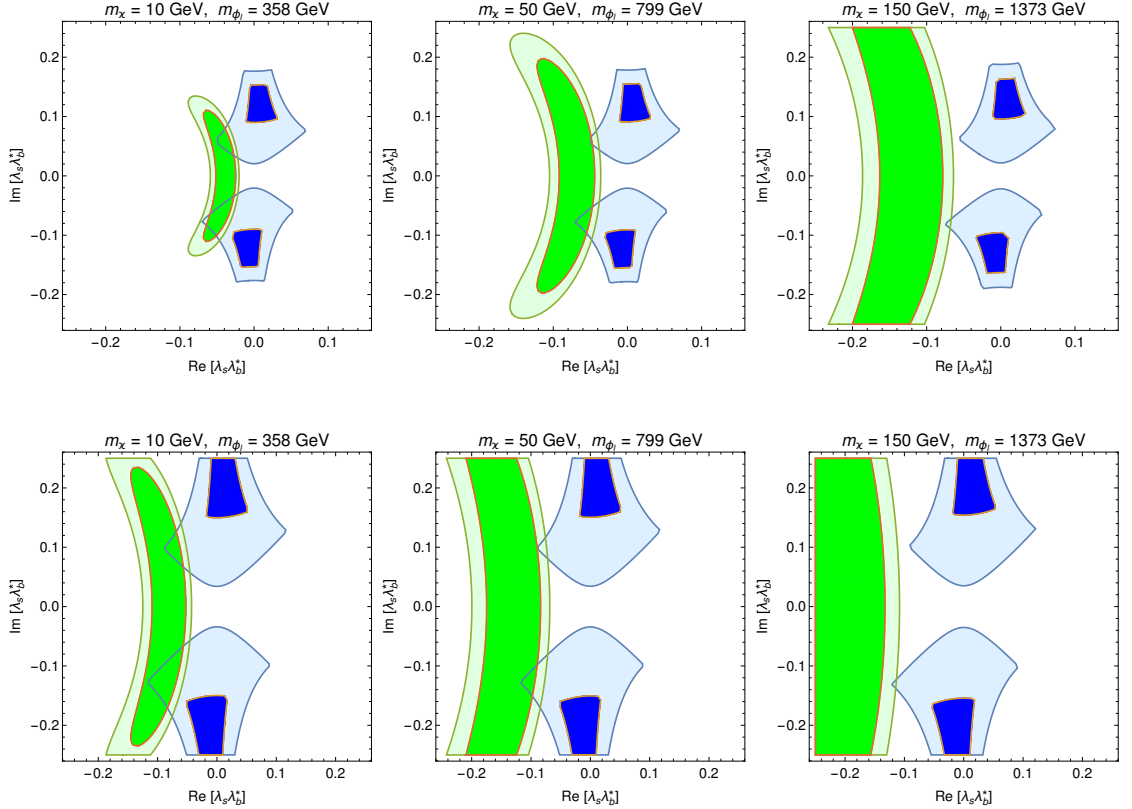


Figure 6.4: The dark (light) green area is the 1σ (2σ) allowed region by $b \rightarrow s\mu^+\mu^-$ observables in the $(\text{Re}(\lambda_s \lambda_b^*), \text{Im}(\lambda_s \lambda_b^*))$ plane. Dark (light) blue regions correspond to 1σ (2σ) B_s -mixing allowed regions. We take $\lambda_\mu = \sqrt{4\pi}$ and $m_{\phi_q} = 1.5 \text{ TeV}$ (top row), 2.5 TeV (bottom row). The specific values of m_χ , m_{ϕ_q} are given in the plot and m_{ϕ_l} is fixed to reproduce the measured DM relic abundance.

In Figure 6.4, the effect of all of these constraints on the real and imaginary parts of the couplings $\lambda_s \lambda_b^*$ for several benchmark points is shown. Regions that are allowed by $b \rightarrow s \mu^+ \mu^-$ observables and B_s -mixing (given by Eqs. (6.17) and (6.18)) are shaded in green and blue, respectively. For illustrative purposes, the figure shows the constraints for multiple values of DM and mediator masses, while keeping $\lambda_\mu = \sqrt{4\pi}$ fixed. We remind the reader that once the DM mass is fixed, the m_{ϕ_l} is constrained by the relic density restriction Eq. (6.9).

As we can observe, in order to simultaneously satisfy both types of constraints, complex couplings are needed ($\text{Im}(\lambda_s \lambda_b^*) \neq 0$). Also, as the mass of the dark matter particle and the mediators increase, both areas are more difficult to reconcile. In practise, this leads to an upper bound on the masses of the exotic new particles. The precise limit depends on the choice of couplings, which we will discuss in Section 6.4.

Finally, the new physics couplings to the up-type quarks are generated via CKM rotation,

$$\begin{aligned}\lambda_u &= V_{us} \lambda_s + V_{ub} \lambda_b, \\ \lambda_c &= V_{cs} \lambda_s + V_{cb} \lambda_b.\end{aligned}\tag{6.19}$$

These couplings generate a new physics contribution to D^0 -mixing, and the Wilson coefficient $C_{D\bar{D}}^{\text{NP}}$ is obtained replacing λ_s and λ_b^* in Eq. (6.13) by λ_u and λ_c^* , respectively.

In contrast to B_s -mixing, there is no precise theory determination for the mass difference in the D^0 system. Therefore, in order to constrain the new physics contribution to $C_{D\bar{D}}$ we use the measured value of the mass difference in D^0 -mixing. The experimental bound on the mixing diagram is given by [331]

$$|M_{12}|_{D\bar{D}}^{\text{exp}} \in [0.6, 7.5] \times 10^{-3} \text{ ps}^{-1} \quad (2\sigma),\tag{6.20}$$

whereas the new physics contribution to D^0 -mixing is described by

$$|M_{12}|_{D\bar{D}} = \frac{|C_{D\bar{D}}|}{2M_{D^0}} \langle D^0 | \mathcal{O} | \bar{D}^0 \rangle, \quad (6.21)$$

where \mathcal{O} is a combination of operators containing all possible SM and new physics contributions to D^0 -mixing. Using the last results from [332] we get the following bound on the Wilson coefficient:

$$|C_{D\bar{D}}^{\text{exp}}| \leq 5.695 \times 10^{-8} \text{ TeV}^{-2} \quad (2\sigma). \quad (6.22)$$

Although this model induces new physics contributions to other flavour observables (such as $b \rightarrow s\gamma$, $b \rightarrow s\nu\bar{\nu}$ and effective $Z\mu^+\mu^-$ and Zq_iq_j couplings), their size is very small and does not produce significant deviations from current experimental searches.

Benchmark scenarios

All the new physics contributions to the observables described above depend on five independent parameters: the three masses of the new particles, m_χ , m_{ϕ_q} and m_{ϕ_l} , the product of the couplings $\lambda_s\lambda_b^*$ and the absolute value of the coupling $|\lambda_\mu|$.

The three masses only enter the Wilson coefficients through the factor m_χ^{-2} and the dimensionless loop functions. In addition, all the Wilson coefficients are proportional to $\lambda_s\lambda_b^*$ or $|\lambda_\mu|^2$ or both. In order to constrain our model, we consider two scenarios by fixing the value of $|\lambda_\mu|$. Then we scan over the mass parameters m_χ and m_{ϕ_q} , with m_{ϕ_l} fixed by the requirement of reproducing the correct relic abundance, and check all the flavour observables described in Section 6.2. In this way, for any combination of masses and a fixed value of $|\lambda_\mu|$ we get a set of allowed values for $\lambda_s\lambda_b^*$. We consider two hierarchies between $|\lambda_s|$ and $|\lambda_b|$ that lead to different constraints from

D^0 -mixing, and, ensuring that $\text{Im}(\lambda_s \lambda_b^*) \neq 0$, we define the following benchmark scenarios:

$$\begin{aligned} \text{(A1)} \quad |\lambda_\mu| = 2, \text{ with } \lambda_b = \lambda_s^*; & \quad \text{(B1)} \quad |\lambda_\mu| = \sqrt{4\pi}, \text{ with } \lambda_b = \lambda_s^*; \\ \text{(A2)} \quad |\lambda_\mu| = 2, \text{ with } \lambda_b = 4\lambda_s^*; & \quad \text{(B2)} \quad |\lambda_\mu| = \sqrt{4\pi}, \text{ with } \lambda_b = 4\lambda_s^*, \end{aligned}$$

where $|\lambda_\mu| = \sqrt{4\pi}$ is the perturbative limit. After establishing a hierarchy between $|\lambda_s|$ and $|\lambda_b|$, we calculate their maximum and minimum allowed values from the corresponding maximum and minimum allowed values of $\lambda_s \lambda_b^*$. Scenarios with $|\lambda_s| > |\lambda_b|$ are excluded by D^0 -mixing constraints. Likewise, as we will see in Section 6.4, smaller values of λ_μ are constrained by LHC bounds.

6.3 Direct DM detection prospects and constraints

In this section we return to familiar territory and discuss whether our model is expected to produce an observable response in direct detection experiments. We have calculated this response, by matching the model parameters to the effective DM-nucleon interaction terms in Eq.(2.4) and Table 2.1. By rotating the quark interaction in Figure 6.2, we see that the leading tree-level process is a s-channel one. As discussed in Section 2.2, we can recover the $\mathcal{J}_{\text{DM}}\mathcal{J}_{\text{SM}}$ via the Fierz transformations. These result in scalar $(\bar{\chi}\chi\bar{\psi}\psi)$ and vector $(\bar{\chi}\gamma^\mu\chi\bar{\psi}\gamma_\mu\psi)$ type interactions. The latter is the leading contribution to \mathcal{O}_1 for Dirac DM [333], but it vanishes in the case of Majorana DM. For scalar type interactions Majorana DM does not in general vanish, but with our models chiral structure, i.e. $\lambda_{Q_i}\bar{Q}_i\phi_q P_R\chi$, it does.

The other interaction coming from the tree-level process is the spin-dependent inter-

action \mathcal{O}_4 , which as we know from Figure 2.2, is much weaker than the \mathcal{O}_1 response. Additionally, sub-dominant couplings to the first generation of quarks, and given that $m_{\phi_q} > m_{\phi_l}$, one-loop processes with the lepton scalar ϕ_l contributes to the DM-nucleon scattering cross sections to a greater extent than the tree level. The leptons loop contributions couple to photons as discussed in Chapter 2. In Section 2.2, the generic fermionic DM that involve the exchange of a photon can be classified as electric and magnetic dipoles ($\bar{\chi}i\sigma^{\mu\nu}\gamma^5\chi F_{\mu\nu}$ and $\bar{\chi}\sigma^{\mu\nu}\chi F_{\mu\nu}$, respectively), anapole ($\bar{\chi}\gamma^\mu\gamma^5\chi\partial^\nu F_{\mu\nu}$), and charge radius ($\bar{\chi}\gamma^\mu\chi\partial^\nu F_{\mu\nu}$). However, in the particular case of Majorana DM considered in this work, the magnetic dipole and charge radius effective couplings are forbidden by charge conjugation symmetry. Thus, the dominant one-loop interaction to the photon is the now familiar anapole moment from Chapters 2 and 5 which gives contributions to the \mathcal{O}_8 and \mathcal{O}_9 operators following the result in Eq.(2.29).

To make the connection with the parameters of the model, one has to integrate out the scalar ϕ_l and leptons that run in the loop shown in Figure 6.5. Similar models have been considered in the literature [334] giving the result,

$$\mathcal{A} = -\frac{e|\lambda_\mu|^2}{96\pi^2 m_\chi^2} \left[\frac{3}{2} \log \frac{\mu}{\epsilon} - \frac{1+3\mu-3\epsilon}{\sqrt{(\mu-1-\epsilon)^2-4\epsilon}} \operatorname{arctanh} \left(\frac{\sqrt{(\mu-1-\epsilon)^2-4\epsilon}}{\mu-1+\epsilon} \right) \right] \quad (6.23)$$

with $\mu \equiv m_{\phi_l}^2/m_\chi^2$ and $\epsilon \equiv m_l^2/m_\chi^2$. The nuclear responses to the \mathcal{O}_8 and \mathcal{O}_9 operators are markedly weaker than that of \mathcal{O}_1 , which implies that, in general, the scattering cross section is very small and beyond current experimental limits. Note that a loop similar to that of Figure 6.5 but with ϕ_q and q running in the loop instead. The contributions of such diagrams will be suppressed by comparison.

Another contribution which is not a priori sub dominant comes from the so-called

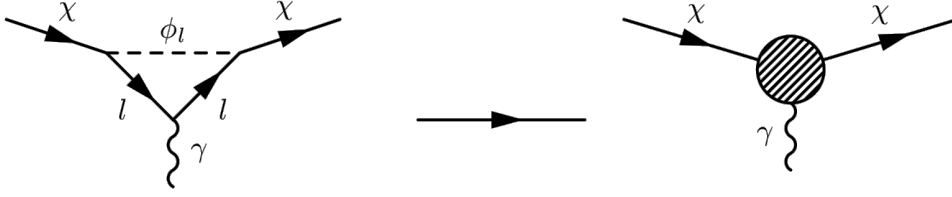


Figure 6.5: Loop process that leads to DM anapole interaction in this model.

twist-2 operators [335–337],

$$\begin{aligned}\mathcal{O}_{\mu\nu}^q &\equiv \frac{1}{2}\bar{q}i\left(D_\mu\gamma_\nu + D_\nu\gamma_\mu - \frac{1}{2}g_{\mu\nu}\not{D}\right)q \\ \mathcal{O}_{\mu\nu}^g &\equiv G_\mu^{A\rho}G_{\nu\rho}^A - \frac{1}{4}g_{\mu\nu}G_{\rho\sigma}^AG^{A\rho\sigma}\end{aligned}\quad (6.24)$$

where here D_μ is the covariant derivative, we have made use of the Dirac slash notation $\not{D} = \gamma^\mu D_\mu$ and $G_{\mu\nu}^A$ is the gluon field strength tensor. These operators when embedded in the nucleons via the evaluation of the hadron matrix element become,

$$\begin{aligned}\langle N(p) | \mathcal{O}_{\mu\nu}^q | N(p) \rangle &= \frac{1}{m_N} \left(p_\mu p_\nu - \frac{1}{4}m_N^2 g_{\mu\nu} \right) (q(2; \mu) + \bar{q}(2; \mu)) \\ \langle N(p) | \mathcal{O}_{\mu\nu}^g | N(p) \rangle &= -\frac{1}{m_N} \left(p_\mu p_\nu - \frac{1}{4}m_N^2 g_{\mu\nu} \right) g(2; \mu),\end{aligned}\quad (6.25)$$

where $q(x, \mu)$, $\bar{q}(x, \mu)$ and $g(x, \mu)$ are the PDFs of quarks, antiquarks and gluon at the factorization scale μ , see Ref. [336] for details. From the NREFT perspective, the m_N^2 terms will contribute to the scalar interaction,

$$c_1^{(N)} = \sum_Q \frac{|\lambda_Q|^2}{32 (m_\chi^2 - m_{\phi_q}^2)^2}. \quad (6.26)$$

Because of the increased sensitivity to the \mathcal{O}_1 response, it is possible that despite the extra mass suppressions with respect to the spin-dependent and anapole interaction, the twist-2 modification may well be dominant.

Given the range of DM masses that we consider in this study, the main constraint is due to Xenon1T results [102], which we simulate using the prescription outlined in Appendix A of Ref. [177], achieving good agreement as shown in Chapter 3.

Where here we have adopted the so-called standard halo model [181] with local DM density $\rho_\chi = 0.4 \text{ GeV/cm}^3$, a central velocity of $v_0 = 220 \text{ km s}^{-1}$, and a escape speed of $v_{\text{esc}} = 544 \text{ km s}^{-1}$ to calculate the number of expected recoils in a specific experiment.

As we can see in Figure 6.6, the theoretical predictions for this model are beyond the reach of current experimental searches. We also show the reach of future direct detection experiments. The LZ detector, will employ 5.6 tons of liquid xenon with 1000 days exposure as outlined in [231, 338]. The DarkSide-20k experiment [113], is an argon detector which will employ 20 tons of fiducial mass for a duration of 10 years. We have assumed that the DarkSide collaboration will be able to achieve a threshold energy of 5 keV, a reasonable assumption considering the results from DarkSide-50 [115]. For reference we have also calculated the neutrino floor for anapole interactions in the (\mathcal{A}, m_χ) plane and for the \mathcal{O}_1 interactions in the (c_1, m_χ) plane. We have used the prescription described in Ref. [147] and the expected neutrino fluxes from Refs. [148–152].

It is clear that our model favourably lays in a region of parameter space that would be probed by a generation of experiments with multi-ton targets, that can probe near or even slightly beyond the neutrino floor. Spectral analysis with the neutrino background compounded with annual modulation data, could provide complete discrimination between model and the anapole moment which is both velocity and momentum dependent.

Notice in Figure 6.6 that the Anapole and \mathcal{O}_1 responses have very different character. This is simply explained by the benchmarks we have chosen and what parameters are allowed to run freely. By looking at Eq.(6.23) one can see that, once λ_μ is fixed, \mathcal{A} is simply a function of SM values and m_χ , this produces the straight line we see in Figure6.6. The c_1 plane is much more free with our scan, this is because c_1

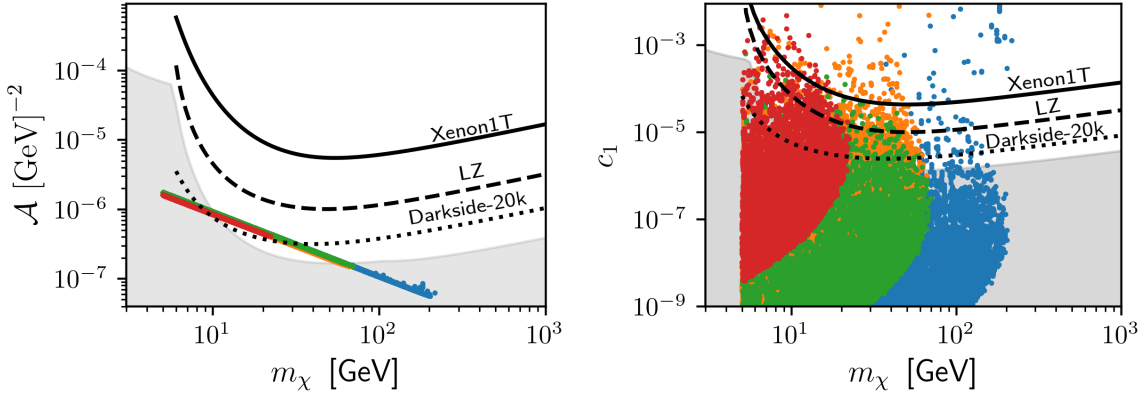


Figure 6.6: Theoretical predictions for the anapole (**left**) and spin-independent (**right**) couplings, \mathcal{A} and c_1 , as a function of the DM mass, m_χ for the four benchmark points: A1 (red points), A2 (green), B1 (orange), and B2 (blue). For comparison, we show the current exclusion line by Xenon1T [102] and the predicted reach of LZ [231, 338] and DarkSide-20k [113]. The shaded area represents the neutrino floor.

depends on the quark couplings to the new mediator, a coupling that is varied over in our analysis. We see a pattern develop however, at m_χ increases, the variation of possible c_1 values gets smaller and smaller. This is a reflection on the fact that the flavour anomalies are running out of parameter space to satisfy both the leptonic decays and B_s -mixing as shown in Figure 6.4.

We have neglected to show the spin-dependent \mathcal{O}_4 interactions in Figure 6.6 because they are always sub-dominant. It is clear from the variation of c_1 contributions that the quark interactions are fairly unconstrained in this model and in fact current Xenon1T results are constraining this model via its twist-2 contribution. The figure is unable to capture the density of the parameter point, but its worth noting that only 1% of points have a dominant c_1 contribution in Xenon1T. This suggests that the situation where c_1 contribution is high, is by no means required by the model, and instead it is just a possibility that is not ruled out by the flavour constraints mentioned in Section 6.2.

Had we chosen to work with a Dirac fermion, the dipole and charge radius contribu-

tions should have been added. As it has been pointed out in Ref. [333], the fairly large coupling to muons that is required to explain the flavour anomalies leads to effective DM couplings that are orders of magnitude higher than those coming from the tree level contribution, the most important being the charge-radius interaction. This we have checked, and in fact above $m_\chi \sim 10$ GeV, all our parameter points are excluded by Xenon1T.

Below $m_\chi \sim 10$ GeV, the model is excluded by indirect detection bounds as discussed in Section 6.2. Unlike in the Majorana case, the S-wave contribution to the thermal cross section $\langle\sigma v\rangle$ is no longer helicity suppressed and hence excluded [339].

6.4 LHC constraints and prospects for high-luminosity

In this section, we study the experimental signatures that this model would produce at the LHC. DM search strategies in both ATLAS and CMS involve analysing final states containing jets and leptons produced in association with a DM particle, identified from missing transverse energy. In this model, direct production of the coloured and leptonic scalar doublets ϕ_q and ϕ_l , respectively, typically leads to such final states.

Let us first consider production processes that involve the coloured scalar, ϕ_q . In this case, our model could lead to visible signals in final states with both monojet / dijet + \cancel{E}_T signatures. When the new physics coupling λ_q is smaller than the strong interaction coupling, α_{QCD} , pure QCD processes constitute the main contribution to the cross section [340]. In this model, this implies that QCD diagrams dominate over those with new physics couplings. As a consequence, monojet searches for this

model are less effective than dijet searches and we will concentrate on the latter. The dijet + \cancel{E}_T processes are shown in Figure 6.7, where diagrams (a) correspond to the QCD contributions, and diagrams (b) and (c) involve new physics couplings. The main production channel is the pair production of the coloured scalar particles, that subsequently decays into a DM particle and a quark,

$$pp \rightarrow \phi_q \phi_q^* / \phi_q \phi_q / \phi_q^* \phi_q^* \rightarrow qq + \cancel{E}_T. \quad (6.27)$$

In addition, the scalar doublet ϕ_q has the same quantum numbers as squarks in supersymmetric (SUSY) models. Therefore, the kinematics in its production and decay in diagrams (a) of Figure 6.7 mimic those of squarks in SUSY models with decoupled gluinos. As a consequence, limits from ATLAS and CMS squark searches can be used to constrain the model.

One can also consider the pair production of the leptonic scalar, ϕ_l . In this case, the production process is mediated by W or Z bosons and involves the electroweak coupling, as shown in Figure 6.8. The decays of ϕ_l lead to clean final states with one or two leptons and missing energy. Although flavour constraints require $\lambda_\mu \gg \lambda_q$, the cross section of this process is smaller than the production of the coloured mediator for similar mediator masses. However, since m_{ϕ_l} is fixed for every value of m_χ to reproduce the correct relic abundance, there are regions of the parameter space where both searches are complementary. We will here consider the process

$$pp \rightarrow \phi_l \phi_l^* \rightarrow \mu\mu / \mu\nu + \cancel{E}_T, \quad (6.28)$$

where the dimuon channel leads to the strongest constraints. As in the previous case, we can exploit the analogy between ϕ_l and sleptons to use the limits from slepton searches to constrain this model.

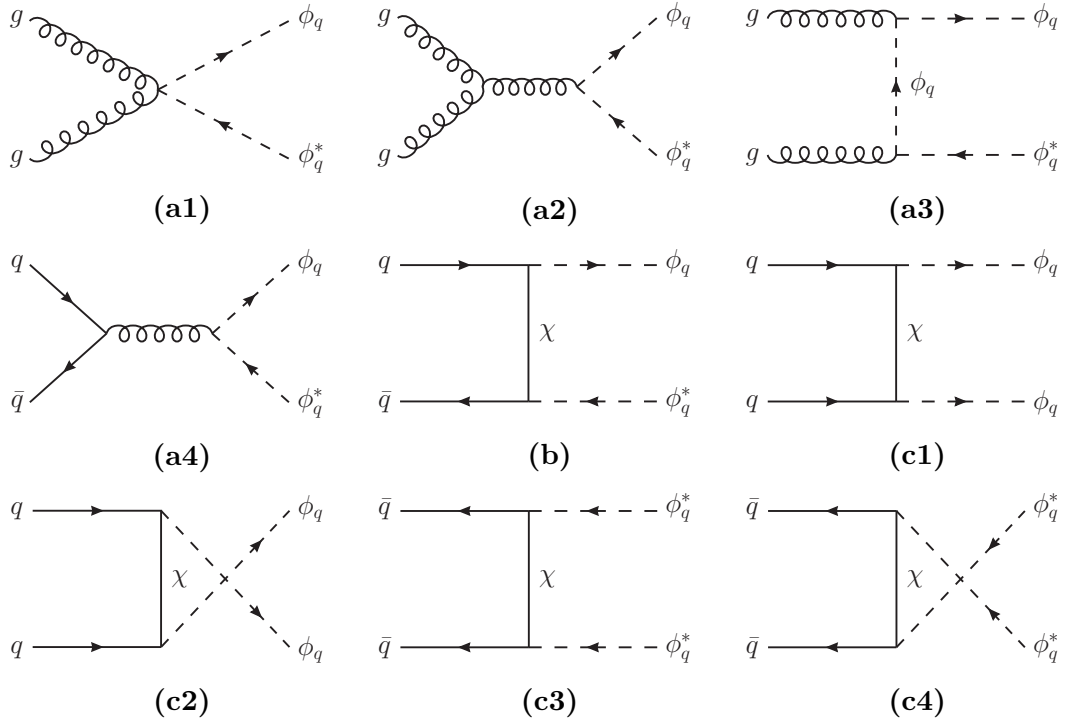


Figure 6.7: Diagrams for the pair production of the coloured scalar mediator, ϕ_q , leading to dijet + \cancel{E}_T signatures in the final state. Diagrams (a1)–(a4) are generated by purely QCD interactions, and diagrams (b), (c1)–(c4) are generated by DM t-channel exchange.

Simulation details

We have implemented this model in `Feynrules 2.3` [341]. The calculation of the matrix elements and the event generation is done using `MadGraph5_aMC@NLO 2.6.3` [342]. Production and decay of the new particles are considered independently using the narrow width approximation, as implemented in `MadSpin` [343], which further accounts for spin correlations in decay chains⁴. We then use `Pythia 8.235` [344] to shower the parton-level events and we pass the output to `CheckMATE 2.0.26` [345], which compares the expected signal with supersymmetric searches at the LHC and derives an exclusion limit. As we have explained above, we can apply squark and slepton searches to constrain the coloured and leptonic mediator, respectively.

⁴The narrow width approximation is not valid in benchmark points B1 and B2, for which we have taken interference effects into account.

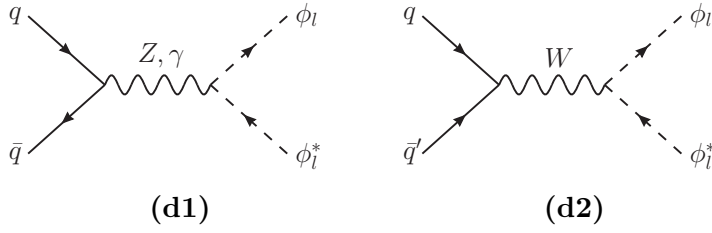


Figure 6.8: Diagrams for the pair production of the leptonic scalar mediator, ϕ_l , leading to $\mu\mu/\mu\nu + \cancel{E}_T$ signatures in the final state.

In order to describe initial and final state radiation and reproduce the correct jet structure precisely, we consider leading order (LO) production with parton shower matching and multijet merging when needed. The LO multijet merging techniques describe how parton shower emissions can be combined with full matrix element calculations to achieve a better accuracy in the description of the radiation spectrum. Using this technique, every jet is classified according to its p_T and then compared to a hardness scale Q_{cut} . In this way, emissions above the hardness scale Q_{cut} are described at LO accuracy using the corresponding matrix element calculation for an extra hard, wide-angle QCD emission in the final state, while emissions below this scale are defined as soft or collinear jets and the all-orders resummation description from the parton shower is preserved. Note that even though $\mathcal{O}(\alpha_s)$ corrections are included using this procedure, the calculation remains formally LO + LL accurate after parton shower due to missing virtual corrections.

After hadronization, the showered events and the production cross sections are passed to CheckMATE. Each model point is tested against all the implemented experimental analyses to determine the optimal signal region. For this signal region, CheckMATE compares the simulated signal with the actual experimental observation and determines whether the model point is excluded at the 90% confidence level.

Results

Constraints from LHC searches for the four benchmark points defined in Section 6.2 are presented in Figure 6.9 on the (m_χ, m_{ϕ_q}) plane, for all the points that satisfy the flavour constraints of Section 6.2 and that reproduce the correct DM relic abundance. This figure shows the complementarity between the experimental limits obtained from the $pp \rightarrow jj + \cancel{E}_T$ and $pp \rightarrow \mu\mu + \cancel{E}_T$ searches. The experimental results used in our analysis are summarised in Table 6.2. The colour code represents the average value of the coupling $|\lambda_b|$ in the region allowed by flavour constraints, defined as $|\lambda_b|_{\text{mean}} = (|\lambda_b|_{\text{max}} + |\lambda_b|_{\text{min}})/2$, where $|\lambda_b|_{\text{max}}$ and $|\lambda_b|_{\text{min}}$ are the maximum and minimum allowed values respectively. The variation of our results when choosing either the minimum or maximum value for $|\lambda_b|$ has been checked and is insignificant.

Regarding the $pp \rightarrow jj + \cancel{E}_T$ search, the limits in every scenario show that for the lightest DM mass, coloured mediators with masses below ~ 1 TeV are excluded. Even though heavier DM produces larger amounts of missing energy in final states, the cross section decreases rapidly with the m_χ , leading to similar exclusion limits. It is interesting to note that exclusion limits are slightly stronger for the scenarios with $|\lambda_{b,t}| > |\lambda_{s,c}|$, where mediators with masses below ~ 1.1 TeV are excluded. The reason for this is that final states with either top or bottom quarks are more sensitive to some experimental searches. The most stringent experimental search involves final states with at least two ($b\bar{b}$ production) or four ($t\bar{t}$ production) jets or exactly two leptons and missing energy [346]. In particular, the most sensitive signal region is optimised to detect events featuring a DM particle produced in association with a $t\bar{t}$ pair, which decays fully hadronically.

Regarding the $pp \rightarrow \mu\mu + \cancel{E}_T$ search, the limits show that models with dark matter masses below approximately 30 GeV are ruled out for $|\lambda_\mu| = 2$, with the exclusion limit going down to ~ 13 GeV for $|\lambda_\mu| = \sqrt{4\pi}$. This corresponds to mediator masses

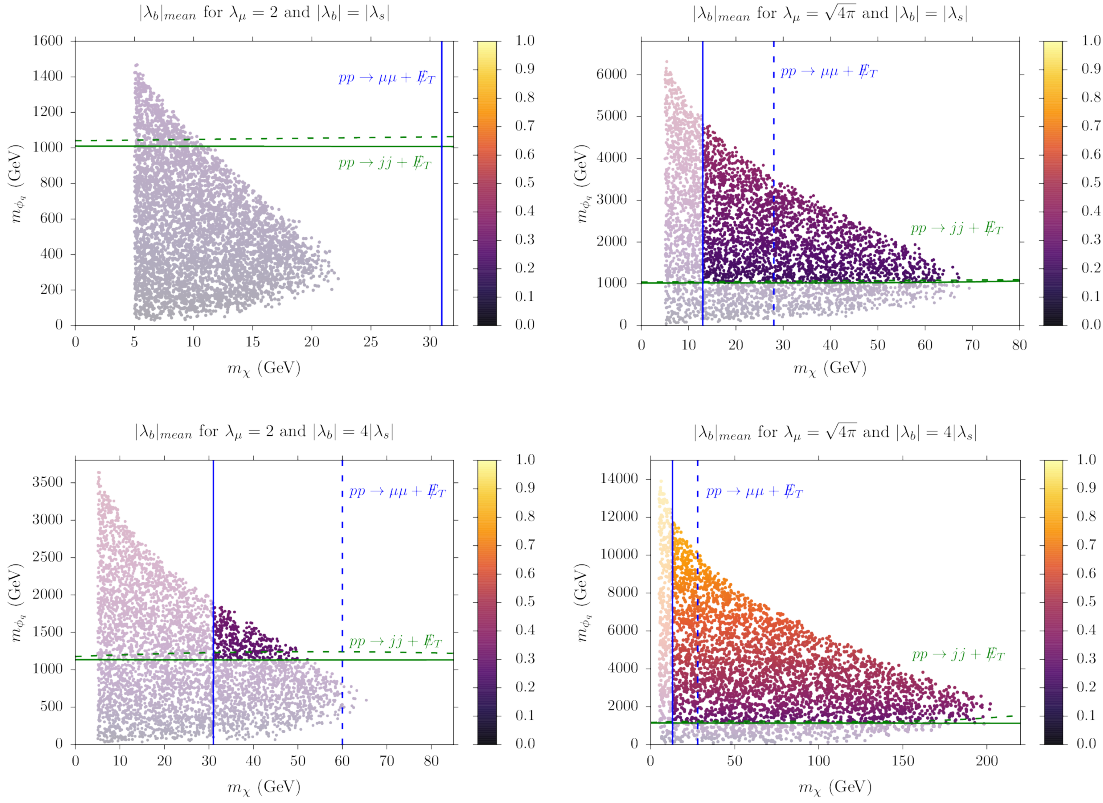


Figure 6.9: LHC limits from the $pp \rightarrow jj + \cancel{E}_T$ (green) and $pp \rightarrow \mu\mu + \cancel{E}_T$ (blue) searches. On the left (right), results for the scenario with $|\lambda_\mu| = 2$ ($|\lambda_\mu| = \sqrt{4\pi}$) are presented. The figures in the upper panel correspond to $\lambda_b = \lambda_s^*$, while the bottom panel shows limits for $\lambda_b = 4\lambda_s^*$. The colour code represents the average value of the coupling $|\lambda_b|$ in the region allowed by flavour constraints, as defined in the text. Solid lines represent the current exclusion limits, whereas dashed ones correspond to the projected reach of the LHC High luminosity phase.

below 360 GeV for $|\lambda_\mu| = 2$ and 410 GeV for $|\lambda_\mu| = \sqrt{4\pi}$. The $pp \rightarrow \mu\mu + \cancel{E}_T$ cross section mainly depends on m_{ϕ_l} , so the limits on m_χ can be understood through its relation with m_{ϕ_l} given by the DM relic condition (6.9) for a particular value of λ_μ . The most stringent search involves final states with $2l + 0j$, $2l$ and at least 2 jets, or $3l$ and missing energy [347]. In particular, the most sensitive signal region is characterised by $2l + 0j$ and a dilepton invariant mass $m_{ll} > 300$ GeV, and it is optimised to target slepton pair production.

The most remarkable result is that LHC limits completely exclude the scenario with $|\lambda_\mu| = 2$ and $\lambda_b = \lambda_s^*$, as well as a sizeable region of the scenario with $\lambda_b = 4\lambda_s^*$ for

\sqrt{s}	Search	Final state	\mathcal{L} [fb $^{-1}$]
13 TeV	1710.11412 [346]	$t\bar{t} / b\bar{b} + \cancel{E}_T$	36.1
	ATLAS-CONF-2017-039 [347]	$2l / 3l + \cancel{E}_T$	36.1
14 TeV	atlas_phys_pub_013_011 [348]	$t\bar{t} + \cancel{E}_T$	3000
	atlas_phys_2014_010_hl_3l [349]	$2l / 3l + \cancel{E}_T$	3000

Table 6.2: List of experimental searches sensitive to our model, where l denotes electron and muon. The third column describes the final state targeted by the analysis and the last column displays the total integrated luminosity.

the same $|\lambda_\mu|$. These constraints become weaker for larger values of $|\lambda_\mu|$ and, for the scenarios with $|\lambda_\mu| = \sqrt{4\pi}$, most of the parameter space is allowed. It is crucial to note that the limits coming from final states with jets and leptons are complementary to each other. While the former exclude regions of the parameter space with large m_χ and small m_{ϕ_q} , the latter rule out models with very heavy mediator masses m_{ϕ_q} and light dark matter. Importantly, these limits are also complementary to the ones coming from direct detection, where dark matter masses below 12 GeV lie below the neutrino floor. Therefore, it is fundamental to consider both approaches to explore the model.

It is worth mentioning that the small couplings required by flavour constraints lead to decay widths slightly below the QCD scale for $m_{\phi_q} \lesssim 370$ GeV. Strictly speaking, this means that the computation of the decay width cannot be handled perturbatively and that the new particle ϕ_q may hadronize into bound states with SM quarks, analogous to R-hadrons [350], before decaying. However, the typical width involved is $\Gamma_{\phi_q} \sim \mathcal{O}(10^{-2}) - \mathcal{O}(10^{-3})$ GeV, which means lifetimes of the order $\tau \sim 10^{-22}$ s, so any potential bound state would decay promptly in the detector. This region of the parameter space is excluded by ATLAS and CMS R-hadron searches [351, 352].

We have also studied the limits that could be obtained with 3000 fb $^{-1}$ of 14 TeV data once the LHC High Luminosity (HL) phase [353] is completed. The experimental

searches giving the strongest exclusion limits target the same final states and are shown in the low panel of Table 6.2. As we can observe in the plots, the main gain would come from the leptonic channels, which would allow to test a considerable amount of the model's parameter space. In particular, scenarios with $|\lambda_\mu| < 2$ would be completely excluded. The axes of Figure 6.9 are somewhat misleading with the relative gain from the HL-LHC between the leptonic and hadronic channels since the scales are vastly different. It is perhaps more illuminating to consider how the values for m_χ correspond to m_{ϕ_l} values. From Eq.6.9 one can determine that the improvement in the HL phase will move the constraints by under 200 GeV. This is still a slightly better improvement when comparing to the dijet searches.

Evaluating why this is, is somewhat difficult without performing the analysis that CheckMATE provides, ourselves. In Figure 6.10 we show an event distribution of a point in the $|\lambda_b|_{\text{mean}}$ for $\lambda_\mu = \sqrt{4\pi}$ and $\lambda_b = 4\lambda_s^*$ scan which is just above the constraints from the 13 TeV results but will be constrained by the 14 TeV, HL analysis, in the leptonic channel. We see that the increased energy increases the cross-section somewhat for both channels so the cause for the difference is unlikely to be there. Upon investigation of the CheckMATE analysis files, the analysis cuts are reducing the new physics signal from the dijet channel substantially. Why this is and how we can improve such searches is currently the subject under investigation, but outside the scope of the work being presented here.

Combining these results with those of Section 6.3, we have Figure 6.11. Once LHC constraints are considered, the parameter points where the anapole interaction is dominant are the only ones left. Our results suggest that future multi-ton direct detection experiments, such as DarkSide [113], would be able to probe this model in the mass range $m_\chi \sim 10 - 60$ GeV. It is very interesting to point out that many of the points in this DM mass range feature very heavy ϕ_q and therefore would be beyond the reach of collider searches. In a sense, future direct DM detection and

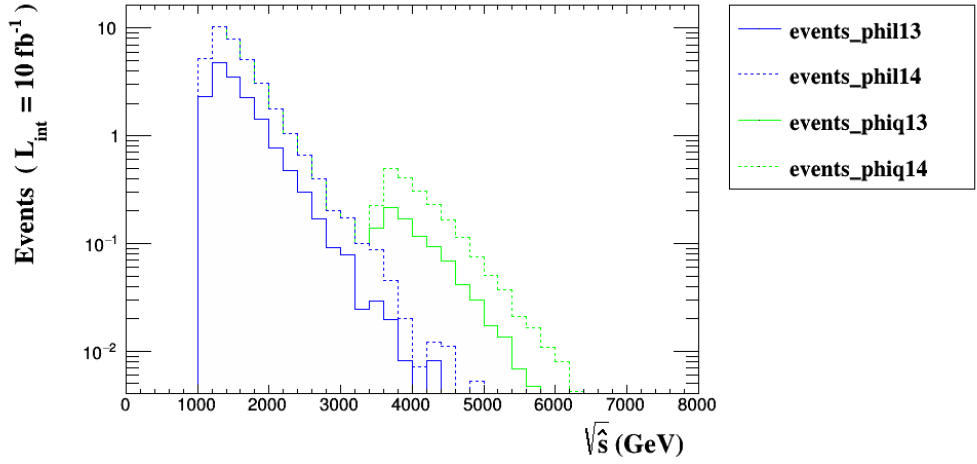


Figure 6.10: Kinematic distributions for dijet (green) and dilepton (blue) signals produced by a benchmark point, which just escapes the constraints for current 13 TeV bounds but will be constrained by the leptonic channel of the HL-LHC. We plot the distribution for both energies of 13 TeV and 14 TeV with a fixed luminosity of 10 fb^{-1} .

the LHC complement each other to probe a large part of the model's parameter space. There are parameter points below the current projected direct detection experiments. However, if the flavour anomalies persist, this model will provide an additional motivation for pushing direct detection below the neutrino floor.

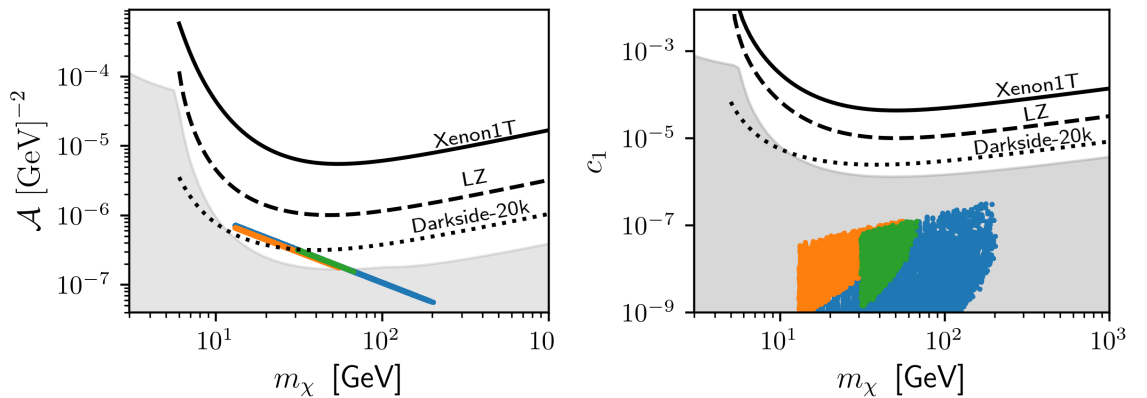


Figure 6.11: The same as in Figure 6.6, but including constraints coming from collider results as shown in Figure 6.9.

6.5 Summary

In this article, we have studied a particle physics model that addresses the hints of lepton flavour universality violation observed by LHCb in $b \rightarrow s\mu^+\mu^-$ transitions, and that provides a solution to the dark matter problem. The scenario that we have analysed incorporates two new scalar fields and a Majorana fermion that provide one-loop contributions to B meson decays.

The Majorana fermion is stable and can reproduce the observed DM relic abundance. We have studied the effect of new physics in flavour observables, for which B_s -mixing and $b \rightarrow s\mu^+\mu^-$ processes provide the most important constraints. In order to find an explanation for the B anomalies and to reduce the 1.8σ tension between the predicted and measured mass difference in B_s -mixing, complex couplings are needed. We have used results from the first global fit that takes into account this possibility. The combination of flavour bounds and constraints on the DM relic abundance leads to upper limits on the masses of the exotic states, and in general points towards a rather light DM candidate (with a mass $m_\chi \lesssim 200$ GeV).

We have investigated how DM direct detection experiments constrain this model. Given the range of DM masses that we consider in this study, the main constraint is due to Xenon1T results. The small new couplings required by flavour constraints means that one-loop contributions to the DM-nucleon scattering cross section are generally larger than the tree level process. In many cases, the dominant loop induced interaction is the anapole moment. We have shown that this model is not excluded by current data and could be probed by the next generation of experiments with multi-ton targets in the mass range $m_\chi \sim 10 - 60$ GeV.

Finally, we have studied the signatures that this model would produce at the LHC. The dominant processes are the pair production of the coloured and leptonic scalars.

For the former, the strongest exclusion limits are given by dijet + \cancel{E}_T searches. For the latter, the final states are very clean, containing 1 or 2 leptons and missing energy. Both searches are complementary and exclude different regions of the parameter space, setting lower bounds on DM and mediator masses. The high-luminosity phase improves bounds coming from both searches, with dilepton being the most pronounced. The collider constraints are weakened when the λ_μ parameter is pushed towards the perturbative limit. These results have been combined with those for direct detection and show that after LHC data is considered the anapole interaction is always dominant.

Chapter 7

Conclusions

The precise nature of DM still eludes us, but this thesis has hopefully shed light on the kinds of analysis that will lead to a greater understanding. Chapter 1 discussed the pivotal role DM plays in our cosmic history without predicting its mass or how it interacts with the SM. Because of this, the theory space for DM is truly expansive. It is our job to exclude as many of these theories as possible. Over the last decade, experimental probes have made some great progress, but there is much more work to be done.

Currently, direct detection is probing very interesting regions of parameter space. Particularly for DM candidates that could have been thermally produced via freeze-out. In order to fully appreciate the signals one expects from these experiments, the NREFT introduced in Chapter 2, should be used. This framework enables more model independent analyses reviewed in Chapter 3. With this approach we can be sure our search strategy is as comprehensive as possible.

With a more model independent approach, one finds that there is a high degree of

uncertainty, especially when attempting to reconstruct parameters. Luckily however, multiple direct detection experiments are underway or being developed now, providing an excellent opportunity to maximise what can be learnt about DM. To this end, we developed the code RAPIDD, introduced in Chapter 4, which simulates DM signals in direct detection by making use of polynomials. This novel technique showed promising improvements in terms of speed and sacrificed a minimal amount of accuracy. This software allowed for a case study where we evaluated the degeneracies between a subset of simplified models for a series of benchmark points. As shown for the reconstructions of BP1 and BP2, the different simplified models are able to mimic each other well. Only when the true nature of DM is particularly unique, like the pseudoscalar mediated Fermion taken for BP3, is the discrimination power of multiple experiments enough.

The situation is particularly bad if the DM mass is above ~ 50 GeV. Above this value, the recoil spectrum is fairly flat and featureless. Chapter 5 explores the possibility of improving mass reconstruction by extending the signal region analyzed by experiments, and therefore capturing the tail of the spectrum. These features enable a better understanding of the DM mass and can provide great improvements for experimental sensitivities. For example, exclusion limits for anapole DM can be improved by an order of magnitude as shown in Figure 5.2. This increased understanding of the DM mass would have great implications for the degeneracy of signals, providing better reconstructions of couplings. Furthermore, improvements like this across multiple experiments with different target materials could even provide some insight into the DM halo, where statistical tensions can arise between experiments if a the SHM is assumed.

These works above, hopefully go some way toward realising the potential of direct detection, but ultimately, this technology will be a part of the global experimental effort to determine the nature of DM. In Chapter 6 we combined direct detection with

collider, flavour and indirect detection constraints in an effort to probe a specific particle model that can explain both, the anomalies found in meson decays and DM. We found that, if the anomalous measurements persist, future direct detection experiments will play a central role in probing the full parameter space for our particular model.

The mystery of DM remains one of the biggest problems facing particle and astrophysicists alike. When attempting to understand something where so little is known, it can feel like shooting in the dark. However, situations like this one, gives the community the opportunity to challenge our assumptions and to take stock of the information we have, and what information we really want. Through this process, we can find novel ways to look for new physics and learn how to distinguish between different solutions to the DM problem.

Bibliography

- [1] D. G. Cerdeño, A. Cheek, E. Reid and H. Schulz, *Surrogate Models for Direct Dark Matter Detection*, *JCAP* **1808** (2018) 011, [1802.03174].
- [2] N. Bozorgnia, D. G. Cerdeño, A. Cheek and B. Penning, *Opening the energy window on direct dark matter detection*, *JCAP* **1812** (2018) 013, [1810.05576].
- [3] D. G. Cerdeño, A. Cheek, P. Martín-Ramiro and J. M. Moreno, *B anomalies and dark matter: a complex connection*, *Eur. Phys. J.* **C79** (2019) 517, [1902.01789].
- [4] F. Zwicky, *Die Rotverschiebung von extragalaktischen Nebeln*, *Helv. Phys. Acta* **6** (1933) 110–127.
- [5] M. Schwarzschild, *Mass distribution and mass-luminosity ratio in galaxies*, *Astronomical Journal* **59** (Sept., 1954) 273.
- [6] V. C. Rubin and W. K. Ford, Jr., *Rotation of the Andromeda Nebula from a Spectroscopic Survey of Emission Regions*, *Astrophysical Journal* **159** (Feb., 1970) 379.
- [7] A. Bosma, *The distribution and kinematics of neutral hydrogen in spiral galaxies of various morphological types*, Ph.D. thesis, PhD Thesis, Groningen Univ., (1978), 1978.

- [8] R. H. Miller, K. H. Prendergast and W. J. Quirk, *Numerical Experiments on Spiral Structure*, *Astrophysical Journal* **161** (Sept., 1970) 903.
- [9] F. Hohl, *Numerical Experiments with a Disk of Stars*, *Astrophysical Journal* **168** (Sept., 1971) 343.
- [10] J. P. Ostriker and P. J. E. Peebles, *A Numerical Study of the Stability of Flattened Galaxies: or, can Cold Galaxies Survive?*, *Astrophysical Journal* **186** (Dec., 1973) 467–480.
- [11] S. M. Faber and J. S. Gallagher, *Masses and mass-to-light ratios of galaxies*, *Annual Review of Astronomy and Astrophysics* **17** (1979) 135–187, [<https://doi.org/10.1146/annurev.aa.17.090179.001031>].
- [12] G. Bertone, D. Hooper and J. Silk, *Particle dark matter: Evidence, candidates and constraints*, *Phys. Rept.* **405** (2005) 279–390, [[hep-ph/0404175](https://arxiv.org/abs/hep-ph/0404175)].
- [13] M. Milgrom, *A modification of the Newtonian dynamics as a possible alternative to the hidden mass hypothesis*, *Astrophysical Journal* **270** (July, 1983) 365–370.
- [14] M. Milgrom, *A modification of the Newtonian dynamics - Implications for galaxies*, *Astrophysical Journal* **270** (July, 1983) 371–389.
- [15] R. Massey, T. Kitching and J. Richard, *The dark matter of gravitational lensing*, *Rept. Prog. Phys.* **73** (2010) 086901, [[1001.1739](https://arxiv.org/abs/1001.1739)].
- [16] J. D. Bekenstein, *Relativistic gravitation theory for the MOND paradigm*, *Phys. Rev.* **D70** (2004) 083509, [[astro-ph/0403694](https://arxiv.org/abs/astro-ph/0403694)].
- [17] R. H. Sanders, *Clusters of galaxies with modified Newtonian dynamics (MOND)*, *Mon. Not. Roy. Astron. Soc.* **342** (2003) 901, [[astro-ph/0212293](https://arxiv.org/abs/astro-ph/0212293)].
- [18] D. Harvey, A. Robertson, R. Massey and J.-P. Kneib, *Looking for dark matter trails in colliding galaxy clusters*, *Mon. Not. Roy. Astron. Soc.* **464** (2017) 3991–3997, [[1610.05327](https://arxiv.org/abs/1610.05327)].

- [19] M. Markevitch, A. H. Gonzalez, D. Clowe, A. Vikhlinin, L. David, W. Forman et al., *Direct constraints on the dark matter self-interaction cross-section from the merging galaxy cluster 1E0657-56*, *Astrophys. J.* **606** (2004) 819–824, [astro-ph/0309303].
- [20] D. Clowe, M. Bradac, A. H. Gonzalez, M. Markevitch, S. W. Randall, C. Jones et al., *A direct empirical proof of the existence of dark matter*, *Astrophys. J.* **648** (2006) L109–L113, [astro-ph/0608407].
- [21] EROS collaboration, T. Lasserre, *Not enough stellar mass machos in the galactic halo*, *Astron. Astrophys.* **355** (2000) L39–L42, [astro-ph/0002253].
- [22] M. Tegmark, A. Aguirre, M. J. Rees and F. Wilczek, *Dimensionless constants, cosmology, and other dark matters*, *Phys. Rev. D* **73** (Jan, 2006) 023505.
- [23] E. Hubble, *A relation between distance and radial velocity among extra-galactic nebulae*, *Proceedings of the National Academy of Sciences* **15** (1929) 168–173, [<https://www.pnas.org/content/15/3/168.full.pdf>].
- [24] A. A. Penzias and R. W. Wilson, *A Measurement of Excess Antenna Temperature at 4080 Mc/s.*, *Astrophysical Journal* **142** (July, 1965) 419–421.
- [25] E. Kolb and M. Turner, *The Early Universe*. Frontiers in physics. Avalon Publishing, 1994.
- [26] R. A. Alpher, H. Bethe and G. Gamow, *The origin of chemical elements*, *Phys. Rev.* **73** (Apr, 1948) 803–804.
- [27] B. D. Fields, P. Molaro and S. Sarkar, *Big-Bang Nucleosynthesis*, *Chin. Phys.* **C38** (2014) 339–344, [1412.1408].
- [28] PARTICLE DATA GROUP collaboration, J. Beringer, J. F. Arguin, R. M. Barnett, K. Copic, O. Dahl, D. E. Groom et al., *Review of particle physics*, *Phys. Rev. D* **86** (Jul, 2012) 010001.

- [29] P. J. E. Peebles, *Recombination of the primeval plasma*, *The Astrophysical Journal* **153** (06, 1968) 1.
- [30] V. S. Alpher, *Ralph A. Alpher, George Antonovich Gamow, and the Prediction of the Cosmic Microwave Background Radiation*, 1411.0172.
- [31] C. L. Bennett, D. Larson, J. L. Weiland, N. Jarosik, G. Hinshaw, N. Odegard et al., *Nine-year Wilkinson Microwave Anisotropy Probe (WMAP) Observations: Final Maps and Results*, *The Astrophysical Journal Supplement* **208** (Oct, 2013) 20, [1212.5225].
- [32] G. Hinshaw, D. Larson, E. Komatsu, D. N. Spergel, C. L. Bennett, J. Dunkley et al., *Nine-year Wilkinson Microwave Anisotropy Probe (WMAP) Observations: Cosmological Parameter Results*, *The Astrophysical Journal Supplement* **208** (Oct, 2013) 19, [1212.5226].
- [33] W. Hu, N. Sugiyama and J. Silk, *The Physics of microwave background anisotropies*, *Nature* **386** (1997) 37–43, [astro-ph/9604166].
- [34] PLANCK collaboration, P. A. R. Ade et al., *Planck 2015 results. XIII. Cosmological parameters*, *Astron. Astrophys.* **594** (2016) A13, [1502.01589].
- [35] R. Cooke, M. Pettini, R. A. Jorgenson, M. T. Murphy and C. C. Steidel, *Precision measures of the primordial abundance of deuterium*, *Astrophys. J.* **781** (2014) 31, [1308.3240].
- [36] B. Carr, F. Kuhnel and M. Sandstad, *Primordial Black Holes as Dark Matter*, *Phys. Rev.* **D94** (2016) 083504, [1607.06077].
- [37] R. Ichimasa, R. Nakamura, M. Hashimoto and K. Arai, *Big-Bang Nucleosynthesis in comparison with observed helium and deuterium abundances: possibility of a nonstandard model*, *Phys. Rev.* **D90** (2014) 023527, [1404.4831].

- [38] H. Yukawa, *On the Interaction of Elementary Particles. I*, *Progress of Theoretical Physics Supplement* **1** (01, 1955) 1–10.
- [39] N. Cabibbo, *Unitary symmetry and leptonic decays*, *Phys. Rev. Lett.* **10** (Jun, 1963) 531–533.
- [40] M. Kobayashi and T. Maskawa, *CP-Violation in the Renormalizable Theory of Weak Interaction*, *Progress of Theoretical Physics* **49** (02, 1973) 652–657.
- [41] A. J. Buras, P. Gambino, M. Gorbahn, S. Jager and L. Silvestrini, *Universal unitarity triangle and physics beyond the standard model*, *Phys. Lett.* **B500** (2001) 161–167, [[hep-ph/0007085](#)].
- [42] G. D’Ambrosio, G. F. Giudice, G. Isidori and A. Strumia, *Minimal flavor violation: An Effective field theory approach*, *Nucl. Phys.* **B645** (2002) 155–187, [[hep-ph/0207036](#)].
- [43] R. Davis, D. S. Harmer and K. C. Hoffman, *Search for neutrinos from the sun*, *Phys. Rev. Lett.* **20** (May, 1968) 1205–1209.
- [44] SUPER-KAMIOKANDE collaboration, Y. Fukuda et al., *Evidence for oscillation of atmospheric neutrinos*, *Phys. Rev. Lett.* **81** (1998) 1562–1567, [[hep-ex/9807003](#)].
- [45] DOUBLE CHOOZ collaboration, Y. Abe et al., *Indication of Reactor $\bar{\nu}_e$ Disappearance in the Double Chooz Experiment*, *Phys. Rev. Lett.* **108** (2012) 131801, [[1112.6353](#)].
- [46] OPERA collaboration, N. Agafonova et al., *Observation of a first ν_τ candidate in the OPERA experiment in the CNGS beam*, *Phys. Lett.* **B691** (2010) 138–145, [[1006.1623](#)].
- [47] B. Pontecorvo, *Mesonium and anti-mesonium*, *Sov. Phys. JETP* **6** (1957) 429.
- [48] Z. Maki, M. Nakagawa and S. Sakata, *Remarks on the Unified Model of Elementary Particles*, *Progress of Theoretical Physics* **28** (11, 1962) 870–880.

- [49] S. Tremaine and J. E. Gunn, *Dynamical role of light neutral leptons in cosmology*, *Phys. Rev. Lett.* **42** (Feb, 1979) 407–410.
- [50] M. Schwartz, *Quantum Field Theory and the Standard Model*. Quantum Field Theory and the Standard Model. Cambridge University Press, 2014.
- [51] ATLAS collaboration, G. Aad et al., *Observation of a new particle in the search for the Standard Model Higgs boson with the ATLAS detector at the LHC*, *Phys. Lett.* **B716** (2012) 1–29, [1207.7214].
- [52] CMS collaboration, S. Chatrchyan et al., *Observation of a new boson at a mass of 125 GeV with the CMS experiment at the LHC*, *Phys. Lett.* **B716** (2012) 30–61, [1207.7235].
- [53] A. Signer, *ABC of SUSY*, *J. Phys.* **G36** (2009) 073002, [0905.4630].
- [54] G. Jungman, M. Kamionkowski and K. Griest, *Supersymmetric dark matter*, *Phys. Rept.* **267** (1996) 195–373, [hep-ph/9506380].
- [55] S. Weinberg, *A New Light Boson?*, *Phys. Rev. Lett.* **40** (1978) 223–226.
- [56] F. Wilczek, *Problem of Strong P and T Invariance in the Presence of Instantons*, *Phys. Rev. Lett.* **40** (1978) 279–282.
- [57] L. D. Duffy and K. van Bibber, *Axions as Dark Matter Particles*, *New J. Phys.* **11** (2009) 105008, [0904.3346].
- [58] A. D. Sakharov, *Violation of CP in variance, asymmetry, and baryon asymmetry of the universe*, *Soviet Physics Uspekhi* **34** (may, 1991) 392–393.
- [59] K. M. Zurek, *Asymmetric Dark Matter: Theories, Signatures, and Constraints*, *Phys. Rept.* **537** (2014) 91–121, [1308.0338].
- [60] S. Mertens, *Direct Neutrino Mass Experiments*, *J. Phys. Conf. Ser.* **718** (2016) 022013, [1605.01579].

- [61] I. G. McCarthy, S. Bird, J. Schaye, J. Harnois-Deraps, A. S. Font and L. Van Waerbeke, *The BAHAMAS project: the CMB–large-scale structure tension and the roles of massive neutrinos and galaxy formation*, *Mon. Not. Roy. Astron. Soc.* **476** (2018) 2999–3030, [1712.02411].
- [62] P. Gondolo and G. Gelmini, *Cosmic abundances of stable particles: Improved analysis*, *Nucl. Phys.* **B360** (1991) 145–179.
- [63] B. W. Lee and S. Weinberg, *Cosmological lower bound on heavy-neutrino masses*, *Phys. Rev. Lett.* **39** (Jul, 1977) 165–168.
- [64] P. Hut, *Limits on masses and number of neutral weakly interacting particles*, *Physics Letters B* **69** (1977) 85 – 88.
- [65] K. Griest and M. Kamionkowski, *Unitarity Limits on the Mass and Radius of Dark Matter Particles*, *Phys. Rev. Lett.* **64** (1990) 615.
- [66] C. Boehm and P. Fayet, *Scalar dark matter candidates*, *Nucl. Phys.* **B683** (2004) 219–263, [hep-ph/0305261].
- [67] C. M. Ho and R. J. Scherrer, *Anapole Dark Matter*, *Phys. Lett.* **B722** (2013) 341–346, [1211.0503].
- [68] K. Griest and D. Seckel, *Three exceptions in the calculation of relic abundances*, *Phys. Rev. D* **43** (May, 1991) 3191–3203.
- [69] J. McDonald, *Thermally generated gauge singlet scalars as selfinteracting dark matter*, *Phys. Rev. Lett.* **88** (2002) 091304, [hep-ph/0106249].
- [70] L. J. Hall, K. Jedamzik, J. March-Russell and S. M. West, *Freeze-In Production of FIMP Dark Matter*, *JHEP* **03** (2010) 080, [0911.1120].
- [71] S. Heeba, F. Kahlhoefer and P. Stöcker, *Freeze-in production of decaying dark matter in five steps*, *JCAP* **1811** (2018) 048, [1809.04849].

- [72] J. L. Feng, A. Rajaraman and F. Takayama, *Superweakly interacting massive particles*, *Phys. Rev. Lett.* **91** (2003) 011302, [[hep-ph/0302215](#)].
- [73] A. Kusenko, *Sterile neutrinos: The Dark side of the light fermions*, *Phys. Rept.* **481** (2009) 1–28, [[0906.2968](#)].
- [74] M. Drewes et al., *A White Paper on keV Sterile Neutrino Dark Matter*, *JCAP* **1701** (2017) 025, [[1602.04816](#)].
- [75] S. Dodelson and L. M. Widrow, *Sterile-neutrinos as dark matter*, *Phys. Rev. Lett.* **72** (1994) 17–20, [[hep-ph/9303287](#)].
- [76] R. Li, C. S. Frenk, S. Cole, L. Gao, S. Bose and W. A. Hellwing, *Constraints on the identity of the dark matter from strong gravitational lenses*, *Mon. Not. Roy. Astron. Soc.* **460** (2016) 363–372, [[1512.06507](#)].
- [77] R. Li, C. S. Frenk, S. Cole, Q. Wang and L. Gao, *Projection effects in the strong lensing study of subhaloes*, *Mon. Not. Roy. Astron. Soc.* **468** (2017) 1426–1432, [[1612.06227](#)].
- [78] E. W. Kolb, D. J. H. Chung and A. Riotto, *WIMPzillas!*, *AIP Conf. Proc.* **484** (1999) 91–105, [[hep-ph/9810361](#)].
- [79] M. Fairbairn, K. Kainulainen, T. Markkanen and S. Nurmi, *Despicable Dark Relics: generated by gravity with unconstrained masses*, *JCAP* **1904** (2019) 005, [[1808.08236](#)].
- [80] J. Preskill, M. B. Wise and F. Wilczek, *Cosmology of the invisible axion*, *Physics Letters B* **120** (1983) 127 – 132.
- [81] FERMI-LAT collaboration, M. Ackermann et al., *Searching for Dark Matter Annihilation from Milky Way Dwarf Spheroidal Galaxies with Six Years of Fermi Large Area Telescope Data*, *Phys. Rev. Lett.* **115** (2015) 231301, [[1503.02641](#)].

- [82] R. K. Leane and T. R. Slatyer, *Dark Matter Strikes Back at the Galactic Center*, 1904.08430.
- [83] FERMI-LAT collaboration, A. A. Abdo et al., *Observations of Milky Way Dwarf Spheroidal galaxies with the Fermi-LAT detector and constraints on Dark Matter models*, *Astrophys. J.* **712** (2010) 147–158, [1001.4531].
- [84] H.E.S.S. collaboration, A. Abramowski et al., *Search for Photon-Linelike Signatures from Dark Matter Annihilations with H.E.S.S.*, *Phys. Rev. Lett.* **110** (2013) 041301, [1301.1173].
- [85] HAWC collaboration, A. U. Abeysekara et al., *Sensitivity of HAWC to high-mass dark matter annihilations*, *Phys. Rev.* **D90** (2014) 122002, [1405.1730].
- [86] ICECUBE collaboration, M. G. Aartsen et al., *Search for Neutrinos from Dark Matter Self-Annihilations in the center of the Milky Way with 3 years of IceCube/DeepCore*, *Eur. Phys. J.* **C77** (2017) 627, [1705.08103].
- [87] ICECUBE, ANTARES collaboration, J. A. A. Sánchez, N. Iovine, C. Tönnis and J. De Dios Zornoza Gémez, *Combined Search for Neutrinos from Dark Matter Annihilation in the Galactic Center using IceCube and ANTARES*, *PoS ICRC2017* (2018) 911.
- [88] M. Srednicki, K. A. Olive and J. Silk, *High-Energy Neutrinos from the Sun and Cold Dark Matter*, *Nucl. Phys.* **B279** (1987) 804–823.
- [89] A. KOUNINE, *The alpha magnetic spectrometer on the international space station*, *International Journal of Modern Physics E* **21** (2012) 1230005, [<https://doi.org/10.1142/S0218301312300056>].
- [90] PAMELA collaboration, O. Adriani et al., *An anomalous positron abundance in cosmic rays with energies 1.5-100 GeV*, *Nature* **458** (2009) 607–609, [0810.4995].

- [91] ICECUBE collaboration, M. G. Aartsen et al., *Evidence for High-Energy Extraterrestrial Neutrinos at the IceCube Detector*, *Science* **342** (2013) 1242856, [1311.5238].
- [92] T. Daylan, D. P. Finkbeiner, D. Hooper, T. Linden, S. K. N. Portillo, N. L. Rodd et al., *The characterization of the gamma-ray signal from the central Milky Way: A case for annihilating dark matter*, *Phys. Dark Univ.* **12** (2016) 1–23, [1402.6703].
- [93] D. Hooper and L. Goodenough, *Dark Matter Annihilation in The Galactic Center As Seen by the Fermi Gamma Ray Space Telescope*, *Phys. Lett.* **B697** (2011) 412–428, [1010.2752].
- [94] ICECUBE collaboration, M. G. Aartsen et al., *First observation of PeV-energy neutrinos with IceCube*, *Phys. Rev. Lett.* **111** (2013) 021103, [1304.5356].
- [95] ICECUBE collaboration, M. G. Aartsen et al., *Observation of High-Energy Astrophysical Neutrinos in Three Years of IceCube Data*, *Phys. Rev. Lett.* **113** (2014) 101101, [1405.5303].
- [96] ATLAS collaboration, M. Aaboud et al., *Constraints on mediator-based dark matter and scalar dark energy models using $\sqrt{s} = 13$ TeV pp collision data collected by the ATLAS detector*, *JHEP* **05** (2019) 142, [1903.01400].
- [97] CMS collaboration, A. Vartak, *Dark matter search in CMS*, in *Proceedings, 52nd Rencontres de Moriond on Very High Energy Phenomena in the Universe: La Thuile, Italy, March 18-25, 2017*, (Geneva), pp. 225–233, CERN, CERN, 2017.
- [98] O. Buchmueller, M. J. Dolan and C. McCabe, *Beyond Effective Field Theory for Dark Matter Searches at the LHC*, *JHEP* **01** (2014) 025, [1308.6799].
- [99] S. Alekhin et al., *A facility to Search for Hidden Particles at the CERN SPS: the SHiP physics case*, *Rept. Prog. Phys.* **79** (2016) 124201, [1504.04855].

- [100] M. W. Goodman and E. Witten, *Detectability of Certain Dark Matter Candidates*, *Phys. Rev.* **D31** (1985) 3059.
- [101] J. R. Primack, D. Seckel and B. Sadoulet, *Detection of Cosmic Dark Matter*, *Ann. Rev. Nucl. Part. Sci.* **38** (1988) 751–807.
- [102] XENON collaboration, E. Aprile et al., *Dark Matter Search Results from a One Tonne \times Year Exposure of XENON1T*, 1805.12562.
- [103] LUX collaboration, D. S. Akerib et al., *Limits on spin-dependent WIMP-nucleon cross section obtained from the complete LUX exposure*, *Phys. Rev. Lett.* **118** (2017) 251302, [1705.03380].
- [104] PANDAX-II collaboration, X. Cui et al., *Dark Matter Results From 54-Ton-Day Exposure of PandaX-II Experiment*, *Phys. Rev. Lett.* **119** (2017) 181302, [1708.06917].
- [105] DARKSIDE collaboration, P. Agnes et al., *DarkSide-50 532-day Dark Matter Search with Low-Radioactivity Argon*, 1802.07198.
- [106] SUPERCDMS collaboration, R. Agnese et al., *Search for Low-Mass Dark Matter with CDMSlite Using a Profile Likelihood Fit*, 1808.09098.
- [107] CRESST collaboration, F. Petricca et al., *First results on low-mass dark matter from the CRESST-III experiment*, in *15th International Conference on Topics in Astroparticle and Underground Physics (TAUP 2017) Sudbury, Ontario, Canada, July 24-28, 2017*, 2017, 1711.07692, <https://inspirehep.net/record/1637341/files/arXiv:1711.07692.pdf>.
- [108] DAMIC collaboration, A. Aguilar-Arevalo et al., *Search for low-mass WIMPs in a 0.6 kg day exposure of the DAMIC experiment at SNOLAB*, *Phys. Rev.* **D94** (2016) 082006, [1607.07410].

- [109] LUX collaboration, D. S. Akerib et al., *Results from a search for dark matter in the complete LUX exposure*, *Phys. Rev. Lett.* **118** (2017) 021303, [1608.07648].
- [110] LZ collaboration, D. S. Akerib et al., *Projected WIMP sensitivity of the LUX-ZEPLIN (LZ) dark matter experiment*, *Submitted to: Phys. Rev. D.* (2018) , [1802.06039].
- [111] XENON1T collaboration, E. Aprile et al., *Physics reach of the XENON1T dark matter experiment*, *JCAP* **2016** (2016) 36, [1512.07501].
- [112] DARWIN collaboration, J. Aalbers et al., *DARWIN: towards the ultimate dark matter detector*, *JCAP* **1611** (2016) 017, [1606.07001].
- [113] C. E. Aalseth et al., *DarkSide-20k: A 20 tonne two-phase LAr TPC for direct dark matter detection at LNGS*, *Eur. Phys. J. Plus* **133** (2018) 131, [1707.08145].
- [114] DEAP-3600 collaboration, P. A. Amaudruz et al., *First results from the DEAP-3600 dark matter search with argon at SNOLAB*, *Phys. Rev. Lett.* **121** (2018) 071801, [1707.08042].
- [115] DARKSIDE collaboration, P. Agnes et al., *Low-Mass Dark Matter Search with the DarkSide-50 Experiment*, *Phys. Rev. Lett.* **121** (2018) 081307, [1802.06994].
- [116] SUPERCDMS collaboration, K. Schneck et al., *Dark matter effective field theory scattering in direct detection experiments*, *Phys. Rev.* **D91** (2015) 092004, [1503.03379].
- [117] NEWS-G collaboration, Q. Arnaud et al., *First results from the NEWS-G direct dark matter search experiment at the LSM*, *Astropart. Phys.* **97** (2018) 54–62, [1706.04934].

- [118] M. Battaglieri et al., *US Cosmic Visions: New Ideas in Dark Matter 2017: Community Report*, 1707.04591.
- [119] J. Bramante, B. Broerman, R. F. Lang and N. Raj, *Saturated Overburden Scattering and the Multiscatter Frontier: Discovering Dark Matter at the Planck Mass and Beyond*, *Phys. Rev.* **D98** (2018) 083516, [1803.08044].
- [120] D. Carney, S. Ghosh, G. Krnjaic and J. M. Taylor, *Gravitational Direct Detection of Dark Matter*, 1903.00492.
- [121] A. K. Drukier, S. Baum, K. Freese, M. Górski and P. Stengel, *Paleo-detectors: Searching for Dark Matter with Ancient Minerals*, *Phys. Rev.* **D99** (2019) 043014, [1811.06844].
- [122] F. Mayet et al., *A review of the discovery reach of directional Dark Matter detection*, *Phys. Rept.* **627** (2016) 1–49, [1602.03781].
- [123] A. L. Fitzpatrick, W. Haxton, E. Katz, N. Lubbers and Y. Xu, *The Effective Field Theory of Dark Matter Direct Detection*, *JCAP* **1302** (2013) 004, [1203.3542].
- [124] N. Anand, A. L. Fitzpatrick and W. C. Haxton, *Weakly interacting massive particle-nucleus elastic scattering response*, *Phys. Rev.* **C89** (2014) 065501, [1308.6288].
- [125] M. Hoferichter, P. Klos, J. Menéndez and A. Schwenk, *Analysis strategies for general spin-independent WIMP-nucleus scattering*, *Phys. Rev.* **D94** (2016) 063505, [1605.08043].
- [126] D. Gazda, R. Catena and C. Forssén, *Ab initio nuclear response functions for dark matter searches*, *Phys. Rev.* **D95** (2017) 103011, [1612.09165].
- [127] F. Bishara, J. Brod, B. Grinstein and J. Zupan, *From quarks to nucleons in dark matter direct detection*, *JHEP* **11** (2017) 059, [1707.06998].

- [128] J. Fan, M. Reece and L.-T. Wang, *Non-relativistic effective theory of dark matter direct detection*, *JCAP* **1011** (2010) 042, [1008.1591].
- [129] S. Groote and A. A. Pivovarov, *Heavy quark induced effective action for gauge fields in the $SU(N(c)) \times U(1)$ model and the low-energy structure of heavy quark current correlators*, *Eur. Phys. J.* **C21** (2001) 133–143, [hep-ph/0103313].
- [130] M. Shifman, A. Vainshtein and V. Zakharov, *Remarks on higgs-boson interactions with nucleons*, *Physics Letters B* **78** (1978) 443 – 446.
- [131] P. Agrawal, Z. Chacko, C. Kilic and R. K. Mishra, *A Classification of Dark Matter Candidates with Primarily Spin-Dependent Interactions with Matter*, 1003.1912.
- [132] M. E. Peskin and D. V. Schroeder, *An Introduction to quantum field theory*. Addison-Wesley, Reading, USA, 1995.
- [133] E. Del Nobile, *Complete Lorentz-to-Galileo dictionary for direct dark matter detection*, *Phys. Rev.* **D98** (2018) 123003, [1806.01291].
- [134] M. Pospelov and T. ter Veldhuis, *Direct and indirect limits on the electromagnetic form-factors of WIMPs*, *Phys. Lett.* **B480** (2000) 181–186, [hep-ph/0003010].
- [135] K. Sigurdson, M. Doran, A. Kurylov, R. R. Caldwell and M. Kamionkowski, *Dark-matter electric and magnetic dipole moments*, *Phys. Rev. D* **70** (Oct, 2004) 083501.
- [136] V. Barger, W.-Y. Keung and D. Marfatia, *Electromagnetic properties of dark matter: Dipole moments and charge form factor*, *Physics Letters B* **696** (2011) 74 – 78.
- [137] T. Banks, J.-F. Fortin and S. Thomas, *Direct Detection of Dark Matter Electromagnetic Dipole Moments*, 1007.5515.

- [138] N. Weiner and I. Yavin, *Uv completions of magnetic inelastic and rayleigh dark matter for the fermi line(s)*, *Phys. Rev. D* **87** (Jan, 2013) 023523.
- [139] M. T. Frandsen, U. Haisch, F. Kahlhoefer, P. Mertsch and K. Schmidt-Hoberg, *Loop-induced dark matter direct detection signals from gamma-ray lines*, *JCAP* **1210** (2012) 033, [1207.3971].
- [140] M. I. Gresham and K. M. Zurek, *Effect of nuclear response functions in dark matter direct detection*, *Phys. Rev.* **D89** (2014) 123521, [1401.3739].
- [141] C. Savage, G. Gelmini, P. Gondolo and K. Freese, *Compatibility of DAMA/LIBRA dark matter detection with other searches*, *JCAP* **0904** (2009) 010, [0808.3607].
- [142] DAMA, LIBRA collaboration, R. Bernabei et al., *New results from DAMA/LIBRA*, *Eur. Phys. J.* **C67** (2010) 39–49, [1002.1028].
- [143] S. Kang, S. Scopel and G. Tomar, *Probing DAMA/LIBRA data in the full parameter space of WIMP effective models of inelastic scattering*, *Phys. Rev.* **D99** (2019) 103019, [1902.09121].
- [144] S. Kang, S. Scopel, G. Tomar, J.-H. Yoon and P. Gondolo, *Anapole Dark Matter after DAMA/LIBRA-phase2*, *JCAP* **1811** (2018) 040, [1808.04112].
- [145] J. Amaré et al., *First Results on Dark Matter Annual Modulation from the ANAIS-112 Experiment*, *Phys. Rev. Lett.* **123** (2019) 031301, [1903.03973].
- [146] COSINE-100 collaboration, G. Adhikari et al., *Search for a Dark Matter-Induced Annual Modulation Signal in NaI(Tl) with the COSINE-100 Experiment*, *Phys. Rev. Lett.* **123** (2019) 031302, [1903.10098].
- [147] J. Billard, L. Strigari and E. Figueroa-Feliciano, *Implication of neutrino backgrounds on the reach of next generation dark matter direct detection experiments*, *Phys. Rev.* **D89** (2014) 023524, [1307.5458].

- [148] T. K. Gaisser and M. Honda, *Flux of atmospheric neutrinos*, *Ann. Rev. Nucl. Part. Sci.* **52** (2002) 153–199, [[hep-ph/0203272](#)].
- [149] G. Battistoni, A. Ferrari, T. Montaruli and P. R. Sala, *The atmospheric neutrino flux below 100-MeV: The FLUKA results*, *Astropart. Phys.* **23** (2005) 526–534.
- [150] S. Horiuchi, J. F. Beacom and E. Dwek, *The Diffuse Supernova Neutrino Background is detectable in Super-Kamiokande*, *Phys. Rev.* **D79** (2009) 083013, [[0812.3157](#)].
- [151] A. M. Serenelli, W. C. Haxton and C. Pena-Garay, *Solar models with accretion. I. Application to the solar abundance problem*, *Astrophys. J.* **743** (2011) 24, [[1104.1639](#)].
- [152] G. B. Gelmini, V. Takhistov and S. J. Witte, *Casting a Wide Signal Net with Future Direct Dark Matter Detection Experiments*, *JCAP* **1807** (2018) 009, [[1804.01638](#)].
- [153] K. Freese, M. Lisanti and C. Savage, *Colloquium: Annual modulation of dark matter*, *Rev. Mod. Phys.* **85** (2013) 1561–1581, [[1209.3339](#)].
- [154] PICO collaboration, C. Amole et al., *Dark Matter Search Results from the PICO-60 C₃F₈ Bubble Chamber*, *Phys. Rev. Lett.* **118** (2017) 251301, [[1702.07666](#)].
- [155] SUPER-KAMIOKANDE collaboration, K. Choi et al., *Search for neutrinos from annihilation of captured low-mass dark matter particles in the Sun by Super-Kamiokande*, *Phys. Rev. Lett.* **114** (2015) 141301, [[1503.04858](#)].
- [156] ICECUBE collaboration, M. G. Aartsen et al., *Search for annihilating dark matter in the Sun with 3 years of IceCube data*, *Eur. Phys. J.* **C77** (2017) 146, [[1612.05949](#)].

- [157] A. M. Green, *Determining the WIMP mass using direct detection experiments*, *JCAP* **0708** (2007) 022, [[hep-ph/0703217](#)].
- [158] A. M. Green, *Determining the WIMP mass from a single direct detection experiment, a more detailed study*, *JCAP* **0807** (2008) 005, [[0805.1704](#)].
- [159] S. D. McDermott, H.-B. Yu and K. M. Zurek, *The Dark Matter Inverse Problem: Extracting Particle Physics from Scattering Events*, *Phys. Rev.* **D85** (2012) 123507, [[1110.4281](#)].
- [160] S. Yellin, *Finding an upper limit in the presence of an unknown background*, *Physical Review D* **66** (Aug, 2002) 032005, [[physics/0203002](#)].
- [161] A. M. Green, *Astrophysical uncertainties on direct detection experiments*, *Mod. Phys. Lett.* **A27** (2012) 1230004, [[1112.0524](#)].
- [162] D. G. Cerdeno, M. Fornasa, J. H. Huh and M. Peiro, *Nuclear uncertainties in the spin-dependent structure functions for direct dark matter detection*, *Phys. Rev.* **D87** (2013) 023512, [[1208.6426](#)].
- [163] G. Bertone, D. G. Cerdeno, J. I. Collar and B. C. Odom, *WIMP identification through a combined measurement of axial and scalar couplings*, *Phys. Rev. Lett.* **99** (2007) 151301, [[0705.2502](#)].
- [164] M. Pato, L. Baudis, G. Bertone, R. Ruiz de Austri, L. E. Strigari and R. Trotta, *Complementarity of Dark Matter Direct Detection Targets*, *Phys. Rev.* **D83** (2011) 083505, [[1012.3458](#)].
- [165] D. G. Cerdeño et al., *Complementarity of dark matter direct detection: the role of bolometric targets*, *JCAP* **1307** (2013) 028, [[1304.1758](#)].
- [166] A. H. G. Peter, V. Gluscevic, A. M. Green, B. J. Kavanagh and S. K. Lee, *WIMP physics with ensembles of direct-detection experiments*, *Phys. Dark Univ.* **5-6** (2014) 45–74, [[1310.7039](#)].

- [167] R. Catena and P. Gondolo, *Global fits of the dark matter-nucleon effective interactions*, *JCAP* **1409** (2014) 045, [1405.2637].
- [168] F. Kahlhoefer, S. Kulkarni and S. Wild, *Exploring light mediators with low-threshold direct detection experiments*, *JCAP* **1711** (2017) 016, [1707.08571].
- [169] C. Streve, R. Trotta, G. Bertone, A. H. G. Peter and P. Scott, *Fundamental statistical limitations of future dark matter direct detection experiments*, *Phys. Rev.* **D86** (2012) 023507, [1201.3631].
- [170] R. Catena, *Analysis of the theoretical bias in dark matter direct detection*, *JCAP* **1409** (2014) 049, [1407.0127].
- [171] V. Gluscevic, M. I. Gresham, S. D. McDermott, A. H. G. Peter and K. M. Zurek, *Identifying the Theory of Dark Matter with Direct Detection*, *JCAP* **1512** (2015) 057, [1506.04454].
- [172] F. S. Queiroz, W. Rodejohann and C. E. Yaguna, *Is the dark matter particle its own antiparticle?*, *Phys. Rev.* **D95** (2017) 095010, [1610.06581].
- [173] B. J. Kavanagh, F. S. Queiroz, W. Rodejohann and C. E. Yaguna, *Prospects for determining the particle/antiparticle nature of WIMP dark matter with direct detection experiments*, *JHEP* **10** (2017) 059, [1706.07819].
- [174] V. Gluscevic and A. H. G. Peter, *Understanding WIMP-baryon interactions with direct detection: A Roadmap*, *JCAP* **1409** (2014) 040, [1406.7008].
- [175] R. Catena, *Prospects for direct detection of dark matter in an effective theory approach*, *JCAP* **1407** (2014) 055, [1406.0524].
- [176] G. Cowan, *Statistical data analysis*. 1998.
- [177] B. J. Kavanagh, P. Panci and R. Ziegler, *Faint Light from Dark Matter: Classifying and Constraining Dark Matter-Photon Effective Operators*, *JHEP* **04** (2019) 089, [1810.00033].

- [178] P. Athron, J. M. Cornell, F. Kahlhoefer, J. McKay, P. Scott and S. Wild, *Impact of vacuum stability, perturbativity and XENON1T on global fits of \mathbb{Z}_2 and \mathbb{Z}_3 scalar singlet dark matter*, *Eur. Phys. J.* **C78** (2018) 830, [1806.11281].
- [179] PARTICLE DATA GROUP collaboration, C. Patrignani et al., *Review of Particle Physics*, *Chin. Phys.* **C40** (2016) 100001.
- [180] A. Fowlie and M. H. Bardsley, *Superplot: a graphical interface for plotting and analysing MultiNest output*, *Eur. Phys. J. Plus* **131** (2016) 391, [1603.00555].
- [181] A. K. Drukier, K. Freese and D. N. Spergel, *Detecting Cold Dark Matter Candidates*, *Phys. Rev.* **D33** (1986) 3495–3508.
- [182] K. Freese, J. Frieman and A. Gould, *Signal modulation in cold-dark-matter detection*, *Phys. Rev. D* **37** (Jun, 1988) 3388–3405.
- [183] C. McCabe, *Aspects of Dark Matter Phenomenology*, Ph.D. thesis, Oxford U., 2011.
- [184] N. W. Evans, C. M. Carollo and P. T. de Zeeuw, *Triaxial haloes and particle dark matter detection*, *Mon. Not. Roy. Astron. Soc.* **318** (2000) 1131, [astro-ph/0008156].
- [185] M. Fairbairn and T. Schwetz, *Spin-independent elastic WIMP scattering and the DAMA annual modulation signal*, *JCAP* **0901** (2009) 037, [0808.0704].
- [186] J. March-Russell, C. McCabe and M. McCullough, *Inelastic Dark Matter, Non-Standard Halos and the DAMA/LIBRA Results*, *JHEP* **05** (2009) 071, [0812.1931].
- [187] N. Bozorgnia, R. Catena and T. Schwetz, *Anisotropic dark matter distribution functions and impact on WIMP direct detection*, *JCAP* **1312** (2013) 050, [1310.0468].

- [188] C. Savage, K. Freese and P. Gondolo, *Annual modulation of dark matter in the presence of streams*, *Phys. Rev. D* **74** (Aug, 2006) 043531.
- [189] M. Fornasa and A. M. Green, *Self-consistent phase-space distribution function for the anisotropic dark matter halo of the Milky Way*, *Phys. Rev.* **D89** (2014) 063531, [1311.5477].
- [190] C. W. Purcell, A. R. Zentner and M.-Y. Wang, *Dark matter direct search rates in simulations of the milky way and sagittarius stream*, *Journal of Cosmology and Astroparticle Physics* **2012** (aug, 2012) 027–027.
- [191] M. Vogelsberger, A. Helmi, V. Springel, S. D. M. White, J. Wang, C. S. Frenk et al., *Phase-space structure in the local dark matter distribution and its signature in direct detection experiments*, *Mon. Not. Roy. Astron. Soc.* **395** (2009) 797–811, [0812.0362].
- [192] F. S. Ling, E. Nezri, E. Athanassoula and R. Teyssier, *Dark Matter Direct Detection Signals inferred from a Cosmological N-body Simulation with Baryons*, *JCAP* **1002** (2010) 012, [0909.2028].
- [193] M. Kuhlen, N. Weiner, J. Diemand, P. Madau, B. Moore, D. Potter et al., *Dark Matter Direct Detection with Non-Maxwellian Velocity Structure*, *JCAP* **1002** (2010) 030, [0912.2358].
- [194] M. Lisanti, L. E. Strigari, J. G. Wacker and R. H. Wechsler, *The Dark Matter at the End of the Galaxy*, *Phys. Rev.* **D83** (2011) 023519, [1010.4300].
- [195] G. Gelmini and P. Gondolo, *WIMP annual modulation with opposite phase in Late-Infall halo models*, *Phys. Rev.* **D64** (2001) 023504, [hep-ph/0012315].
- [196] N. Bozorgnia, F. Calore, M. Schaller, M. Lovell, G. Bertone, C. S. Frenk et al., *Simulated Milky Way analogues: implications for dark matter direct searches*, *JCAP* **1605** (2016) 024, [1601.04707].

- [197] R. Catena and P. Ullio, *A novel determination of the local dark matter density*, *JCAP* **1008** (2010) 004, [0907.0018].
- [198] P. Salucci, F. Nesti, G. Gentile and C. F. Martins, *The dark matter density at the Sun's location*, *Astron. Astrophys.* **523** (2010) A83, [1003.3101].
- [199] M. Pato, O. Agertz, G. Bertone, B. Moore and R. Teyssier, *Systematic uncertainties in the determination of the local dark matter density*, *Phys. Rev.* **D82** (2010) 023531, [1006.1322].
- [200] F. Iocco, M. Pato, G. Bertone and P. Jetzer, *Dark Matter distribution in the Milky Way: microlensing and dynamical constraints*, *JCAP* **1111** (2011) 029, [1107.5810].
- [201] F. Calore, N. Bozorgnia, M. Lovell, G. Bertone, M. Schaller, C. S. Frenk et al., *Simulated Milky Way analogues: implications for dark matter indirect searches*, *JCAP* **1512** (2015) 053, [1509.02164].
- [202] J. F. Navarro, C. S. Frenk and S. D. M. White, *The Structure of cold dark matter halos*, *Astrophys. J.* **462** (1996) 563–575, [astro-ph/9508025].
- [203] J. Diemand, M. Kuhlen, P. Madau, M. Zemp, B. Moore, D. Potter et al., *Clumps and streams in the local dark matter distribution*, *Nature* **454** (2008) 735–738, [0805.1244].
- [204] V. Springel, J. Wang, M. Vogelsberger, A. Ludlow, A. Jenkins, A. Helmi et al., *The Aquarius Project: the subhalos of galactic halos*, *Mon. Not. Roy. Astron. Soc.* **391** (2008) 1685–1711, [0809.0898].
- [205] J. Stadel, D. Potter, B. Moore, J. Diemand, P. Madau, M. Zemp et al., *Quantifying the heart of darkness with GHALO - a multi-billion particle simulation of our galactic halo*, *Mon. Not. Roy. Astron. Soc.* **398** (2009) L21–L25, [0808.2981].

- [206] S. H. Hansen, B. Moore, M. Zemp and J. Stadel, *A Universal velocity distribution of relaxed collisionless structures*, *JCAP* **0601** (2006) 014, [astro-ph/0505420].
- [207] A. D. Ludlow, J. F. Navarro, M. Boylan-Kolchin, V. Springel, A. Jenkins, C. S. Frenk et al., *The density and pseudo-phase-space density profiles of cold dark matter haloes*, *Mon. Not. Roy. Astron. Soc.* **415** (2011) 3895–3902, [1102.0002].
- [208] Y.-Y. Mao, L. E. Strigari, R. H. Wechsler, H.-Y. Wu and O. Hahn, *Halo-to-Halo Similarity and Scatter in the Velocity Distribution of Dark Matter*, *Astrophys. J.* **764** (2013) 35, [1210.2721].
- [209] M. Kuhlen, A. Pillepich, J. Guedes and P. Madau, *The Distribution of Dark Matter in the Milky Way’s Disk*, *Astrophys. J.* **784** (2014) 161, [1308.1703].
- [210] Gaia Collaboration, A. G. A. Brown, A. Vallenari, T. Prusti, J. H. J. de Bruijne, C. Babusiaux et al., *Gaia Data Release 2. Summary of the contents and survey properties*, *Astronomy & Astrophysics* **616** (Aug, 2018) A1, [1804.09365].
- [211] C. A. J. O’Hare, C. McCabe, N. W. Evans, G. Myeong and V. Belokurov, *Dark matter hurricane: Measuring the S1 stream with dark matter detectors*, *Phys. Rev.* **D98** (2018) 103006, [1807.09004].
- [212] N. W. Evans, C. A. J. O’Hare and C. McCabe, *Refinement of the standard halo model for dark matter searches in light of the Gaia Sausage*, *Phys. Rev.* **D99** (2019) 023012, [1810.11468].
- [213] K. Schneck, *Search for Low-Mass Dark Matter with SuperCDMS Soudan and Study of Shorted Electric Field Configurations in CDMS Detectors*, Ph.D. thesis, Stanford U., 2015. 10.2172/1352049.

- [214] S. J. Witte, V. Gluscevic and S. D. McDermott, *Prospects for Distinguishing Dark Matter Models Using Annual Modulation*, *JCAP* **1702** (2017) 044, [1612.07808].
- [215] R. Catena, J. Conrad, C. Döring, A. D. Ferella and M. B. Krauss, *Dark matter spin determination with directional direct detection experiments*, *Phys. Rev.* **D97** (2018) 023007, [1706.09471].
- [216] S. Baum, R. Catena, J. Conrad, K. Freese and M. B. Krauss, *Determining Dark Matter properties with a XENONnT/LZ signal and LHC-Run3 mono-jet searches*, 1709.06051.
- [217] R. Bellman, R. Corporation and K. M. R. Collection, *Dynamic Programming*. Rand Corporation research study. Princeton University Press, 1957.
- [218] H. Rogers, D. G. Cerdeno, P. Cushman, F. Livet and V. Mandic, *Multidimensional effective field theory analysis for direct detection of dark matter*, *Phys. Rev.* **D95** (2017) 082003, [1612.09038].
- [219] R. Catena and P. Gondolo, *Global limits and interference patterns in dark matter direct detection*, *JCAP* **1508** (2015) 022, [1504.06554].
- [220] J. B. Dent, L. M. Krauss, J. L. Newstead and S. Sabharwal, *General analysis of direct dark matter detection: From microphysics to observational signatures*, *Phys. Rev.* **D92** (2015) 063515, [1505.03117].
- [221] J. Abdallah et al., *Simplified Models for Dark Matter Searches at the LHC*, *Phys. Dark Univ.* **9-10** (2015) 8–23, [1506.03116].
- [222] R. Catena, K. Fridell and M. B. Krauss, *Non-relativistic Effective Interactions of Spin 1 Dark Matter*, *JHEP* **08** (2019) 030, [1907.02910].
- [223] A. Buckley, H. Hoeth, H. Lacker, H. Schulz and J. E. von Seggern, *Systematic event generator tuning for the LHC*, *Eur. Phys. J.* **C65** (2010) 331–357, [0907.2973].

- [224] DELPHI collaboration, P. Abreu et al., *Tuning and test of fragmentation models based on identified particles and precision event shape data*, *Z. Phys.* **C73** (1996) 11–60.
- [225] C. Englert, R. Kogler, H. Schulz and M. Spannowsky, *Higgs characterisation in the presence of theoretical uncertainties and invisible decays*, *Eur. Phys. J.* **C77** (2017) 789, [1708.06355].
- [226] A. Buckley, C. Englert, J. Ferrando, D. J. Miller, L. Moore, M. Russell et al., *Constraining top quark effective theory in the LHC Run II era*, *JHEP* **04** (2016) 015, [1512.03360].
- [227] C. Englert, R. Kogler, H. Schulz and M. Spannowsky, *Higgs coupling measurements at the LHC*, *Eur. Phys. J.* **C76** (2016) 393, [1511.05170].
- [228] F. Feroz, M. P. Hobson and M. Bridges, *MultiNest: an efficient and robust Bayesian inference tool for cosmology and particle physics*, *Mon. Not. Roy. Astron. Soc.* **398** (2009) 1601–1614, [0809.3437].
- [229] F. Feroz and M. P. Hobson, *Multimodal nested sampling: an efficient and robust alternative to MCMC methods for astronomical data analysis*, *Mon. Not. Roy. Astron. Soc.* **384** (2008) 449, [0704.3704].
- [230] SUPERCDMS collaboration, R. Agnese et al., *Projected Sensitivity of the SuperCDMS SNOLAB experiment*, *Phys. Rev.* **D95** (2017) 082002, [1610.00006].
- [231] LZ collaboration, D. S. Akerib et al., *LUX-ZEPLIN (LZ) Conceptual Design Report*, 1509.02910.
- [232] XENON collaboration, E. Aprile et al., *The XENON1T Dark Matter Experiment*, *Eur. Phys. J.* **C77** (2017) 881, [1708.07051].

- [233] F. Feroz, K. Cranmer, M. Hobson, R. Ruiz de Austri and R. Trotta, *Challenges of Profile Likelihood Evaluation in Multi-Dimensional SUSY Scans*, *JHEP* **06** (2011) 042, [1101.3296].
- [234] J. D. Lewin and P. F. Smith, *Review of mathematics, numerical factors, and corrections for dark matter experiments based on elastic nuclear recoil*, *Astropart. Phys.* **6** (1996) 87–112.
- [235] A. Kurylov and M. Kamionkowski, *Generalized analysis of weakly interacting massive particle searches*, *Phys. Rev.* **D69** (2004) 063503, [hep-ph/0307185].
- [236] F. Giuliani, *Are direct search experiments sensitive to all spin-independent WIMP candidates?*, *Phys. Rev. Lett.* **95** (2005) 101301, [hep-ph/0504157].
- [237] S. Chang, J. Liu, A. Pierce, N. Weiner and I. Yavin, *CoGeNT Interpretations*, *JCAP* **1008** (2010) 018, [1004.0697].
- [238] J. L. Feng, J. Kumar, D. Marfatia and D. Sanford, *Isospin-Violating Dark Matter*, *Phys. Lett.* **B703** (2011) 124–127, [1102.4331].
- [239] C. E. Yaguna, *Isospin-violating dark matter in the light of recent data*, *Phys. Rev.* **D95** (2017) 055015, [1610.08683].
- [240] P. Belli, R. Cerulli, N. Fornengo and S. Scopel, *Effect of the galactic halo modeling on the DAMA / NaI annual modulation result: an Extended analysis of the data for WIMPs with a purely spin independent coupling*, *Phys. Rev.* **D66** (2002) 043503, [hep-ph/0203242].
- [241] D. G. Cerdeno, M. Fornasa, A. M. Green and M. Peiro, *How to calculate dark matter direct detection exclusion limits that are consistent with gamma rays from annihilation in the Milky Way halo*, *Phys. Rev.* **D94** (2016) 043516, [1605.05185].

- [242] N. Bozorgnia and G. Bertone, *Implications of hydrodynamical simulations for the interpretation of direct dark matter searches*, *Int. J. Mod. Phys. A* **32** (2017) , [1705.05853].
- [243] C. McCabe, *The Astrophysical Uncertainties Of Dark Matter Direct Detection Experiments*, *Phys. Rev. D* **82** (2010) 023530, [1005.0579].
- [244] G. Bertone, N. Bozorgnia, J. S. Kim, S. Liem, C. McCabe, S. Otten et al., *Identifying WIMP dark matter from particle and astroparticle data*, 1712.04793.
- [245] D. Tucker-Smith and N. Weiner, *Inelastic dark matter*, *Phys. Rev. D* **64** (2001) 043502, [hep-ph/0101138].
- [246] P. W. Graham, R. Harnik, S. Rajendran and P. Saraswat, *Exothermic Dark Matter*, *Phys. Rev. D* **82** (2010) 063512, [1004.0937].
- [247] K. R. Dienes, J. Kumar, B. Thomas and D. Yaylali, *Dark-Matter Decay as a Complementary Probe of Multicomponent Dark Sectors*, *Phys. Rev. Lett.* **114** (2015) 051301, [1406.4868].
- [248] J. Bramante, P. J. Fox, G. D. Kribs and A. Martin, *Inelastic frontier: Discovering dark matter at high recoil energy*, *Phys. Rev. D* **94** (2016) 115026, [1608.02662].
- [249] G. Barello, S. Chang and C. A. Newby, *A Model Independent Approach to Inelastic Dark Matter Scattering*, *Phys. Rev. D* **90** (2014) 094027, [1409.0536].
- [250] XENON collaboration, E. Aprile et al., *Effective field theory search for high-energy nuclear recoils using the XENON100 dark matter detector*, *Phys. Rev. D* **96** (2017) 042004, [1705.02614].

- [251] A. H. G. Peter, *WIMP astronomy and particle physics with liquid-noble and cryogenic direct-detection experiments*, *Phys. Rev.* **D83** (2011) 125029, [1103.5145].
- [252] D. Mei and A. Hime, *Muon-induced background study for underground laboratories*, *Phys. Rev.* **D73** (2006) 053004, [astro-ph/0512125].
- [253] LUX collaboration, D. S. Akerib et al., *Low-energy (0.7-74 keV) nuclear recoil calibration of the LUX dark matter experiment using D-D neutron scattering kinematics*, 1608.05381.
- [254] S. Polosatkin, E. Grishnyaev and A. Dolgov, *Liquid Argon Cryogenic Detector Calibration by Inelastic Scattering of Neutrons*, 1407.2718.
- [255] L. Vietze, P. Klos, J. Menéndez, W. C. Haxton and A. Schwenk, *Nuclear structure aspects of spin-independent WIMP scattering off xenon*, *Phys. Rev.* **D91** (2015) 043520, [1412.6091].
- [256] F. Bishara, J. Brod, B. Grinstein and J. Zupan, *Chiral Effective Theory of Dark Matter Direct Detection*, *JCAP* **1702** (2017) 009, [1611.00368].
- [257] M. Hoferichter, P. Klos and A. Schwenk, *Chiral power counting of one- and two-body currents in direct detection of dark matter*, *Phys. Lett.* **B746** (2015) 410–416, [1503.04811].
- [258] J. R. Ellis, R. A. Flores and J. D. Lewin, *Rates for Inelastic Nuclear Excitation by Dark Matter Particles*, *Phys. Lett.* **B212** (1988) 375–380.
- [259] C. McCabe, *Prospects for dark matter detection with inelastic transitions of xenon*, *JCAP* **1605** (2016) 033, [1512.00460].
- [260] P. Klos, J. Menéndez, D. Gazit and A. Schwenk, *Large-scale nuclear structure calculations for spin-dependent WIMP scattering with chiral effective field theory currents*, *Phys. Rev.* **D88** (2013) 083516, [1304.7684].

- [261] L. Baudis, G. Kessler, P. Klos, R. F. Lang, J. Menéndez, S. Reichard et al., *Signatures of Dark Matter Scattering Inelastically Off Nuclei*, *Phys. Rev.* **D88** (2013) 115014, [1309.0825].
- [262] C. Kelso, C. Savage, M. Valluri, K. Freese, G. S. Stinson and J. Bailin, *The impact of baryons on the direct detection of dark matter*, *JCAP* **1608** (2016) 071, [1601.04725].
- [263] J. D. Sloane, M. R. Buckley, A. M. Brooks and F. Governato, *Assessing Astrophysical Uncertainties in Direct Detection with Galaxy Simulations*, *Astrophys. J.* **831** (2016) 93, [1601.05402].
- [264] T. D. P. Edwards, B. J. Kavanagh and C. Weniger, *Assessing Near-Future Direct Dark Matter Searches with Benchmark-Free Forecasting*, *Phys. Rev. Lett.* **121** (2018) 181101, [1805.04117].
- [265] LHCb collaboration, R. Aaij et al., *Differential branching fractions and isospin asymmetries of $B \rightarrow K^{(*)}\mu^+\mu^-$ decays*, *JHEP* **06** (2014) 133, [1403.8044].
- [266] LHCb collaboration, R. Aaij et al., *Angular analysis and differential branching fraction of the decay $B_s^0 \rightarrow \phi\mu^+\mu^-$* , *JHEP* **09** (2015) 179, [1506.08777].
- [267] G. Hiller and F. Kruger, *More model-independent analysis of $b \rightarrow s$ processes*, *Phys. Rev.* **D69** (2004) 074020, [hep-ph/0310219].
- [268] M. Bordone, G. Isidori and A. Pattori, *On the Standard Model predictions for R_K and R_{K^*}* , *Eur. Phys. J.* **C76** (2016) 440, [1605.07633].
- [269] BELLE collaboration, J. T. Wei et al., *Measurement of the Differential Branching Fraction and Forward-Backward Asymmetry for $B \rightarrow K^{(*)}\ell^+\ell^-$* , *Phys. Rev. Lett.* **103** (2009) 171801, [0904.0770].

- [270] CMS collaboration, V. Khachatryan et al., *Angular analysis of the decay $B^0 \rightarrow K^{*0}\mu^+\mu^-$ from pp collisions at $\sqrt{s} = 8$ TeV*, *Phys. Lett.* **B753** (2016) 424–448, [1507.08126].
- [271] BELLE collaboration, A. Abdesselam et al., *Angular analysis of $B^0 \rightarrow K^*(892)^0\ell^+\ell^-$* , in *Proceedings, LHCSki 2016 - A First Discussion of 13 TeV Results: Obergurgl, Austria, April 10-15, 2016*, 2016, 1604.04042.
- [272] BABAR collaboration, J. P. Lees et al., *Measurement of angular asymmetries in the decays $B \rightarrow K^*\ell^+\ell^-$* , *Phys. Rev.* **D93** (2016) 052015, [1508.07960].
- [273] CMS collaboration, A. M. Sirunyan et al., *Measurement of angular parameters from the decay $B^0 \rightarrow K^{*0}\mu^+\mu^-$ in proton-proton collisions at $\sqrt{s} = 8$ TeV*, *Phys. Lett.* **B781** (2018) 517–541, [1710.02846].
- [274] ATLAS collaboration, M. Aaboud et al., *Angular analysis of $B_d^0 \rightarrow K^*\mu^+\mu^-$ decays in pp collisions at $\sqrt{s} = 8$ TeV with the ATLAS detector*, *JHEP* **10** (2018) 047, [1805.04000].
- [275] BELLE collaboration, S. Wehle et al., *Lepton-Flavor-Dependent Angular Analysis of $B \rightarrow K^*\ell^+\ell^-$* , *Phys. Rev. Lett.* **118** (2017) 111801, [1612.05014].
- [276] CDF collaboration, T. Aaltonen et al., *Measurements of the Angular Distributions in the Decays $B \rightarrow K^{(*)}\mu^+\mu^-$ at CDF*, *Phys. Rev. Lett.* **108** (2012) 081807, [1108.0695].
- [277] LHCb collaboration, R. Aaij et al., *Angular analysis of the $B^0 \rightarrow K^{*0}\mu^+\mu^-$ decay using 3 fb^{-1} of integrated luminosity*, *JHEP* **02** (2016) 104, [1512.04442].
- [278] B. Gripaios, M. Nardecchia and S. A. Renner, *Linear flavour violation and anomalies in B physics*, *JHEP* **06** (2016) 083, [1509.05020].
- [279] P. Arnan, L. Hofer, F. Mescia and A. Crivellin, *Loop effects of heavy new scalars and fermions in $b \rightarrow s\mu^+\mu^-$* , *JHEP* **04** (2017) 043, [1608.07832].

- [280] A. J. Buras and J. Girrbach, *Left-handed Z' and Z FCNC quark couplings facing new $b \rightarrow s\mu^+\mu^-$ data*, *JHEP* **12** (2013) 009, [1309.2466].
- [281] R. Gauld, F. Goertz and U. Haisch, *An explicit Z' -boson explanation of the $B \rightarrow K^*\mu^+\mu^-$ anomaly*, *JHEP* **01** (2014) 069, [1310.1082].
- [282] M. Bauer and M. Neubert, *Minimal Leptoquark Explanation for the $R_{D^{(*)}}$, R_K , and $(g-2)_g$ Anomalies*, *Phys. Rev. Lett.* **116** (2016) 141802, [1511.01900].
- [283] A. Angelescu, D. Bečirević, D. A. Faroughy and O. Sumensari, *Closing the window on single leptoquark solutions to the B -physics anomalies*, *JHEP* **10** (2018) 183, [1808.08179].
- [284] B. Capdevila, A. Crivellin, S. Descotes-Genon, J. Matias and J. Virto, *Patterns of New Physics in $b \rightarrow s\ell^+\ell^-$ transitions in the light of recent data*, *JHEP* **01** (2018) 093, [1704.05340].
- [285] A. Vicente, *Anomalies in $b \rightarrow s$ transitions and dark matter*, *Adv. High Energy Phys.* **2018** (2018) 3905848, [1803.04703].
- [286] D. Aristizabal Sierra, F. Staub and A. Vicente, *Shedding light on the $b \rightarrow s$ anomalies with a dark sector*, *Phys. Rev.* **D92** (2015) 015001, [1503.06077].
- [287] G. Bélanger, C. Delaunay and S. Westhoff, *A Dark Matter Relic From Muon Anomalies*, *Phys. Rev.* **D92** (2015) 055021, [1507.06660].
- [288] W. Altmannshofer, S. Gori, S. Profumo and F. S. Queiroz, *Explaining dark matter and B decay anomalies with an $L_\mu - L_\tau$ model*, *JHEP* **12** (2016) 106, [1609.04026].
- [289] A. Celis, W.-Z. Feng and M. Vollmann, *Dirac dark matter and $b \rightarrow s\ell^+\ell^-$ with $U(1)$ gauge symmetry*, *Phys. Rev.* **D95** (2017) 035018, [1608.03894].

- [290] J. M. Cline, J. M. Cornell, D. London and R. Watanabe, *Hidden sector explanation of B -decay and cosmic ray anomalies*, *Phys. Rev.* **D95** (2017) 095015, [1702.00395].
- [291] P. Ko, T. Nomura and H. Okada, *Explaining $B \rightarrow K^{(*)}\ell^+\ell^-$ anomaly by radiatively induced coupling in $U(1)_{\mu-\tau}$ gauge symmetry*, *Phys. Rev.* **D95** (2017) 111701, [1702.02699].
- [292] J. Ellis, M. Fairbairn and P. Tunney, *Anomaly-Free Models for Flavour Anomalies*, *Eur. Phys. J.* **C78** (2018) 238, [1705.03447].
- [293] S. Baek, *Dark matter contribution to $b \rightarrow s\mu^+\mu^-$ anomaly in local $U(1)_{L_\mu-L_\tau}$ model*, *Phys. Lett.* **B781** (2018) 376–382, [1707.04573].
- [294] K. Fuyuto, H.-L. Li and J.-H. Yu, *Implications of hidden gauged $U(1)$ model for B anomalies*, *Phys. Rev.* **D97** (2018) 115003, [1712.06736].
- [295] P. Cox, C. Han and T. T. Yanagida, *Right-handed Neutrino Dark Matter in a $U(1)$ Extension of the Standard Model*, *JCAP* **1801** (2018) 029, [1710.01585].
- [296] A. Falkowski, S. F. King, E. Perdomo and M. Pierre, *Flavourful Z' portal for vector-like neutrino Dark Matter and $R_{K^{(*)}}$* , *JHEP* **08** (2018) 061, [1803.04430].
- [297] L. Darmé, K. Kowalska, L. Roszkowski and E. M. Sessolo, *Flavor anomalies and dark matter in SUSY with an extra $U(1)$* , *JHEP* **10** (2018) 052, [1806.06036].
- [298] S. Singirala, S. Sahoo and R. Mohanta, *Exploring dark matter, neutrino mass and $R_{K^{(*)},\phi}$ anomalies in $L_\mu - L_\tau$ model*, *Phys. Rev.* **D99** (2019) 035042, [1809.03213].
- [299] S. Baek and C. Yu, *Dark matter for $b \rightarrow s\mu^+\mu^-$ anomaly in a gauged $U(1)_X$ model*, *JHEP* **11** (2018) 054, [1806.05967].

- [300] A. Kamada, M. Yamada and T. T. Yanagida, *Self-interacting dark matter with a vector mediator: kinetic mixing with the $U(1)_{(B-L)_3}$ gauge boson*, *JHEP* **03** (2019) 021, [1811.02567].
- [301] C. Hati, G. Kumar, J. Orloff and A. M. Teixeira, *Reconciling B -meson decay anomalies with neutrino masses, dark matter and constraints from flavour violation*, *JHEP* **11** (2018) 011, [1806.10146].
- [302] S.-M. Choi, Y.-J. Kang, H. M. Lee and T.-G. Ro, *Lepto-Quark Portal Dark Matter*, *JHEP* **10** (2018) 104, [1807.06547].
- [303] J. M. Cline, *B decay anomalies and dark matter from vectorlike confinement*, *Phys. Rev.* **D97** (2018) 015013, [1710.02140].
- [304] I. de Medeiros Varzielas and O. Fischer, *Non-Abelian family symmetries as portals to dark matter*, *JHEP* **01** (2016) 160, [1512.00869].
- [305] J. Kawamura, S. Okawa and Y. Omura, *Interplay between the $b \rightarrow s\ell\ell$ anomalies and dark matter physics*, *Phys. Rev.* **D96** (2017) 075041, [1706.04344].
- [306] B. Bhattacharya, D. London, J. M. Cline, A. Datta and G. Dupuis, *Quark-flavored scalar dark matter*, *Phys. Rev.* **D92** (2015) 115012, [1509.04271].
- [307] J. M. Cline and J. M. Cornell, *$R(K^{(*)})$ from dark matter exchange*, *Phys. Lett.* **B782** (2018) 232–237, [1711.10770].
- [308] L. Di Luzio, M. Kirk and A. Lenz, *Updated B_s -mixing constraints on new physics models for $b \rightarrow s\ell^+\ell^-$ anomalies*, *Phys. Rev.* **D97** (2018) 095035, [1712.06572].
- [309] S. Descotes-Genon, L. Hofer, J. Matias and J. Virto, *Global analysis of $b \rightarrow s\ell\ell$ anomalies*, *JHEP* **06** (2016) 092, [1510.04239].

- [310] T. Hurth, F. Mahmoudi and S. Neshatpour, *On the anomalies in the latest LHCb data*, *Nucl. Phys.* **B909** (2016) 737–777, [1603.00865].
- [311] W. Altmannshofer, P. Stangl and D. M. Straub, *Interpreting Hints for Lepton Flavor Universality Violation*, *Phys. Rev.* **D96** (2017) 055008, [1704.05435].
- [312] G. D’Amico, M. Nardecchia, P. Panci, F. Sannino, A. Strumia, R. Torre et al., *Flavour anomalies after the R_{K^*} measurement*, *JHEP* **09** (2017) 010, [1704.05438].
- [313] G. Hiller and I. Nisandzic, *R_K and R_{K^*} beyond the standard model*, *Phys. Rev.* **D96** (2017) 035003, [1704.05444].
- [314] L.-S. Geng, B. Grinstein, S. Jäger, J. Martin Camalich, X.-L. Ren and R.-X. Shi, *Towards the discovery of new physics with lepton-universality ratios of $b \rightarrow s\ell\ell$ decays*, *Phys. Rev.* **D96** (2017) 093006, [1704.05446].
- [315] M. Ciuchini, A. M. Coutinho, M. Fedele, E. Franco, A. Paul, L. Silvestrini et al., *On Flavourful Easter eggs for New Physics hunger and Lepton Flavour Universality violation*, *Eur. Phys. J.* **C77** (2017) 688, [1704.05447].
- [316] A. K. Alok, B. Bhattacharya, A. Datta, D. Kumar, J. Kumar and D. London, *New Physics in $b \rightarrow s\mu^+\mu^-$ after the Measurement of R_{K^*}* , *Phys. Rev.* **D96** (2017) 095009, [1704.07397].
- [317] T. Hurth, F. Mahmoudi, D. Martinez Santos and S. Neshatpour, *Lepton nonuniversality in exclusive $b \rightarrow s\ell\ell$ decays*, *Phys. Rev.* **D96** (2017) 095034, [1705.06274].
- [318] C.-W. Chiang and H. Okada, *A simple model for explaining muon-related anomalies and dark matter*, 1711.07365.
- [319] B. Barman, D. Borah, L. Mukherjee and S. Nandi, *Correlating the anomalous results in $b \rightarrow s$ decays with inert Higgs doublet dark matter and muon $(g - 2)$* , 1808.06639.

- [320] B. Grinstein, S. Pokorski and G. G. Ross, *Lepton non-universality in B decays and fermion mass structure*, *JHEP* **12** (2018) 079, [1809.01766].
- [321] S. Chang, R. Edezhath, J. Hutchinson and M. Luty, *Leptophilic Effective WIMPs*, *Phys. Rev.* **D90** (2014) 015011, [1402.7358].
- [322] G. Steigman, B. Dasgupta and J. F. Beacom, *Precise Relic WIMP Abundance and its Impact on Searches for Dark Matter Annihilation*, *Phys. Rev.* **D86** (2012) 023506, [1204.3622].
- [323] AMS collaboration, M. Aguilar et al., *Electron and Positron Fluxes in Primary Cosmic Rays Measured with the Alpha Magnetic Spectrometer on the International Space Station*, *Phys. Rev. Lett.* **113** (2014) 121102.
- [324] AMS collaboration, L. Accardo et al., *High Statistics Measurement of the Positron Fraction in Primary Cosmic Rays of 0.5–500 GeV with the Alpha Magnetic Spectrometer on the International Space Station*, *Phys. Rev. Lett.* **113** (2014) 121101.
- [325] FERMI-LAT, DES collaboration, A. Albert et al., *Searching for Dark Matter Annihilation in Recently Discovered Milky Way Satellites with Fermi-LAT*, *Astrophys. J.* **834** (2017) 110, [1611.03184].
- [326] A. K. Alok, B. Bhattacharya, D. Kumar, J. Kumar, D. London and S. U. Sankar, *New physics in $b \rightarrow s\mu^+\mu^-$: Distinguishing models through CP-violating effects*, *Phys. Rev.* **D96** (2017) 015034, [1703.09247].
- [327] HFLAV collaboration, Y. Amhis et al., *Averages of b -hadron, c -hadron, and τ -lepton properties as of summer 2016*, *Eur. Phys. J.* **C77** (2017) 895, [1612.07233].
- [328] M. Artuso, G. Borissov and A. Lenz, *CP violation in the B_s^0 system*, *Rev. Mod. Phys.* **88** (2016) 045002, [1511.09466].

- [329] S. Aoki et al., *Review of lattice results concerning low-energy particle physics*, *Eur. Phys. J.* **C77** (2017) 112, [1607.00299].
- [330] CKMFITTER GROUP collaboration, J. Charles, A. Hocker, H. Lacker, S. Laplace, F. R. Le Diberder, J. Malcles et al., *CP violation and the CKM matrix: Assessing the impact of the asymmetric B factories*, *Eur. Phys. J.* **C41** (2005) 1–131, [hep-ph/0406184].
- [331] UTFIT collaboration, M. Bona, *Neutral charm mixing results from the Ufit collaboration*, *PoS CKM2016* (2017) 143.
- [332] A. Bazavov et al., *Short-distance matrix elements for D^0 -meson mixing for $N_f = 2 + 1$ lattice QCD*, *Phys. Rev.* **D97** (2018) 034513, [1706.04622].
- [333] A. Ibarra and S. Wild, *Dirac dark matter with a charged mediator: a comprehensive one-loop analysis of the direct detection phenomenology*, *JCAP* **1505** (2015) 047, [1503.03382].
- [334] J. Kopp, L. Michaels and J. Smirnov, *Loopy Constraints on Leptophilic Dark Matter and Internal Bremsstrahlung*, *JCAP* **1404** (2014) 022, [1401.6457].
- [335] J. Hisano, K. Ishiwata and N. Nagata, *Gluon contribution to the dark matter direct detection*, *Phys. Rev.* **D82** (2010) 115007, [1007.2601].
- [336] J. Hisano, R. Nagai and N. Nagata, *Effective Theories for Dark Matter Nucleon Scattering*, *JHEP* **05** (2015) 037, [1502.02244].
- [337] T. Jubb, *Dark Matter : No Place for WIMPs*, Ph.D. thesis, IPPP, Durham University, 2017.
- [338] B. J. Mount et al., *LUX-ZEPLIN (LZ) Technical Design Report*, 1703.09144.
- [339] R. K. Leane, T. R. Slatyer, J. F. Beacom and K. C. Y. Ng, *GeV-scale thermal WIMPs: Not even slightly ruled out*, *Phys. Rev.* **D98** (2018) 023016, [1805.10305].

- [340] H. An, L.-T. Wang and H. Zhang, *Dark matter with t-channel mediator: a simple step beyond contact interaction*, *Phys. Rev.* **D89** (2014) 115014, [1308.0592].
- [341] A. Alloul, N. D. Christensen, C. Degrande, C. Duhr and B. Fuks, *FeynRules 2.0 - A complete toolbox for tree-level phenomenology*, *Comput. Phys. Commun.* **185** (2014) 2250–2300, [1310.1921].
- [342] J. Alwall, R. Frederix, S. Frixione, V. Hirschi, F. Maltoni, O. Mattelaer et al., *The automated computation of tree-level and next-to-leading order differential cross sections, and their matching to parton shower simulations*, *JHEP* **07** (2014) 079, [1405.0301].
- [343] P. Artoisenet, R. Frederix, O. Mattelaer and R. Rietkerk, *Automatic spin-entangled decays of heavy resonances in Monte Carlo simulations*, *JHEP* **03** (2013) 015, [1212.3460].
- [344] T. Sjöstrand, S. Ask, J. R. Christiansen, R. Corke, N. Desai, P. Ilten et al., *An Introduction to PYTHIA 8.2*, *Comput. Phys. Commun.* **191** (2015) 159–177, [1410.3012].
- [345] D. Dercks, N. Desai, J. S. Kim, K. Rolbiecki, J. Tattersall and T. Weber, *CheckMATE 2: From the model to the limit*, *Comput. Phys. Commun.* **221** (2017) 383–418, [1611.09856].
- [346] ATLAS collaboration, M. Aaboud et al., *Search for dark matter produced in association with bottom or top quarks in $\sqrt{s} = 13$ TeV pp collisions with the ATLAS detector*, *Eur. Phys. J.* **C78** (2018) 18, [1710.11412].
- [347] ATLAS collaboration, *Search for electroweak production of supersymmetric particles in the two and three lepton final state at $\sqrt{s} = 13$ TeV with the ATLAS detector*, ATLAS-CONF-2017-039 (2017).

-
- [348] *Prospects for benchmark Supersymmetry searches at the high luminosity LHC with the ATLAS Detector*, Tech. Rep. ATL-PHYS-PUB-2013-011, CERN, Geneva, Sep, 2013.
- [349] *Search for Supersymmetry at the high luminosity LHC with the ATLAS experiment*, Tech. Rep. ATL-PHYS-PUB-2014-010, CERN, Geneva, Jul, 2014.
- [350] G. R. Farrar and P. Fayet, *Phenomenology of the production, decay, and detection of new hadronic states associated with supersymmetry*, *Physics Letters B* **76** (1978) 575 – 579.
- [351] ATLAS collaboration, G. Aad et al., *Search for long-lived stopped R -hadrons decaying out-of-time with pp collisions using the ATLAS detector*, *Phys. Rev. D* **88** (2013) 112003, [1310.6584].
- [352] CMS collaboration, *Search for stopped long-lived particles produced in pp collisions at $\sqrt{s} = 13$ TeV*, CMS-PAS-EXO-16-004 (2017).
- [353] G. Apollinari, O. Bruning, T. Nakamoto and L. Rossi, *High Luminosity Large Hadron Collider HL-LHC*, *CERN Yellow Report* (2015) 1–19, [1705.08830].